ABSTRACT

IMAGE ENHANCEMENT TECHNIQUES APPLIED TO SOLAR FEATURE DETECTION

by
Artur J. Kowalski

This dissertation presents the development of automatic image enhancement techniques for solar feature detection. The new method allows for detection and tracking of the evolution of filaments in solar images. Series of H-alpha full-disk images are taken in regular time intervals to observe the changes of the solar disk features. In each picture, the solar chromosphere filaments are identified for further evolution examination. The initial preprocessing step involves local thresholding to convert grayscale images into black-and-white pictures with chromosphere granularity enhanced. An alternative preprocessing method, based on image normalization and global thresholding is presented. The next step employs morphological closing operations with multi-directional linear structuring elements to extract elongated shapes in the image. After logical union of directional filtering results, the remaining noise is removed from the final outcome using morphological dilation and erosion with a circular structuring element. Experimental results show that the developed techniques can achieve excellent results in detecting large filaments and good detection rates for small filaments. The final chapter discusses proposed directions of the future research and applications to other areas of solar image processing, in particular to detection of solar flares, plages and sunspots.

IMAGE ENHANCEMENT TECHNIQUES APPLIED TO SOLAR FEATURE DETECTION

by
Artur J. Kowalski

A Dissertation
Submitted to the Faculty of
New Jersey Institute of Technology
in Partial Fulfillment of the Requirements for the Degree of
Doctor of Philosophy in Computer Science

Department of Computer Science

May 2003

APPROVAL PAGE

IMAGE ENHANCEMENT TECHNIQUES APPLIED TO SOLAR FEATURE DETECTION

Artur J. Kowalski

Dr. Frank Shih, Dissertation Advisor — Date
Associate Chairman and Professor of Computer Science, NJIT

Dr. James A.M. McHugh, Committee Member — Date
Acting Chairman and Professor of Computer Science, NJIT

Dr. Haimin Wang, Committee Member — Date
Associate Director of Big Bear Solar Observatory, Associate Director of Center for Solar Research and Professor of Physics, NJIT

Dr. Dimitri Theodoratos, Committee Member — Date
Associate Professor of Computer Science, NJIT

Dr. Chengjun Liu, Committee Member — Date
Assistant Professor of Computer Science, NJIT

BIOGRAPHICAL SKETCH

Author: Artur J. Kowalski

Degree: Doctor of Philosophy

Date: May 2003

Undergraduate and Graduate Education:

- Doctor of Philosophy in Computer Science
  New Jersey Institute of Technology, Newark, NJ, 2003

- Master of Science in Computer Science
  Warsaw University of Technology, Warsaw, Poland, 1990

Major: Computer Science

Presentations and Publications:

Frank Y. Shih and Artur J. Kowalski, "Computing unique three-dimensional object aspects representation," Information Sciences, Vol. 132, No. 1-4, pp. 13-22, February 2001

Frank Y. Shih and Artur J. Kowalski, "Automatic Extraction of Filaments in H-alpha Solar Images," submitted to Solar Physics, February 2003

To Kasia, my beloved and patient wife

ACKNOWLEDGMENTS

I would like to express my sincere appreciation to Dr. Frank Shih, who patiently served as my research supervisor, providing valuable and countless resources and insight. I would also like to thank Dr. Haimin Wang for introducing me to the magnificent world of solar research and for his detailed explanation of solar phenomena. Special thanks are given to Dr. James McHugh, Dr. Dimitri Theodoratos and Dr. Chengjun Liu for actively participating in my committee and providing valuable advice.

Special thanks are given to the Big Bear Solar Observatory for providing solar images and other important information used in this dissertation.

I would like to thank Dr. Fadi Deek for his mentor role during my teaching assistance years. I extend special thanks to my fellow graduate students for their assistance and support, in particular to Vijayalakshmi Gaddipati, Maria Cecilia Flores, Yugyung Lee and Jenlong Moh.

I also wish to thank my parents and my wife for their support and encouragement.

TABLE OF CONTENTS

TABLE OF CONTENTS
(Continued)

LIST OF TABLES

LIST OF FIGURES

LIST OF FIGURES
(Continued)

LIST OF FIGURES
(Continued)

LIST OF FIGURES
(Continued)

LIST OF FIGURES
(Continued)

CHAPTER 1

INTRODUCTION

1.1 Image Processing in Astronomy

Astronomical observations have a long history, dating back to ancient times. However the technological progress in recent years opened new areas of research and exploration of previously unknown astronomical phenomena and dependencies among them. The development of optical systems, introduction of CCD (Charge-Coupled Device) technology, dedicated computer and DSP (Digital Signal Processing) systems, mass storage, new means of communication and distributed research stimulated more precise, long-term investigations of astronomical facts and verification of new hypotheses.

Since most of the astronomical data come in the form of images (in different spectra: visible, UV and infrared light, wide range of radio waves), image processing techniques are natural means of data analysis. Some of these techniques, especially statistical and frequency-domain methods, have been used in astronomy for many years and led to revolutionary discoveries and observations. One of the areas relatively undeveloped in terms of image processing is solar image feature extraction.

The new hypotheses concerning solar filament disappearance associate it with coronal eruptions (and therefore with geomagnetic storms affecting power and communication systems). Timely prediction of such phenomena would allow for better protection against negative outcomes of the eruptions. This dissertation describes preliminary results of solar filament detection and proposes further developments of filament tracking system. It also suggests other application of the described methods, as well as new possibilities of solar feature extraction and enhancements.

1.2 Related Research

Image processing applied to astronomy employs a very wide range of image processing techniques. Some fields are quite well developed, especially in noise removal and image enhancements areas, but more specific topics still require development of new techniques or modifications of methods used in different, unrelated fields. Medical imaging is one of the distinct areas that influences strongly other image processing applications, thanks to the large variety of investigated problems and a huge demand for the solutions. Some of the methods of disease diagnosis may be used in astronomical feature extraction.

The techniques most frequently applied to astronomical image processing operate in frequency domain. The change of the processed data domain allows for better separation of the noise from useful information, for better image compression and for more efficient statistical image analysis in some cases.

1.2.1 General Astronomical and Solar Image Processing

Starck and Murtagh [63] review most common reversible transforms combined with multiscale image representation. Application of the wavelet transform (WT) and other multiresolution transforms (such as the multiresolution median transform) allow for efficient noise separation, especially for removing the most common Gaussian and Poisson noise (and combination of both). The paper also describes some new methods for source extraction in an image, based on the wavelet transform. The authors present the concept of multiscale image entropy and its application in measuring of relevant information, filtering, deconvolution and image compression.

Hill, Castelli et al. [33] describe a content-based retrieval application (SOLARSPIRE), which allows for searching large image sequence databases for solar phenomena (such as solar flares). The images are preprocessed to identify and record bright and dark spots based on their relative intensity with respect to their neighboring regions. Temporally persistent objects are extracted from the images and their spatio-temporal behavior is represented as intensity and size time series. The system allows users to query the database through a web-based interface and returns series segments that match the specified spatio-temporal behavior. The benchmark results based on 2500 satellite images show better than 85% matching accuracy on solar phenomena previously identified by astrophysicists.

Irbah, Bouzaria et al. [35] discuss a problem of the noise and spots removal from temporal series of solar images, used in the solar astrolabe experiment. The authors propose a new image-processing method which removes the noise and spots, allowing for accurate solar edge detection needed in their astrolabe experiment. Their method is based upon the use of wavelet transform in the solar image analysis. Their implementation removes image defects (parasite spots) and noise without reducing image resolution and then extracts solar edges of these images and reconstructs trajectories.

Krejčí, Flusser and Šimberová [36] introduce a new method of multichannel blind deconvolution applied to blur removal from solar images. They propose a simple, computationally efficient algorithm that does not need any statistical presumptions about the image. The results of method application to removal of the atmospheric turbulence blur in the astronomical images are promising, particularly when applied to the images of sunspots.

Miura, Baba et al. [46] propose a new method for the improvement of resolution in observed solar images. The authors use a blind deconvolution method for restoration of an atmospherically-degraded solar image, which can restore fine structures that are blurred in an observed image. They also apply a super-resolution method to its restored image to improve the resolution (by making the cutoff frequency in a blind-deconvolved image higher). The technique presented in the paper produces results with fine structures visibly restored.

Paumard and Aubourg [52] present a fast method for finding a translation between a pair of astronomical images. The technique presented in the paper relies on comparison of the brightest stars in the images using a censored Hausdorff distance and can be used to obtain a first estimate with a precision of a few pixels. The results may be used to initiate a second method to achieve the desired sub-pixel accuracy. The paper describes also a method implementation on a massively parallel computer, showing that real-time processing is feasible, with good prospects for the development of specialized efficient hardware systems.

The work of Zhou, Kambhamettu et al. [81] describes a different environment, but their method may be applied to tracking changes in the solar chromosphere. The authors discuss problems of tracking structure and motion of nonrigid objects (such as clouds) from monocular images. They present a hierarchical method, which integrates local analysis (recovering small details) and global analysis (appropriately limiting possible non-rigid behaviors) to recover depth values and nonrigid motion from sequences of two-dimensional satellite cloud images. Their article describes a recursive

algorithm that integrates local analysis with appropriate global fluid model constraints and presents a new structure and motion analysis system (SMAS), which was developed using the described algorithm. Their method may be used for tracking smooth motion in other fluidal environments.

1.2.2 Filament Detection

One of the specific areas of solar image processing is filament detection. There is a very small number of publications concerning this particular topic. One of the filament detection approaches used in TRACS project - Toolkit for Recognition and Automatic Classification of Solar Features [1] employs local edge detection with linking edge vectors of similar angles.

More complete method is presented by Gao, Wang, and Zhou [26]. Their method uses binary thresholding with the half of the image median value as a threshold, followed by region growing. Pieces of filament segments are merged within 80-pixel neighborhood, and all segments within 40-pixel distance are merged into a single filament. Filaments with the total area smaller than a preset area threshold are ignored. This method was applied to the Big Bear Solar Observatory's (BBSO) full-disk H-alpha images.

1.2.3 Image Segmentation and Classification

Candeas, Braga Neto et al. [11] explore the star/galaxy discrimination problem. They propose an original approach to the characterization of these astronomical objects, which is based on gray-level shape information, using mathematical morphology. They present a system that executes image pre-processing, segmentation and feature extraction,

employing mathematical morphology tools implemented using the MMach toolbox for the Khoros system. The segmentation results based on the watershed method are compared with the results obtained by using a classical software package SExtractor. The shape information is extracted through the use of the gray-level morphological pattern spectrum, which yields very satisfactory shape features. The resulting objects are suitable for consecutive work in neural-network automatic classification.

Leung and Jordan [39] discuss problems of image segmentation of weather satellite imagery that is an important initial step in an automated weather forecasting system. Accurate cloud extraction methods are also needed in the determination of the solar radiative transfer in atmospheric research, where satellite observations are used as inputs to global climate models to predict climatic change. The authors propose a new, simple and fast algorithm for cloud extraction, based on an Adaptive Average Brightness Threshold (AABT) algorithm. The algorithm implementation is faster than most of other extraction algorithms, giving sufficiently accurate results.

Lybanon, Lea and Himes [41] present a flexible approach to image segmentation, originally developed for optical astronomical images, that is also applicable to other problem domains such as analyzing infrared oceanographic images and solar magnetograms. The proposed technique is based on the morphological operations of opening and closing. The original implementation was designed to find star boundaries in optical astronomical images and relied on their property: the image background is dark and stars, the brightest objects, are uniform or increase in intensity toward their centers. An additional pre-processing step (based on selected morphological operations) was needed for removing regions with extreme brightness values, for finding fronts and

associated rings in infrared ocean images and for identifying sunspots and other magnetically active regions in magnetograms. The edges found in the images processed using the algorithm are useful as inputs in other image processing systems, e.g. in automated tracking of ocean features.

Turmon and Mukhtar [69] discuss problems related to segmenting images of the solar chromosphere into three classes (plagues, networks and background), which contribute differentially to the ultraviolet radiation reaching the Earth. The authors describe means of segmenting solar images into the constituent classes and a novel high-level representation for compact objects based on a triangulated spatial membership function. These representations are fitted in a variable-dimension Markov chain Monte Carlo scheme, providing an efficient separation of the image features.

1.2.4 Elongated Shapes Extraction

Gregson [32] presents an algorithm for detecting neural processes in serial optical sections for use in an automated three-dimensional neural reconstruction system. The algorithm addresses the problems specific to neural element detection, in images with minimal resolution, operators with small spatial supports, highly curved, filamentous features, large variations in intensity profile, poor signal-to-noise ratio, and determination of depth without stereo. The first step in the method is finding the magnitude and orientation of the maximum intensity second directional derivative. Then, a family of curves is locally fitted to the data, and the projections of the data on the curve family are found. If a pixel lies on a curve with sufficient total projection, it is labeled with the magnitude, orientation, curvature, spatial extent, and element displacement. Depth is

interpolated from the spatial extent data for neighborhoods in three adjacent (in depth) images by using an approximation to the depth-dependent optical point spread function.

Orriols, Toledo et al. [49] address the object recognition problem in a probabilistic framework to detect and describe object appearance through image features organized by means of active contour models. The authors consider the formulation of saliency in terms of visual similarity embedded in the probabilistic principal component analysis framework. A likelihood of object structure detection is obtained using the relation between the visual field and the internal object representation. Deformable models are employed introducing a computational methodology for a perceptual organization of image features as an abstract understanding of the integration between structure and constraints of the visual information-processing problem. The method applied to the vessels segmentation in angiography produces very promising results. The same authors investigate the problem further using different methods.

Toledo, Orriols et al. [67] present a statistic snake that learns and tracks image features by means of statistic learning techniques. Using the probabilistic principal component analysis, a feature description is obtained from a training set of object profiles. The paper introduces a sound statistical model to define a likelihood estimate of the gray-level local image profiles together with their local orientation. This likelihood estimate allows for defining a probabilistic potential field of the snake, where the elastic curve deforms to maximize the overall probability of detecting learned image features. To improve the convergence of snake deformation, the likelihood map is enhanced by a physics-based model simulating a dipole-dipole interaction. A new extended local coherent interaction is introduced, defined in terms of extended structure tensor of the

image to give priority to parallel coherence vectors. The method applied to the tracking of coronary vessels - elongated structures observed in angiographies - produces very encouraging results. This technique is further developed and described in [68]. The second paper introduces a new deformable model, called eigensnake, for segmentation of elongated structures in a probabilistic framework. Instead of snake attraction by specific image features extracted independently of the snake, the eigensnake learns an optimal object description and searches for such image feature in the target image. This is achieved by applying principal component analysis to image responses of a set of Gaussian derivative filters. Therefore, attraction by eigensnakes is defined in terms of classification of image features. The potential energy for the snake is defined in terms of likelihood in the feature space and incorporated into a new energy-minimizing scheme. Hence, the snake deforms to minimize the mahalanobis distance in the feature space.

Zana and Klein [78], [79], [80] present algorithms based on mathematical morphology and linear processing for vessels recognition in a noisy retinal angiography. The authors define a geometrical model of undesirable patterns in order to separate the vessels from their environment [78]. The technique extracts first bright round peaks, allowing for segmentation of microaneurisms from suitable angiograms of diabetic patients. Next, linear structures are extracted using mathematical morphology, and then appropriate differential properties are computed using a Laplacian filter. Finally, the vessels are extracted using curvature differentiation. Results on various medical data from a normal eye and from a set of different abnormalities are presented, showing that the method can be used as a robust segmentation tool. An enhancement of this technique is presented in [80]. In order to differentiate vessels from analogous background patterns,

a cross-curvature evaluation is performed. The vessels are separated out as they have a specific Gaussian-like profile whose curvature varies smoothly along the vessel. The detection algorithm that derives directly from this modeling is based on four steps: (1) noise reduction; (2) linear pattern with Gaussian-like profile improvement; (3) cross-curvature evaluation; (4) linear filtering. Another development of the technique, described in [79] uses temporal and multimodal registration of retinal images based on point correspondence. After detecting the vascular tree, the bifurcation points are labeled with surrounding vessel orientations. An angle-based invariant is then computed in order to give a probability for two points to match. Then a Bayesian Hough transform is used to sort the transformations with their respective likelihoods. A precise affine estimate is finally computed for most likely transformations. The best transformation is chosen for registration.

Soille and Talbot [58] prove that a translation invariant implementation of min/max filters along a line segment of slope in the form of an irreducible fraction dx/dy can be achieved at cost of 2 + k min/max comparisons per image pixel, where k = max(|dx|, |dy|). In their method, for a given slope, the computation time is constant and independent of the length of the line segment. One of the applications described in the paper concerns min/max filters along gray tone periodic line segments, allowing for efficient extraction of elongated object from an image.

1.2.5 Three-Dimensional Image Reconstruction

Imamura, Kitaoka et al. [34] describe a problem of producing three-dimensional solar corona information from a set of X-ray solar images. Even with images taken by the observation satellite 'Yohkoh' from different view angles, the created stereo images lose

the stereoscopic effect due to the changing textures on the sun's surface. The authors propose an efficient method for correcting texture deformations which includes varying surface using morphological processing and rotation by affine transformations. Application of the method significantly improves the correspondence between stereo image pairs.

Mascarenhas, Souza et al. [45] describe a new approach to image 3D interpolation using Bayesian estimation theory. They present two methods that depend on the information used a priori. The approach is applied to the interpolation of X-ray images from the solar atmosphere taken at different depths, as well as RMN tomographic images of a tomato, producing a sharp visualization of the objects.

1.2.6 Problems Related to Observation Methods

Chae, Yun et al. [12] discuss problem of the stray-light correction in filter-based magnetograph observations. They present an iterative algorithm for the maximum entropy method, which seeks the solution in Fourier space and thus accomplishes fast convergence. Their method uses the maximum entropy principle for the image deconvolution to guarantee that intensity should be positive and polarization degrees should be less than unity. The method presented in the paper is effective in correcting stray light, which has a spread angle greater than the full width at half maximum of the point spread function. They also discuss the effect of stray light on magnetograph calibration.

Thorpe and Fraser [65] discuss the problem of wavefront distortion introduced as light passes through the atmosphere, resulting in images exhibiting, among other effects, blurring which varies from region to region. The authors describe the effect of

atmospheric turbulence on short exposure images and propose a technique that removes the position dependency of the blurring. The individual images are dewarped, summed and then iteratively deblurred using an estimate of the now position independent point spread function, introduced by the telescope optics and the atmosphere. The resultant image approaches the theoretical resolution limit of the optical/imaging system used in observations. An important by-product of the research - a sequence of detailed shift maps providing a visualization of the instantaneous turbulence field - is also described in the paper.

The further development of the technique, based on a point-by-point registration to subpixular accuracy of multiple telescopic images of scenes distorted by the atmosphere, both astronomical and terrestrial, is presented by Thorpe, Lambert and Fraser [66]. The registration phase of the newer method is based on hierarchical, windowed area-correlation. Each resulting x and y shift-map is used to dewarp the corresponding raw image in the sequence. Registration is made to a prototype average image, which is initially a motion-blurred average of the uncorrected image sequence, but which is later refined to be the average of the dewarped sequence. The process is executed iteratively, using the current best average result as a new prototype. The resulting x and y shift-map sequence can be viewed as a movie, providing a striking visualization of the wavefront distortion due to atmospheric turbulence.

1.2.7 Parallel Processing Methods

Goller and Leberl [29] describe a system that implements shape-from-shading, stereo matching, resampling, gridding and visualization of terrain models in such a manner that they execute either on parallel machines or on clusters of workstations. Since some radar

image processing algorithms such as shape-from-shading are particularly time consuming and data sets to be processed are large, the authors' method allows for faster processing in a distributed manner. The speedup for image processing tasks in their approach increases nearly linearly with the number of processors, both on parallel machines and on clusters of distributed workstations. Their method would allow users of complex image processing algorithms to easily port the implemented code and to eliminate the necessity for specialized parallel processing hardware is eliminated.

De Vos, van der Schaaf and Bregman [71] describe development of the LOFAR (LOw-Frequency ARray) telescope as a giant data processing machine, consisting of 13,000 antennas that produce a data stream of 2 Gbit/s each. The data are processed by a massive cluster computer and converted to astronomical images and other data products using distributed applications. The LOFAR data processor is being designed as a heterogeneous system containing digital signal processors, programmable logic and general-purpose microcomputers with a total processing power of 40 TFLOPS. To allow for iterative calibration, over 600 TBytes of online storage is envisaged. LOFAR is being developed in a collaboration between the Netherlands (ASTRON) and the USA (NRL and MIT Haystack Observatory). The initial simulations effectively handle the data distribution needed for the correlation process in the interferometric imaging and show very promising capabilities of the system that should reach the full-capacity science operations in 2007.

1.3 Organization of the Dissertation

The second chapter of this dissertation provides astronomical observatory background information, defines research problems and describes in detail areas of solar image processing that require development of new techniques. The third chapter describes current technology developed for filament detection and presents the results for regular and noisy solar image processing. The fourth chapter proposes directions of further works in this field, as well as applications of the developed methods in other areas. Appendix A presents figures of solar image processing results. Appendix B demonstrates the IP_Tools image processing software, used to obtain the results described in this dissertation. Appendix C includes a glossary of solar terms, provided by the Space Environment Center. The last chapter presents the list of relevant references.

CHAPTER 2

SOLAR IMAGE PROCESSING CHALLENGES

2.1 Big Bear Solar Observatory

The Department of Physics of the New Jersey Institute of Technology manages the Big Bear Solar Observatory (BBSO) in California. The observatory is located in the middle of the Big Bear Lake to reduce the image distortion which usually occurs when the Sun heats the ground and produces convection in the air just above the ground. Turbulent motions in the air near the observatory are also reduced by the smooth flow of the wind across the lake instead of the turbulent flow that occurs over mountain peaks and forests. BBSO, located at 2,000 meters (6,750 feet) elevation, uses 25 cm and 65 cm telescopes to observe sunspots and active regions as well as filaments, network and tiny intra-network elements. With 300 sunny days a year and continuous solar observation from sunrise to sunset, the Big Bear Solar Observatory provides invaluable amount of research data.

2.2 Solar Observation Data from BBSO

The Big Bear Solar Observatory acquires solar disk data from multiple sources. Installation of new CCD cameras allow for obtaining full-disk data in H-alpha, white-light spectrum, as well as magnetograms with resolution of 1 Arcsec. The continuous H-alpha (Hydrogen-alpha, 656.3 nm) full-disk observations produces 600-700 solar images per day. The Apogee KX4 CCD Camera, used for image recording, supplies images with the spatial resolution of 2032×2032 pixels and 14-bit dynamic range. The resulting images are stored as 16-bit grayscale pictures, archived in FITS format [76].

2.3 Areas of Solar Research

Solar studies cover a vast area of topics, spanning multiple branches of physical sciences. The scope of this work, related to some areas of the Big Bear Solar Observatory research, is limited to the image processing aspects of a few solar chromospheric phenomena. At this time, the following topics are investigated with regard to the image processing support:

2.3.1 Filaments

Filament detection and tracking is currently one of the most important aspect of the Big Bear Solar Observatory research that requires advanced image processing assistance.

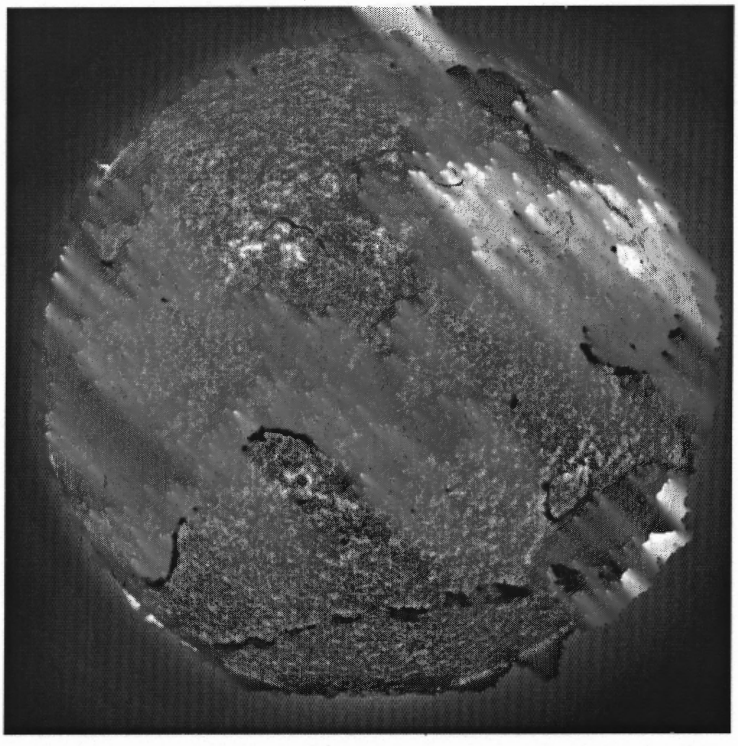

Figure 2.1 Chromosphere with multiple filaments (from BBSO [5]).

A filament is a mass of gas suspended over the photosphere by magnetic fields. Since filaments have much lower temperature, but much greater density than the solar corona, they are visible in H-alpha spectrum as dark elongated shapes against the bright disk (see Figure 2.1). If a filament is seen at the edge of the disk, against the dark space, it is perceived as bright ribbons connected to the disk; in this case it is called a prominence (see Figure 2.2). Filaments are formed on the division of magnetic regions with opposite polarities. They may last for multiple days, changing their manifestation, but eventually they vanish. Filaments disappearance may end up with a large Coronal Mass Ejection (CME) and is associated with geomagnetic storms that may affect the quality of terrestrial communication, power system and safety of space missions. Therefore, automatic detection of filament disappearance becomes an important task with a practical application.

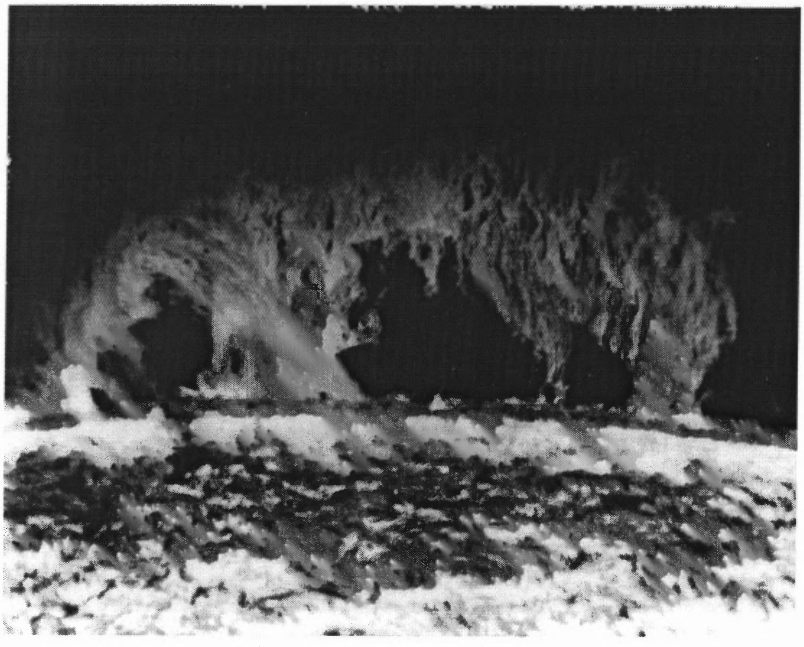

Figure 2.2 An example of solar prominences (from BBSO [5]).

In the solar images, the filaments appear as dark elongated objects of different shape and size. Sometimes they may be broken into separate parts, as visible at the bottom of Figure 2.1. It may be assumed that the filaments of some importance have the area of more than 200 $Arcsec^2$ (as observed on H-alpha full-disk picture). Since the spatial CCD resolution used in the Big Bear Solar Observatory is 1 Arcsec, the threshold area for filament detection may be set to 200 pixels in the original images of 2032×2032 pixels. To shorten the processing time, the images are scaled down to 1016×1016 pixels; therefore, the filament detection threshold is set to 50 pixels.

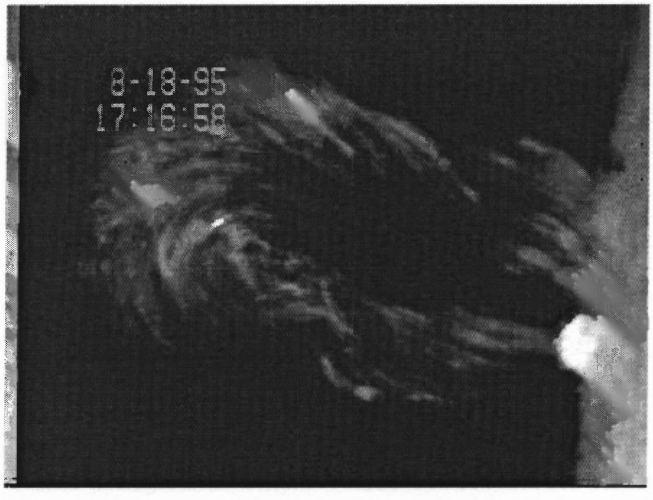

Figure 2.3 An example of Coronal Mass Ejection (from BBSO [5]).

There are additional aspects of filament detection that need to be considered:

1. A filament may appear as a series of disconnected parts, each of which may be smaller that the assumed threshold. A filament detection system should connect those parts while trying to extract the filament.
2. Sunspots should be distinguished from filaments based on the shape (round versus elongated) and filtered out, since they are not related directly to the CME or geomagnetic storms.

3. The brightness of a filament and of the surrounding area of the solar disk diminishes from the disk center toward the edge. Therefore, the relative brightness of filaments should be used in filament detection.
4. The size of any feature on the solar disk appears reduced toward the disk edge. Consequently, the filament threshold size should be scaled, or the whole solar disk image should be transformed before the detection.

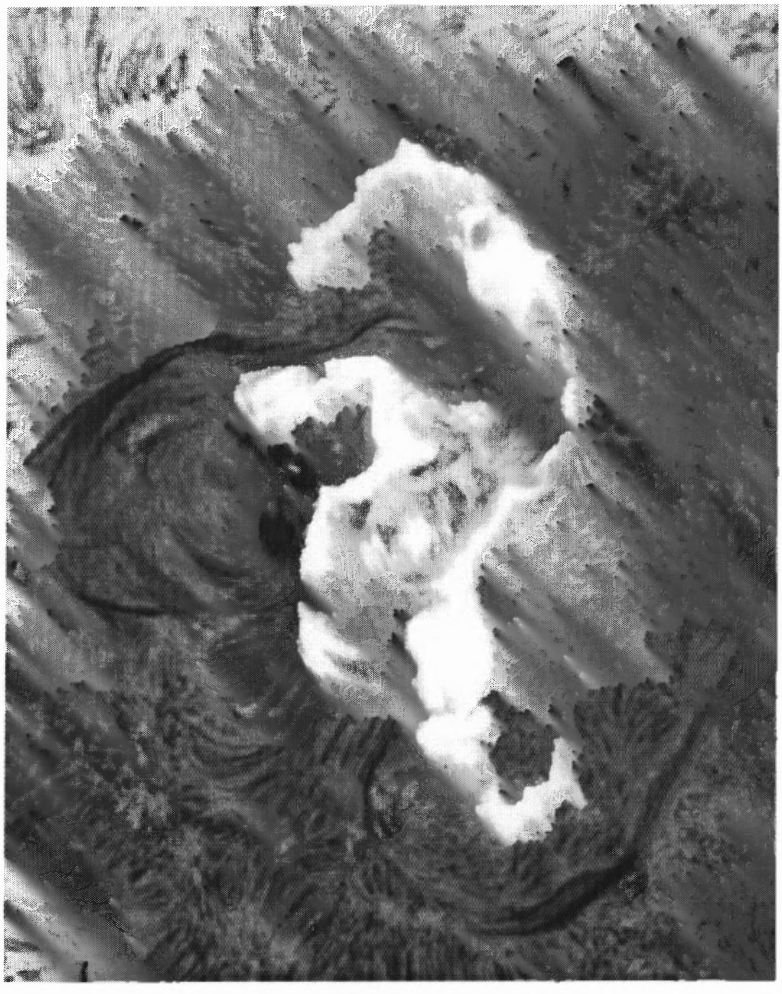

Figure 2.4 Enlargement of the solar disk fragment with a flare (from BBSO [5]).

2.3.2 Flares and Coronal Mass Ejections

As mentioned in the previous section, filament disappearances are usually connected with occurrences of increased solar activity, such as flares and Coronal Mass Ejections (CME). Electromagnetic disruptions in terrestrial communication resulting from such activity stimulate exploration of these phenomena. Although the practical aspect of solar activity motivates researchers to focus on successful prediction of such events, observation of development of solar flares and CMEs is also considered an important research area.

Solar flares may be described as very bright, large features visible against the solar disk. They develop in a matter of minutes and may last for several hours. An automatic flare detection may be based on very high luminosity level (close to the upper range of the CCD output) and on considerable size (at least a few hundred $Arcsec^2$). The appearance of a flare may also significantly increase the average brightness of the image, easily detectable in a series of consecutive images.

The Coronal Mass Ejection may or may not be caused by solar flares. The CMEs send huge quantities of hot solar plasma into the space. They are similar in appearance to the flares when observed against the solar disk. When visible at the limb, against the dark space, they are easily recognizable as large light loops of the same magnitude as the solar disk diameter.

2.3.3 Other Solar Phenomena

Advances in solar research depends on collecting and processing of solar images. Multiple research topics are based on the recognition and extraction of solar features. The following feature detection may benefit from image processing technology:

- *Solar granulation*

  The surface of the photosphere is not uniform – it consists of approximately 5,000,000 granules. The average diameter of a granule is about 1.5 Arcsec, slightly above the resolution of the BBSO CCD array. The granules carry energy from the inner layers of the Sun toward the photosphere. The solar granulation continuously changes, since a granule lifespan is about 15 minutes. Granulation changes reflect dynamic processes inside the Sun, so they are carefully examined. Observations of the granularity require processing series of photospheric images taken in short time intervals and finding the correlations and differences between consecutive images. The images may be enhanced to increase the contrast in order to facilitate granule separation.

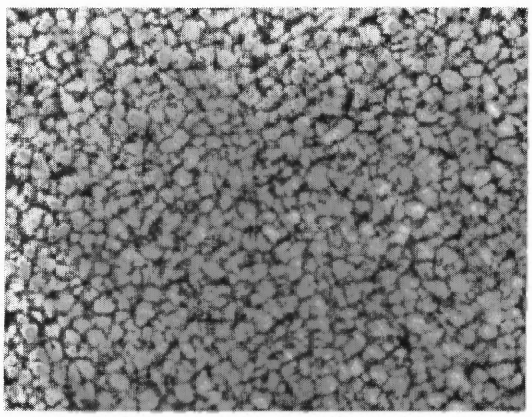

Figure 2.5 An example of photospheric granulation (from BBSO [5]).

- *Filigrees*

  The space between granules is usually darker (colder), but sometimes some bright features, called filigrees, appear in the gaps. They are slightly hotter than the granules, so they are visible as tiny bright speckles. The filigree extraction is difficult, since they are approximately ¼ Arcsec across, often below the resolution of terrestrial telescopes.

- *X-ray bursts*

  The Sun emits energy in many different ranges of the spectrum. The energy bursts observable in the X-ray wavelengths produce interesting effects. To facilitate research, the images captured with X-ray telescopes have to be converted into visible spectrum and further processed as regular images.

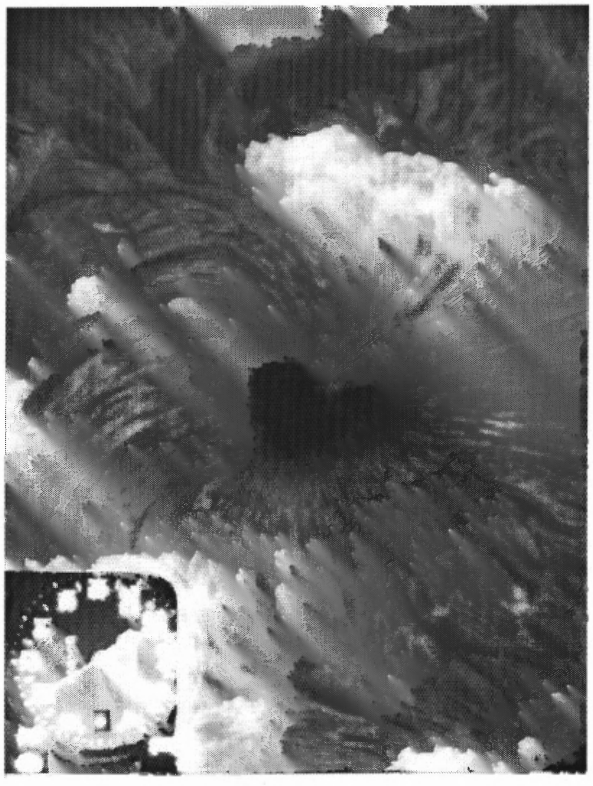

Figure 2.6 An example of a sunspot (from BBSO [5]).

- *Sunspots*

  One of the most important solar activity is the appearance and evolution of sunspots. Sunspot observations are one of the oldest branches of solar research, dating back to the 17th century. Conventional sunspot observations focused on the spot size, shape, spatial and temporal distribution (such as E. Walter Manduer's butterfly diagram). New sunspot studies concentrate on the spot structure, relation to inner solar processes and extraction of features in sunspot penumbra (outside the dark sunspot center, umbra).

- *Plages and faculae*

  These solar phenomena can be observed as slightly brighter areas on the solar surface. The plages are well visible in the H-alpha spectroheliogram images. In this spectrum sunspots are not easily observable, but the bright plages that usually surround sunspots help to identify the spots. The faculae are best seen in the outer parts of the disk, where they appear as bright patches against limb-darkened regions on the edge of the solar disk. They can be observed anywhere on the solar surface, but they are harder to distinguish in the center of the solar disk.

CHAPTER 3

FILAMENT DETECTION - TECHNOLOGY DEVELOPMENT

The effort of solar image processing described in this document was focused on filament detection. The chromospheric filaments usually mark a boundary between two opposite magnetic regions. Disappearance of such filaments usually causes a coronal mass ejection and a magnetic storm. The latter phenomenon disrupts Earth communication; therefore filament tracking is an important task of solar observations.

The most difficult part of filament tracking is separation of a filament from solar image background. Filaments are similar to other dark features in solar images, but may be defined as prominent, elongated, thin, dark objects on the surface of the Sun.

From among the multiple possible methods of features extraction, the initial work in this dissertation focuses on the techniques based on mathematical morphology. These techniques offer precise and fast discrimination of the required features and can be used in parallel processing or DSP (Digital Signal Processing) systems [60].

The proposed method consists of two steps – image preprocessing and feature extraction. In the first step, the superfluous features are removed from the image as it is converted from grayscale to black and white (binary). The outcome is then used for filament detection using multiple morphological operations. The final result is a black and white image with the black features being the solar filaments detected in the process.

3.1 Image Preprocessing

In the initial step of filament detection, all additional features of the solar chromosphere (flares, plages, faculae, other differences in coronal brightness) should be eliminated, leaving only the solar disk with light and dark spots cleanly separated. In the resulting image, filaments should be visible as black elongated shapes, with as few other black features (mostly solar surface granularity and sunspots) as possible.

A few preprocessing techniques were evaluated, yielding different results.

3.1.1 Histogram Equalization

The histogram equalization technique is considered as the first preprocessing stage since it usually enhances the image visually and might be suitable for some feature detection techniques. In general, histogram equalization reassigns the brightness values of pixels (either in grayscale or in the separate color channels) based on the image histogram. Individual pixels retain their brightness order, but the values are shifted, so an equal number of pixels appear in each possible brightness value. Usually, this technique spreads out the values in areas where different regions meet, showing detail in such areas with a high brightness gradient [57]. The histogram equalization in the discreet brightness space is given by the relation (as described in [30]):

$$s_k = \sum_{j=0}^{k} \frac{n_j}{n} \qquad \mathrm{k} = 0, 1, \ldots, \mathrm{L}-1 \tag{3.1}$$

where s_k is the new brightness level for the original brightness level k, L is the number of brightness levels, n_j is the number of original pixels with the brightness level of j, and n is the total number of pixels in the image.

Two histogram equalization versions were used:

3.1.1.1 Global Histogram Equalization. The global histogram equalization changes histogram of the whole image in a uniform way. Applying it improves visually the solar image (see Figures A.3 and A.4), enhancing the image contrast and in most cases widening the distance between the dark features and the bright background, but the changes are not really suitable for further processing because there is no change in relative differences of the brightness level of all image features. The global histogram equalization also fails to "normalize" the brightness of the detected features throughout all regions of the solar disk (in some cases the background at the disk edge can be darker than the filament visible in the disk center).

3.1.1.2 Local Histogram Equalization. The deficiencies of the global histogram equalization can be avoided by using local histogram equalization. In this method the equalization is applied to windows of selected size (e.g., 50 × 50 pixels), moving throughout the image. Since parts of the image are enhanced locally, the distance between dark features and the bright background changes in different way in different parts of the image. The resulting image will have more uniform gray levels of the filaments and more uniform background levels.

Unfortunately, since the image is processed in totally separate windows (the window moves by its edge size), the border pixels of one window may be significantly brighter or darker than the edges of the adjacent windows (even if they have the same brightness values before the equalization), as shown in Figures A.5 and A.6. During feature extraction, such differences between edges may incorrectly be recognized as filaments.

An improvement of local histogram equalization can be achieved by using a smooth (pixel by pixel) movement of the work window. In this method the artificial features created on the boundaries of the work widows disappear because only the central pixel is being processed, according to the brightness levels of its surrounding pixels in the same work window. Since the equalized histogram does not change drastically when the window is moved by one pixel, the resulting levels will not change abruptly. The equalized image is more suitable for further filament detection (see Figures A.7 and A.8) but the processing time becomes unacceptable because the computational complexity is increased proportionally to the number of pixels in the work window.

3.1.2 Thresholding

Thresholding is one of the most important image segmentation techniques and is often used as a preprocessing step for feature extraction. Thresholding with a single threshold level (more frequently used than multilevel thresholding) can be described (see [30]) as an operation that involves test against a function *T* of the form

$$T = T[x, y, p(x, y), f(x, y)] \tag{3.2}$$

where *f(x, y)* is the brightness level of image pixel *(x, y)* and *p(x, y)* denotes some local property of this pixel (such as an average brightness level of a neighborhood centered on this pixel).

The thresholded image *g(x, y)* is defined as

$$g(x, y) = \begin{cases} L-1 & \text{if } f(x, y) > T \\ 0 & \text{if } f(x, y) \leq T \end{cases} \tag{3.3}$$

where *L-1* is the maximum brightness level of the resulting image.

3.1.2.1 Global Thresholding. The most intuitive method that could be used to separate dark filaments from the bright disk background is single-level thresholding applied to the whole image. Since the thresholded image *g(x, y)* depends only on the pixel brightness level *f(x, y)* and the function *T* remains constant for every pixel in the image, this technique is called global thresholding.

The experimental results shown in Figures A.9-A14 demonstrate that based on the threshold value filaments can be separated from the background, but only in some parts of the image. The cause of the problem is a solar phenomenon called the limb darkening. The brightness level of the disk background as well as of the solar features decreases toward the edge of the solar disk. Although the relation between the dark and bright solar features is preserved, the absolute values of the same features are different in different parts of the solar disks. Therefore, global thresholding may correctly separate filaments in the disk center, but merges them in the background at the disk edge (see Figure A.13) or discriminates the filaments correctly close to the disk edge, but loses all the details in the center (see Figure A.9).

3.1.2.2 Local Thresholding. To diminish the influence of limb darkening on the preprocessing results, another thresholding technique is considered. In local thresholding, the function *T* depends on both *f(x, y)* and *p(x, y)*, so this technique may change the threshold level based on the local differences between the background and feature values. To avoid creation of incorrect artificial filaments, the work window may be moved smoothly (pixel by pixel) throughout the whole image. In the experiments, a median filter is used as local property function *p(x, y)*, so the function *T* could be described as

$$T = \mathrm{med}_z(x, y) \tag{3.4}$$

where $med_z(x, y)$ is a median value of a $z \times z$ neighborhood centered on *(x, y)*.

In the first step, the median value for the work window neighborhood of every pixel in the image is computed and stored. In the next step the thresholding is applied to every pixel, with the threshold value being the appropriate retrieved median value for that pixel. Two variations of the method are considered.

In a simpler variant the thresholding is based purely on the local median value. The results are promising, but in the very bright and very light areas some unimportant features are enhanced (this problem is particularly visible in the dark space outside the solar disk) – see Figure A.15.

3.1.2.3 Further Improvements of Thresholding Method. In a modified method an additional preprocessing step is applied – very bright and very dark regions are directly transformed to white and black areas, respectively. The initial median calculation step remains unchanged, but before the final thresholding, the pixel brightness value is compared to the low and high cutoff values. If the pixel brightness is lower than or equal to the lower cutoff margin value, then the output pixel brightness is assigned black value; if the pixel brightness is higher than or equal to the higher cutoff margin value, the output pixel is set to white value; otherwise the thresholding based on the local median value is applied. In this case, the threshold function T can be described as

$$T = \begin{cases} c_{inf} & \text{if } med_z(x, y) \le c_{inf} \\ med_z(x, y) & \text{if } c_{inf} < med_z(x, y) < c_{sup} \\ c_{sup} & \text{if } med_z(x, y) \ge c_{sup} \end{cases} \tag{3.5}$$

where c_{inf} and c_{sup} are lower and higher cutoff margin values, respectively.

A few experiments with different cutoff margin values demonstrate that this method is suitable for separating dark solar features and does not create artificial features in very dark or bright regions (see Figures A.17-A.22). In some cases, artificial features appear in plage regions or in bright surroundings of sunspots because the local median method amplifies tiny brightness differences in regions with similar brightness. This problem can be eliminated with asymmetrical cutoff values (using larger margin for bright values – see Figures A.23 and A.24).

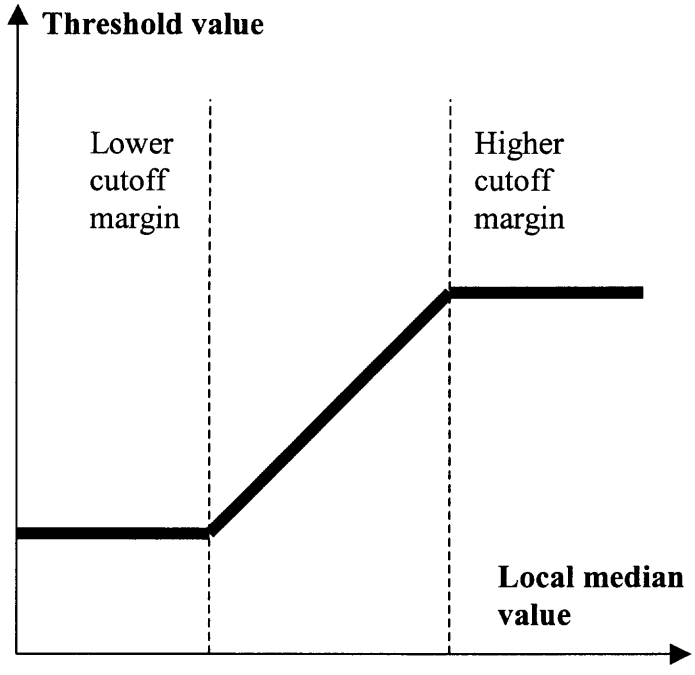

Figure 3.1 Threshold value for local thresholding with cutoff margins.

Since filaments are usually significantly colder than gaps in solar chromosphere granularity, and therefore darker, an additional modification can be introduced for better separation of filaments from the surrounding background. If the thresholding value (the

local median) is multiplied by a constant factor lower than 1, dark filaments are separated more precisely from slightly brighter granularity gaps. The threshold function T in this case can be described as

$$T = \begin{cases} c_{inf} & \text{if } med_z(x, y) \cdot m \leq c_{inf} \\ med_z(x, y) \cdot m & \text{if } c_{inf} < med_z(x, y) \cdot m < c_{sup} \\ c_{sup} & \text{if } med_z(x, y) \cdot m \geq c_{sup} \end{cases} \quad (3.6)$$

where m is a local median modification factor, $0<m<1$.

After some experiments with different cutoff margin values, window sizes and the modification factors, it can be determined that the modified local thresholding technique using Equation 3.6 is the most suitable one for further filament detection (see Figures A.25 and A.26).

3.1.3 Global Thresholding with Brightness and Area Normalization

Since local thresholding is a time-consuming technique, an alternative set of preprocessing methods was investigated. The solar disk image is normalized in such a way that the average brightness level is the same for every image and the limb darkening is removed. These operations allow for a simple sunspot removal and separation of filaments through global thresholding using the same parameters for all preprocessed images. Additionally, equal area projection is investigated to simplify filament detection based on the area threshold.

3.1.3.1 Solar Disk Center and Radius Detection. Since the position and size of the solar disk in each image may vary, the next preprocessing step identifies the location of the disk center and the radius value. This is done by seeking the disk edges starting

from the image center toward the limb. The disk edge is identified by a low brightness threshold value of 50. The disk center is then calculated as the center of gravity of the edge pixels, and the radius as the average distance of the edge from the center.

3.1.3.2 Brightness Level Normalization. Solar images are not always taken under identical conditions, so the overall disk brightness may differ. An additional normalization step converts image brightness levels to a uniform space. The brightness of the image is scaled to achieve the luminosity value of 200 in the central disk region by calculating the average brightness of the central circular area within 100-pixel radius in the original image and scaling it to the average brightness of an "ideal" normalized image.

3.1.3.3 Disk Brightness Normalization (Limb Darkening Removal). The brightness of filaments and of other solar disk features diminishes from the disk center toward the edge, due to limb darkening. This phenomenon can be approximated by a mathematical function. Finding an exact transformation is, however, a difficult task. In the ideal model of the sun as a uniformly lit sphere, and a solar disk image as an orthogonal projection of the sun brightness, limb darkening can be described as follows:

$$B(\omega) = B_c \cos\omega \tag{3.7}$$

where B_c is the brightness level in the center of the solar disk, ω is the angular distance from the center, and $B(\omega)$ is the brightness level of the points on the solar sphere, at ω distance from the center. The actual brightness, however, does not behave like this model.

To improve results, the brightness level is approximated by a polynomial function of the radial distance from the solar disk center, as more suitable for further calculations than the usual function of angular distance (as described by Neckel and Labs [49]). Since the radius of the disk varies from image to image, the maximum radial distance is scaled to 1000. The data beyond the limb brightness level of 50 (after brightness normalization) are discarded, to eliminate seeing effect and to simplify further curve fitting. Based on the data gathered from 58 normalized solar images recorded in January and February 2002 at the BBSO, the average solar disk brightness level is calculated as a function of the scaled radial distance from the disk center. The brightness level function is approximated by a polynomial:

$$B(r) = c_0 + c_1 r + \ldots + c_n r^n \tag{3.8}$$

where r is the radial distance from the center, $B(r)$ is the brightness level at this distance and $c_0, c_1, \ldots, c_n$ are the coefficients of the polynomial of the n-th order.

The gathered average brightness data for r = 0 ...1000 are symmetrically duplicated for r = -1000 ... -1 to assure continuity of the approximation in the disk center, and the least-square curve fitting method is applied for polynomials of the 3 to 10-th order, yielding the following results (see also Figure 3.2):

Table 3.1 Polynomial Least-square Curve Fitting Results

Polynomial order	3	4	5	6	7	8	9	10
Correlation	0.897128	0.97397	0.97397	0.991488	0.991488	0.99702	0.99702	0.999301
Average absolute error value	8.500201	4.209949	4.209949	2.447857	2.44786	1.5424	1.542395	0.746936
Maximum absolute error value	81.1135	49.6285	49.6285	31.2198	31.2198	19.4019	19.4019	11.0396
c_0	207.186	195.286	195.286	201.124	201.124	197.816	197.816	199.945
c_1	-5.90×10^{-17}	-3.84×10^{-16}	2.58×10^{-16}	4.88×10^{-16}	-5.24×10^{-16}	-8.34×10^{-16}	-5.93×10^{-16}	1.65×10^{-15}
c_2	-8.36×10^{-5}	3.50×10^{-5}	3.50×10^{-5}	-8.71×10^{-5}	-8.71×10^{-5}	3.14×10^{-5}	3.14×10^{-5}	-8.51×10^{-5}
c_3	-1.07×10^{-22}	3.49×10^{-22}	-9.24×10^{-22}	-1.02×10^{-21}	2.92×10^{-21}	2.81×10^{-21}	-1.70×10^{-21}	-3.33×10^{-21}
c_4	–	-1.38×10^{-10}	-1.38×10^{-10}	2.28×10^{-10}	2.28×10^{-10}	-4.23×10^{-10}	-4.23×10^{-10}	5.84×10^{-10}
c_5	–	–	8.23×10^{-28}	8.73×10^{-28}	-3.72×10^{-27}	-2.36×10^{-27}	1.88×10^{-26}	7.82×10^{-27}
c_6	–	–	–	-2.68×10^{-16}	-2.68×10^{-16}	8.59×10^{-16}	8.59×10^{-16}	-2.16×10^{-15}
c_7	–	–	–	–	8.87×10^{-34}	-6.24×10^{-34}	-3.43×10^{-32}	-1.36×10^{-32}
c_8	–	–	–	–	–	-6.03×10^{-22}	-6.03×10^{-22}	3.06×10^{-21}
c_9	–	–	–	–	–	–	1.74×10^{-38}	7.92×10^{-39}
c_{10}	–	–	–	–	–	–	–	-1.54×10^{-27}

The polynomial of the 10-th order is used for further calculations. To remove limb darkening, new brightness values of every pixel in the solar disk are calculated according to the following formula:

$$B_n(x,y) = B_o(x,y) \cdot \frac{200}{B(r_a)} \tag{3.9}$$

where $B_n(x,y)$ is the new brightness value of a solar pixel (x,y) after limb darkening removal, $B_o(x,y)$ is the original brightness value of this pixel, and $B(r_a)$ is the average brightness level of the pixel with the adjusted radial distance r_a from the disk center, calculated according to Equation 3.8. The value of r_a is given by the following formula:

$$r_a = \sqrt{(x_c - x)^2 + (y_c - y)^2} \cdot \frac{1000}{R} \tag{3.10}$$

where (x_c, y_c) are coordinates of the disk center, and R is the disk radius.

The brightness level of the pixels outside the solar disk as well as of the outer 5% of the disk pixels (containing no valuable solar filament data) is set to the maximum brightness value to facilitate further processing (see Figure A.29).

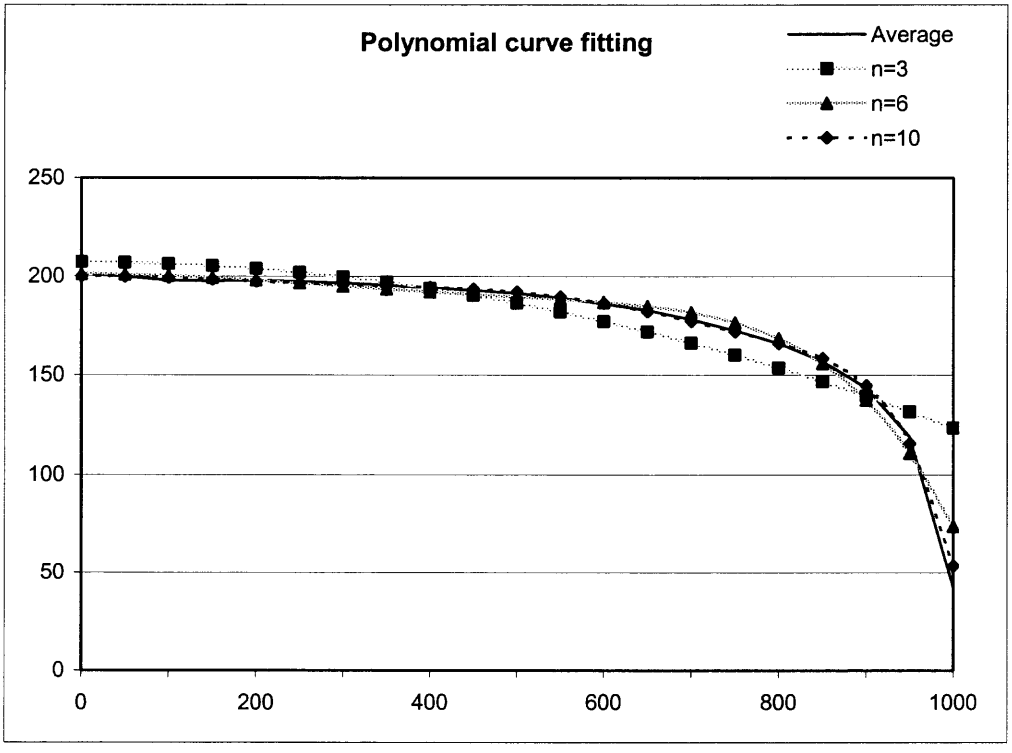

Figure 3.2 Polynomial curve fitting results for limb darkening approximation.

3.1.3.4 Sunspot Removal. Sunspots, as dark solar features, can be misrecognized as solar filaments in further solar image processing steps. Since sunspots are usually darker than filaments, they can be easily removed from the normalized solar image by applying global thresholding with threshold level below the usual filament brightness range. Using the threshold value of 140, the extracted sunspot areas are used as seeds for region growing in the normalized image above the filament threshold level (the brightness value of 186 is used as the region growing limit). The resulting sunspot regions are removed from the normalized image (using region image inversion and logical union with the normalized image) before further processing steps.

3.1.3.5 Area Normalization. Using the calculated disk center and radius, the disk is transformed to achieve a uniform area of solar features throughout the disk. The transformation applied is an equal-area projection with 90% of the visible hemisphere transformed (and scaled back to the original disk size). After this transformation the features have a uniform area, but their shapes are distorted toward the edges and the visual data are more reliable in the disk center.

A sphere of a radius R can be described by

$$x^2 + y^2 + z^2 = R^2 \tag{3.11}$$

The equal-area projection can be defined as

$$r' = \sqrt{x^2 + y^2 + (R - z)^2} \tag{3.12}$$

where r' is the radial distance of the projected point from the center of projection. By substituting

$$x^2 + y^2 = r^2 \tag{3.13}$$

in Equation 3.12, where r is the radial distance of the original point from the center of projection, we obtain

$$r' = \sqrt{r^2 + (R - z)^2} \tag{3.14}$$

Since the solar disk image can be considered as a scaled orthographic projection of an actual solar sphere, the value of z is unknown, but from Equations 3.11 and 3.13, we derive

$$z = \sqrt{R^2 - r^2} \tag{3.15}$$

By substituting value of z in Equation 3.14, we obtain

$$r' = \sqrt{r^2 + R^2 - 2R\sqrt{R^2 - r^2} + R^2 - r^2} \tag{3.16}$$

$$r' = \sqrt{2R^2 - 2R\sqrt{R^2 - r^2}} \tag{3.17}$$

$$r' = R\sqrt{2\left(1 - \sqrt{1 - \frac{r^2}{R^2}}\right)} \tag{3.18}$$

Since the diameter of the resulting equal-area projection is larger than the original image by a factor of $\sqrt{2}$, the projection was scaled back to the original size:

$$r'' = R\sqrt{1 - \sqrt{1 - \frac{r^2}{R^2}}} \tag{3.19}$$

where r'' is the scaled radial distance of the projected point from the center of projection. The inverse transformation (used to assure correct values for every pixel in the projected image) can be obtained as

$$r = r''\sqrt{2 - \frac{r''^2}{R^2}} \tag{3.20}$$

The resulting image is shown in Figure A.33. Since close to the disk edge the distortion of the projected features is very high, the outer 10% of the disk is removed to prevent the filament detection system from extracting features in the unreliable regions.

3.1.3.6 Global Thresholding. The final step of preprocessing is brightness thresholding. Using the threshold value of 185, most of the disk dark features are cleanly separated, including the majority of filaments, as shown in Figures 10 and 11. A similar operation with different single or multiple thresholding values may be used for the extraction of other solar features, such as sunspots, flares, plages, etc.

3.2 Feature Extraction

The next step is the extraction of filaments from the black and white preprocessed solar image. A few techniques based on mathematical morphology are considered. The goal is to achieve more precise and faster results than the region merging techniques implemented by Gao, Wang and Zhou [26].

3.2.1 Basic Mathematical Morphology Definitions

Mathematical morphology techniques are based on set theory and are used for processing of the structural features of an image in the spatial domain, such as morphological filtering, thinning and pruning [30]. The following mathematical morphology definitions will be used in next sections:

Let A and B be sets in 2-D integer space Z^2, with components $a = (a_1, a_2)$ and $b = (b_1, b_2)$, respectively. The translation of A by $x = (x_1, x_2)$, denoted $(A)_x$, is defined as

$$(A)_x = \{c \mid c = a + x, \text{ for } a \in A\} \tag{3.21}$$

The reflection of A, denoted $\hat{A}$, is defined as

$$\hat{A} = \{x \mid x = -a, \text{ for } a \in A\} \tag{3.22}$$

The complement of set A is

$$A^c = \{x \mid x \notin A\} \tag{3.23}$$

The difference of two sets A and B, denoted $A - B$, is defined as

$$A - B = \{x \mid x \in A, x \notin B\} = A \cap B^c \tag{3.24}$$

Two basic operations frequently used in mathematical morphology are dilation and erosion. Many interesting techniques may be obtained by using these two techniques separately, applying them multiple times to an image, or by using them together sequentially in various orders.

With A and B as sets in Z^2 and $\varnothing$ denoting an empty set, the dilation of A by B, denoted as $A \oplus B$, is defined as

$$A \oplus B = \{x \mid (\hat{B})_x \cap A \neq \varnothing\} \tag{3.25}$$

Therefore, the dilation of A by B is the set of all x displacements such that $\hat{B}$ and A overlap by at least one nonzero element. Based on this interpretation, Equation 3.25 may be rewritten as

$$A \oplus B = \{x \mid [(\hat{B})_x \cap A] \subseteq A\} \tag{3.26}$$

Set B is commonly referred to as the structuring element in dilation, as well as in other morphological operations.

For sets A and B in Z^2, the erosion of A by B, denoted $A \ominus B$, is defined as

$$A \ominus B = \{x \mid (B)_x \subseteq A\} \tag{3.27}$$

The erosion of A by B is the set of all points x such that B, translated by x, is contained in A.

Dilation and erosion are duals of each other with respect to set complementation and reflection. That is,

$$(A \ominus B)^c = A^c \oplus \hat{B} \tag{3.28}$$

Two other useful mathematical morphology operations, opening and closing, may be defined as combinations of dilation and erosion.

The opening of set A by structuring element B, denoted $A \circ B$, is defined as

$$A \circ B = (A \ominus B) \oplus B \tag{3.29}$$

The closing of set A by structuring element B, denoted $A \bullet B$, is defined as

$$A \bullet B = (A \oplus B) \ominus B \tag{3.30}$$

Dilation adds pixels to the original shape (A) around its periphery to increase its dimension. It may merge small features of the shape and close smalls gaps. Erosion removes the pixels from the original shape around its boundary. It may delete small shapes altogether, remove small features from an object and enlarge holes in it. Opening generally smoothes the contour of an image, breaks narrow joints between image elements, and eliminates protrusions. Closing also tends to smooth sections of contours, but as opposed to opening, it generally joins elements of the image separated by narrow breaks, closes long thin fissures, eliminates small holes, and fills gaps in the contour.

3.2.2 Simple Morphological Operations

The morphological operations described above are applied to filament detection. After preprocessing filaments are visible as large, elongated black gaps in a black-and-white solar image. All other features on the solar disk are also visible as black areas, but of small sizes (with the exception of sunspots, which can be described as huge, roughly circular black regions of the disk). The objective of applying morphological operations to solar images is to eliminate all solar disk features except for filaments and, if possible, to merge separate sections of the filaments.

The simplest approach evaluated is a sequence of dilations followed by a sequence of erosions. A single closing operation (i.e., a dilation followed by an erosion) with a small structuring element is obviously not sufficient for elimination of unnecessary features; therefore a sequence of dilations followed by a sequence of erosions with a 3×3 circular structuring element is applied. Note that the effect of such sequences with a small structuring element is similar to a single application of closing with a large structuring element of the same shape. However, its speed is significantly improved. The results of one and two iterations of dilation followed by the same number of iterations of erosion is shown in Figures A37-A.40. However, this method not only eliminates most of the unnecessary solar features, but also removes some small filaments and disconnects parts of big ones. Therefore, it is deemed as inadequate for filament detection.

3.2.3 Advanced Morphological Techniques

Since simple morphological operations cannot yield necessary results, more complex combinations of mathematical morphology methods are evaluated, as well as combinations of morphological methods with other image processing techniques.

Zana and Klein in their papers [78], [79], [80] described a method for vessel recognition in a noisy retinal angiography employing mathematical morphology techniques. The retinal images they processed contain a different set of features than solar images, but the basic structure to be extracted, tiny blood vessels, can be described similarly to solar filaments – as thin, elongated objects. Since the preprocessed solar image already contains binary information, some of the steps described by Zana and Klein are irrelevant, but a revised technique can be used for filament detection. The method employed here is an application of disjunctive granulometric filters using directional linear structuring elements, with theory laid out by Dougherty and Chen [23], Dougherty [22], some applications described by Soille, Breen, and Jones [61], and by Soille and Talbot [62].

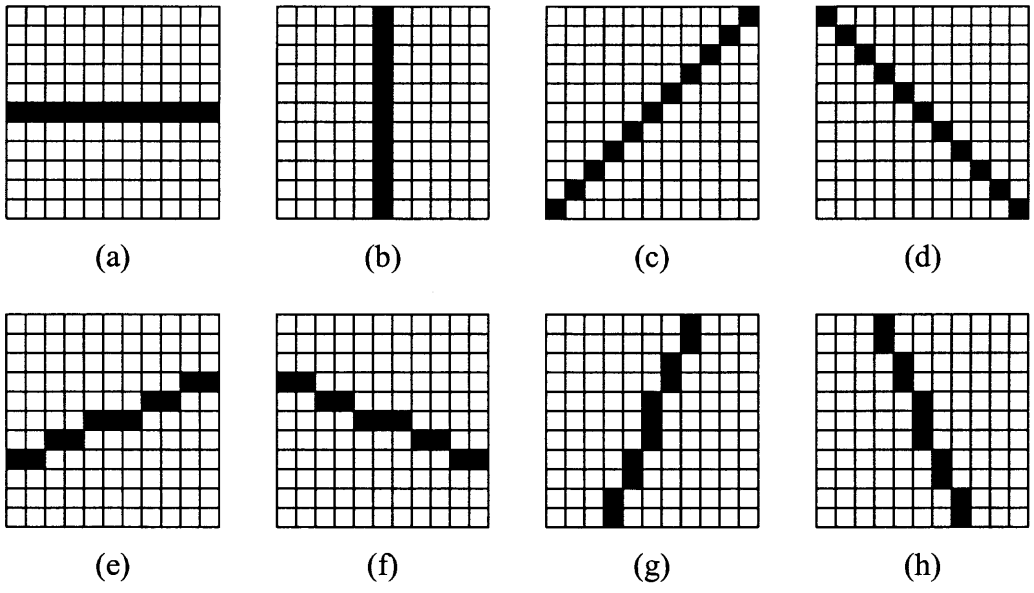

Figure 3.3 Eight directional linear 11 × 11 structuring elements with 90°, 0°, 45°, 135°, 67.5°, 112.5°, 22.5°, 157.5° slope, respectively.

The most important step in the process is the separation of elongated shapes (filaments) from the granular background. Instead of a supremum of openings (as proposed by Walter, Klein et al. [72]) used for discrimination of bright vessels in medical images, a superposition (implemented as logical intersection) of closings is used for the separation of dark filaments in solar images. A set of directional linear structuring elements is used, with the best results for elements with 11×11 size (see Figure 3.3).

Applying the basic four directional elements (Figure 3.3, elements a-d) renders promising results, but some filaments with non-vertical, non-horizontal or non-diagonal slope are missing and other filaments (especially the ones with high curvature) are separated into a few disconnected parts (see Figures A.41 and A.42). Applying the additional four directional elements (Figure 3.3, elements e-h) improves the result significantly (see Figures A.43 and A.44).

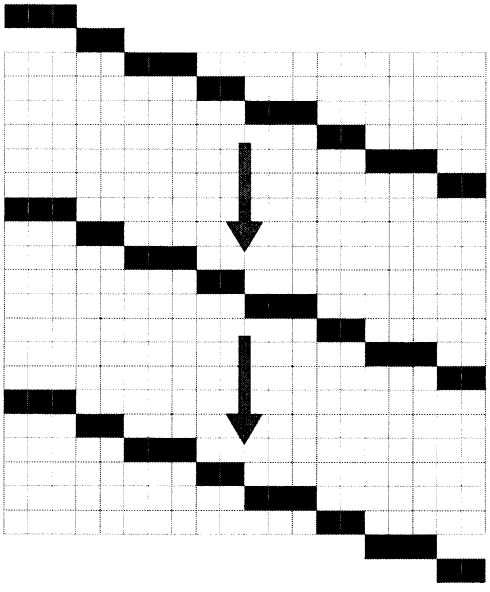

Figure 3.4 Directional buffer movement and pixel processing sequence for the recursive directional filtering.

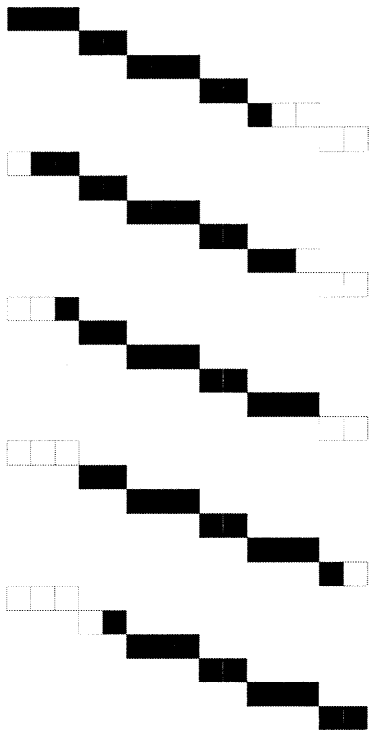

Figure 3.5 Different shapes of structuring elements with the same slope.

Most implementations of the directional filters use a square or rectangular structuring element, moving throughout the image. The processing time of this approach is proportional to the area of the structuring element. Soille, Breen, and Jones [61] proposed a recursive implementation of some morphological operations along discrete lines at arbitrary angles (see Figure 3.4). Their implementation does not depend on the length of the directional filter length, since it requires only three image brightness value comparisons per pixel. As applied to filament extraction, this method is approximately 18 times faster than the traditional implementation (see Table 3.3). The structuring element used in the recursive method (a section of a line with a given slope) is not translation invariant – its shape changes slightly as it is moved throughout the image (see Figure 3.5), but the line slope remains constant. A modification of this method proposed by

Soille and Talbot [62] is translation invariant as it applies all variants of the structuring element, but it requires more comparisons and depends on the slope of the line; therefore the method proposed by Soille, Breen, and Jones is used for filament extraction.

The final superposition contains multiple short thin lines, which may not be actual filaments, but granularity gaps or features in the sunspot vicinity. They may be eliminated by applying a closing operation with a 3×3 circular structuring element. Such an operation (see Figures A.47 and A.48) eliminates most of the spurious features, but applying this operation with a larger structuring element (or applying multiple dilations followed by the same number of erosions) removes also some minor.

The dark features obtained by the superposition of directional closing operations (with or without additional "cleaning" closings) may be used as seeds for a region growing operation. The method checks the neighborhood of the detected features and compares it against the original preprocessed image. All connected black points in the preprocessed image neighboring the detected filament are marked as belonging to the filament. Using 8-neighbor connectivity yields better results than using 4-neighbor connectivity.

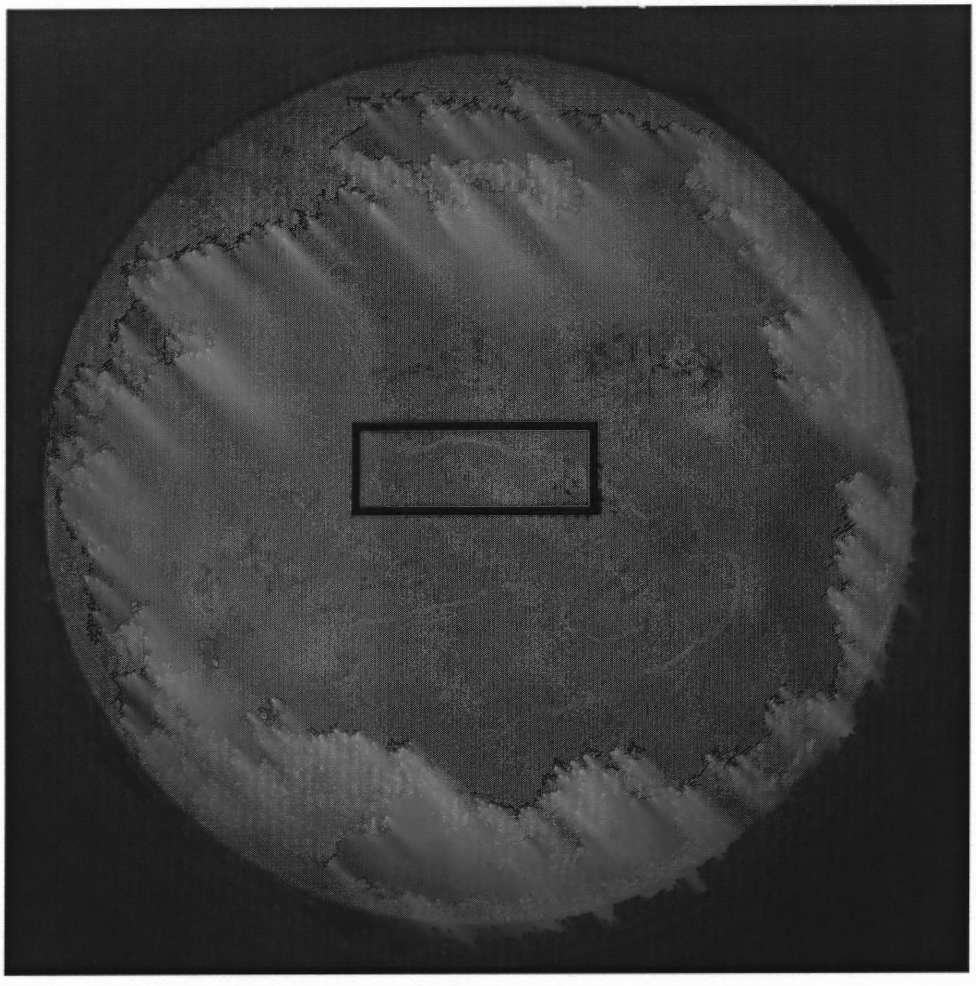

Figure 3.6 The original image of the solar disk (from BBSO [5]). A fragment with a filament used in further examples is marked with a black rectangle.

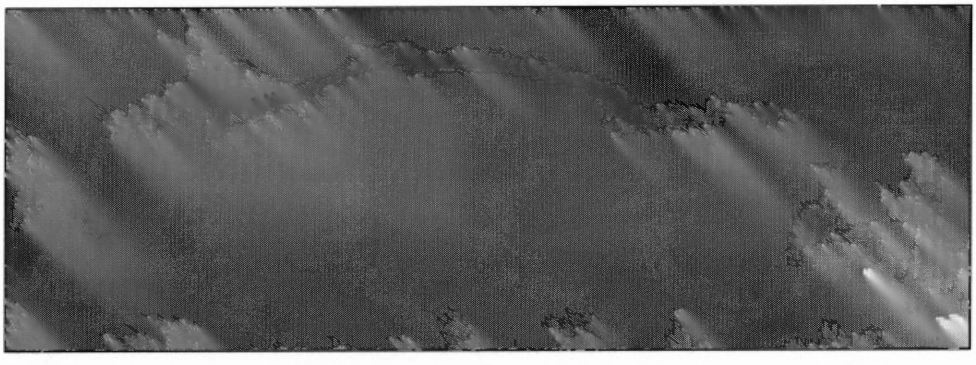

Figure 3.7 An example of a solar filament, unprocessed.

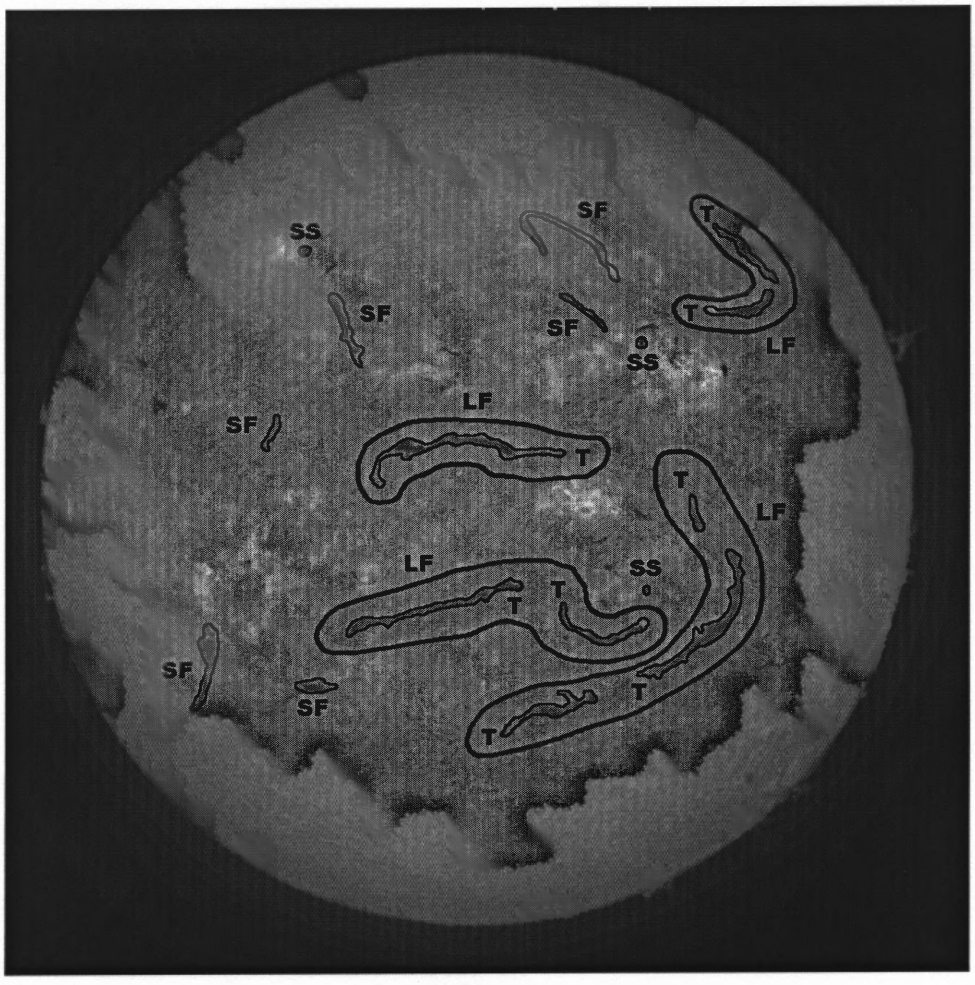

Figure 3.8 Solar disk with dark features marked (LF – large filaments, T – large filament segments, SF – small filaments, SS – sunspots).

3.3 Experimental Results

This section describes the experimental results of the filament detection system described in this dissertation. The filament detection rate and processing time are based on processing of ten solar images gathered by BBSO in January, 2002.

Performance of the filament detection system is compared against the method presented by Gao, Wang, and Zhou [26]. One of the original grayscale images (1016 by 1016 pixels) used in the evaluation, with all the dark features marked manually, is shown

in Figure 3.8. There are six large filaments (labeled LF in the figure), eight large filament segments (labeled T), six small filaments (labeled SF) and three sunspots (labeled SS) present in the picture.

Table 3.2 presents the results of filament detection techniques. The methods referred to in this table (and in the following tables) are described below:

- Method I – the method presented by Gao, Wang, and Zhou; the result is shown in Figures 3.9, A.49 and A.50.
- Method II – the first preprocessing method described in this dissertation (local thresholding with cutoff margins and modifying factor) combined with the morphological operations (superposition of eight traditional directional closings, "cleaning" closing and simple region growing); the result is shown in Figures A.51 and A.52.
- Method III - the first preprocessing method combined with the superposition of eight recursive directional filtering, "cleaning" closing and simple region growing; the result is shown in Figures A.53 and A.54.
- Method IV – the second preprocessing method (brightness normalization, limb darkening and sunspot removal, global thresholding) with the superposition of eight traditional directional closings, "cleaning" closing and simple region growing; the result is shown in Figures A.55 and A.56.
- Method V – the second preprocessing method combined with the superposition of eight recursive directional filtering, "cleaning" closing and simple region; the result is shown in Figures A.57 and A.58.

- Method VI – similar to Method IV, with additional equal area normalization in the preprocessing stage; the result is shown in Figures A.59 and A.60.
- Method VII – similar to Method V, with additional equal area normalization in the preprocessing stage; the result is shown in Figures A.61 and A.62.

Table 3.2 Filament Detection Results

Method	LF[a] (%)	LFS[b] (%)	SF[c] (%)	SMF[e]	AFMF[f]
Method I	50.2	33.3	5.1	0.0	0.2
Method II	100.0	97.1	90.1	0.7	10.8
Method III	100.0	98.1	90.4	0.7	10.5
Method IV	98.3	84.9	72.8	0.0	5.3
Method V	96.7	85.4	74.2	0.0	5.5
Method VI	94.7	80.3	56.5	0.0	4.3
Method VII	94.3	80.1	54.9	0.0	4.0

[a] LF – average detection rate of large filaments
[b] LFS – average detection rate of large filament segments
[c] SF – average detection rate of small filaments
[e] SMF – average number of sunspots misrecognized as filaments
[f] AFMF – average number of additional features misrecognized as filaments

The average preprocessing and feature extraction time, and the average, minimum and maximum total processing time for ten selected solar images are presented in Table 3.3. The results are produced on a single-processor 1.2 MHz AMD Athlon PC with 512 MB of physical memory.

Table 3.3 Processing Time for Preprocessing and Feature Extraction Stages

Method	Average preprocessing time (ms)	Average feature extraction time (ms)	Average total time (ms)	Minimum total time (ms)	Maximum total time (ms)
Method I	N/A	1672.3	1672.3	851	2143
Method II	1194.9	94503.9	95698.8	95678	95718
Method III	1193.8	6286.1	7479.9	7471	7501
Method IV	1364.0	93653.4	95017.4	95006	95047
Method V	1361.8	5507.0	6868.8	6850	6880
Method VI	1711.5	93644.6	95356.1	95347	95377
Method VII	1710.5	5515.0	7225.5	7201	7241

The method presented by Gao, Wang, and Zhou uses the images that are already preprocessed (with dark current and flat field correction, removed limb darkening and enhanced contrast) during the image acquisition process at BBSO; therefore it is compared against the feature extraction stage of the other methods described in this dissertation. The filament detection technique described in [26] is based on binary thresholding with the half of the image median value as a threshold, followed by region growing. Pieces of filament segments are merged within 80-pixel neighborhood, and all segments within 40-pixel distance are merged into a single filament. Filaments with the total area smaller than a preset area threshold (50 pixels) are ignored. The method detects on average 50.2% of large filaments, 33.3% of their segments, and only 5.1% of small filaments; however, there is a very low number of other dark features (including sunspots) recognized incorrectly as filaments. The low filament detection rate for this

method is caused mainly by using global thresholding based on the median value. The second stage, region growing, merges pieces of large filaments correctly and filters out all unnecessary dark features. Unfortunately, it also removes most of the small filaments and some segments of the large ones. The processing time (the shortest among all the methods compared) is highly dependent on the number of the dark features in the image and can not be significantly reduced by parallelization due to the nature of median and region growing algorithms.

The new filament detection technique based on directional morphological filtering achieves excellent results in detecting large filaments and good results for small filaments. The technique, however, misrecognizes some additional dark features as filaments. This deficiency may be improved in the future with an additional step of rejecting features which are too small or improperly shaped.

Application of the first preprocessing method (modified local thresholding, used in Method II and III) results in a higher overall filament detection rate, but it is unable to reject all sunspots and incorrectly recognizes many dark features as filaments.

The second preprocessing method (based on image normalization, used in Method IV and V) is slightly slower than the first one, but it is more suitable for separating solar features into a few categories due to their brightness level (therefore, it is able to remove sunspots from the image). Large part of this preprocessing technique (limb darkening and sunspot removal, thresholding) can be parallelized, leading to reduced processing time.

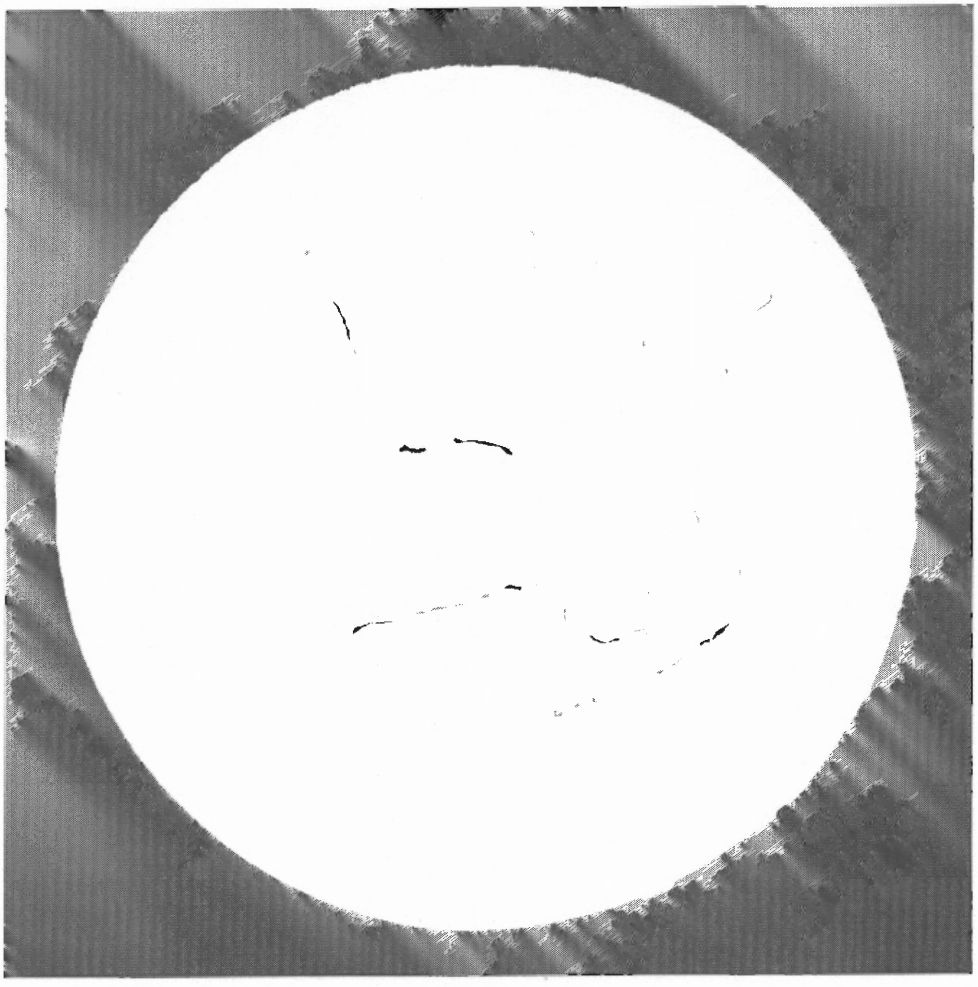

Figure 3.9 Solar disk with Gao, Wang, and Zhou's method applied (the black features are detected filaments, gray areas were rejected due to size limitations or closeness to the disk limb).

The second preprocessing method with the additional equal area projection step (used in Method VI and VII) achieves lower filament detection rate and is slightly slower than the other new methods. It is more suitable for systems tracking precise filament size changes, as it extracts area-corrected filaments.

The difference between two new feature extraction techniques (based on traditional and recursive implementation of morphological operations) is small in terms of filament detection rates, and is mainly due to the slightly different structuring element

shape. The processing time, however, is substantially reduced for the recursive implementation. Therefore, only the second implementation is used for noisy image processing. All methods described in this dissertation allow for real-time implementation of the filament detection system (assuming 1-minute solar image acquisition intervals).

3.4 Noisy Solar Image Processing

The method proposed in this dissertation has also been applied to a set of noisy images produced by adding simulated noise of various nature to one of the original images. Application of Gaussian noise (see Figures A.63 and A.64) simulates random and electronic equipment-related interference, while application of smoothing (Gaussian blur and low pass filtering, see Figures A.67 and A.68) simulates the effect of seeing and light high altitude cloudiness, particularly common in solar observations.

The results of Gao, Wang, and Zhou's method application to the images with Gaussian noise are satisfactory (see Table 3.4), but the filament detection rate for the blurred images is very low, possibly due to the unfavorable relative brightness changes of the image features. Since blurring occurs frequently in solar observations, this method is not very suitable for processing images gathered during unfavorable atmospheric conditions.

Table 3.4 Results of Filament Detection in Noisy Images (Method I)

Image noise	LF[a] (%)	LFS[b] (%)	SF[c] (%)	SMF[e]	AFMF[f]
Gaussian noise, 10% noise level, 100% distribution	100.0	75.0	16.7	0	0
Gaussian noise, 100% noise level, 10% distribution	100.0	62.5	16.7	0	0
Gaussian noise, 25% noise level, 25% distribution	75.0	50.0	16.7	0	0
Gaussian noise, 50% noise level, 50% distribution	100.0	87.5	16.7	0	0
Gaussian blur, 1 pixel	75.0	37.5	0.0	0	0
Gaussian blur, 3 pixels	0.0	0.0	0.0	0	0
Low pass, 1 pixel	75.0	37.5	16.7	0	0
Low pass, 5 pixels	0.0	0.0	0.0	0	0

[a] LF – average detection rate of large filaments
[b] LFS – average detection rate of large filament segments
[c] SF – average detection rate of small filaments
[e] SMF – average number of sunspots misrecognized as filaments
[f] AFMF – average number of additional features misrecognized as filaments

The results presented in Table 3.5 and in Figures A.65, A.66, A.69 and A.70 show that Method III (with modified local thresholding) is quite suitable for processing noisy images. The detection rate for large filaments is excellent, with satisfactory rate for smaller filaments. Slightly lower number of additional features is misrecognized as filaments due to smaller areas and discontinuities in the dark features.

Table 3.5 Results of Filament Detection in Noisy Images (Method III)

Image noise	LF[a] (%)	LFS[b] (%)	SF[c] (%)	SMF[e]	AFMF[f]
Gaussian noise, 10% noise level, 100% distribution	100.0	100.0	83.3	0	9
Gaussian noise, 100% noise level, 10% distribution	100.0	100.0	83.3	1	9
Gaussian noise, 25% noise level, 25% distribution	100.0	100.0	83.3	0	10
Gaussian noise, 50% noise level, 50% distribution	100.0	87.5	66.7	0	3
Gaussian blur, 1 pixel	100.0	100.0	83.3	0	8
Gaussian blur, 3 pixels	100.0	87.5	66.7	0	2
Low pass, 1 pixel	100.0	100.0	83.3	0	11
Low pass, 5 pixels	100.0	87.5	66.7	0	3

[a] LF – average detection rate of large filaments
[b] LFS – average detection rate of large filament segments
[c] SF – average detection rate of small filaments
[e] SMF – average number of sunspots misrecognized as filaments
[f] AFMF – average number of additional features misrecognized as filaments

Method V (with preprocessing based on image normalization) produces the results presented in Table 3.6. The filament detection rate is low for images with Gaussian noise applied, and is particularly poor for images with high-amplitude noise. On the other hand, the results for the blurred images are very good, deeming the method suitable for processing images gathered during imperfect weather conditions.

Table 3.6 Results of Filament Detection in Noisy Images (Method V)

Image noise	LF[a] (%)	LFS[b] (%)	SF[c] (%)	SMF[e]	AFMF[f]
Gaussian noise, 10% noise level, 100% distribution	100.0	87.5	83.3	0	3
Gaussian noise, 100% noise level, 10% distribution	25.0	12.5	0.0	0	1
Gaussian noise, 25% noise level, 25% distribution	50.0	37.5	66.7	0	0
Gaussian noise, 50% noise level, 50% distribution	0.0	0.0	0.0	0	0
Gaussian blur, 1 pixel	100.0	87.5	83.3	0	1
Gaussian blur, 3 pixels	100.0	87.5	66.7	0	0
Low pass, 1 pixel	100.0	87.5	83.3	0	2
Low pass, 5 pixels	100.0	87.5	83.3	0	0

[a] LF – average detection rate of large filaments
[b] LFS – average detection rate of large filament segments
[c] SF – average detection rate of small filaments
[e] SMF – average number of sunspots misrecognized as filaments
[f] AFMF – average number of additional features misrecognized as filaments

Similarly, Method VII (with an additional area normalization step in the preprocessing stage) produces poor results for images with Gaussian noise and good results for blurred images (see Table 3.7). The filament detection rate is slightly inferior to the results produced by the other methods, but it yields very low number of other dark features misrecognized as filaments.

Table 3.7 Results of Filament Detection in Noisy Images (Method VII)

Image noise	LF[a] (%)	LFS[b] (%)	SF[c] (%)	SMF[e]	AFMF[f]
Gaussian noise, 10% noise level, 100% distribution	100.0	87.5	66.7	0	1
Gaussian noise, 100% noise level, 10% distribution	0.0	0.0	0.0	0	0
Gaussian noise, 25% noise level, 25% distribution	25.0	12.5	50.0	0	0
Gaussian noise, 50% noise level, 50% distribution	0.0	0.0	0.0	0	0
Gaussian blur, 1 pixel	100.0	87.5	66.7	0	1
Gaussian blur, 3 pixels	100.0	87.5	50.0	0	0
Low pass, 1 pixel	100.0	87.5	66.7	0	1
Low pass, 5 pixels	100.0	87.5	50.0	0	0

[a] LF – average detection rate of large filaments
[b] LFS – average detection rate of large filament segments
[c] SF – average detection rate of small filaments
[e] SMF – average number of sunspots misrecognized as filaments
[f] AFMF – average number of additional features misrecognized as filaments

CHAPTER 4

FUTURE WORK

The method presented here consists of two alternative preprocessing techniques, separating dark features from a solar disk image, followed by a series of directional morphological filtering which extracts elongated shapes. It achieves excellent results in detecting large filaments and a good detection rate for small filaments. However, the method can be further improved to attain better performance and higher detection rate. This section proposes a few possible directions of further improvements and describes a few other areas of image processing, where this method may be applicable.

4.1 Performance Enhancements

The first preprocessing method (based on modified local thresholding) and a part of the second preprocessing method (based on image normalization), as well as the morphological operations used in feature extraction stage may be ported to a distributed parallel-processing platform. In such implementation, the performance of the system would be greatly enhanced, especially with the usage of Digital Signal Processors (DSP).

4.2 Filament Detection Improvements

The simple directional morphological filtering achieved satisfactory results in filament detection. The recursive implementation of directional filtering significantly improves processing time. However, some enhancements of the feature extraction method could improve its efficiency and the quality of separation of filaments from other dark solar features.

4.2.1 Multi-Resolution Detection

One of the possible performance improvements may include filament detection in images with different (lower) resolution. A large filament detected in a low-resolution image could be refined in a limited area of the original image. This method can be combined with most of the other proposed enhancements.

4.2.2 Other Morphological Operations

Further experiments with morphological operations may produce more precise filament detection methods. Alternating directional filtering with different sizes of the structuring elements can discriminate elongated shapes of desired size. More advanced post-processing morphological operations could separate valid filaments from similar solar dark features.

4.2.3 Additional Filament Detection Techniques

If more sophisticated filament feature extraction or more precise detection methods are needed, some additional techniques may be considered:

- Statistical snakes
- Probabilistic Saliency Approach
- Vector-Gradient Hough Transform
- Neighborhood tracking

4.3 Filament Tracking System

With some additional work on filament registration, the presented method can be used in tracking solar filaments and included in solar eruption early-warning systems. Another potential research direction includes the development of a filament tracking and statistical data gathering based on the filament space co-ordinates. A modified version of the filament detection system can also be useful in research of filament size oscillations. Additional system development may require designing and implementing efficient image compression and storage methods, as well as effective filament indexing for large solar image databases.

4.4 Other Solar Feature Detection

The system developed for filament detection may be modified to detect and explore statistical occurrences of some other solar features, such as flares, plages, faculae, filigrees, or sunspots. The adaptation of the system to new features would require adjustment of brightness level thresholds, size and shape of the structuring elements or feature area limits, but could use the same general method used for filament detection.

4.5 Applications in Other Areas

The proposed filament detection method may be applied in other areas of image processing with similar characteristics. Processing of planetary images may benefit from preprocessing methods presented in this dissertation and the directional morphological filtering technique may be suitable for planetary feature extraction based on feature brightness or shape. Another area of potential application of the developed method

includes images of environments resembling solar chromosphere – in hydrodynamics, gas dynamics, vortex dynamics, and other fluid dynamics research, as well as in earth satellitary image processing.

APPENDIX A

FIGURES OF SOLAR IMAGE PROCESSING RESULTS

The results of consecutive image processing operations performed on the original solar disk image (see Figures 3.6 and A.1) are presented in this appendix. In most cases, each page contains an image of the whole solar disk after a particular operation and an enlarged image fragment containing a single filament, marked with a rectangle in Figures 3.7 and A.2.

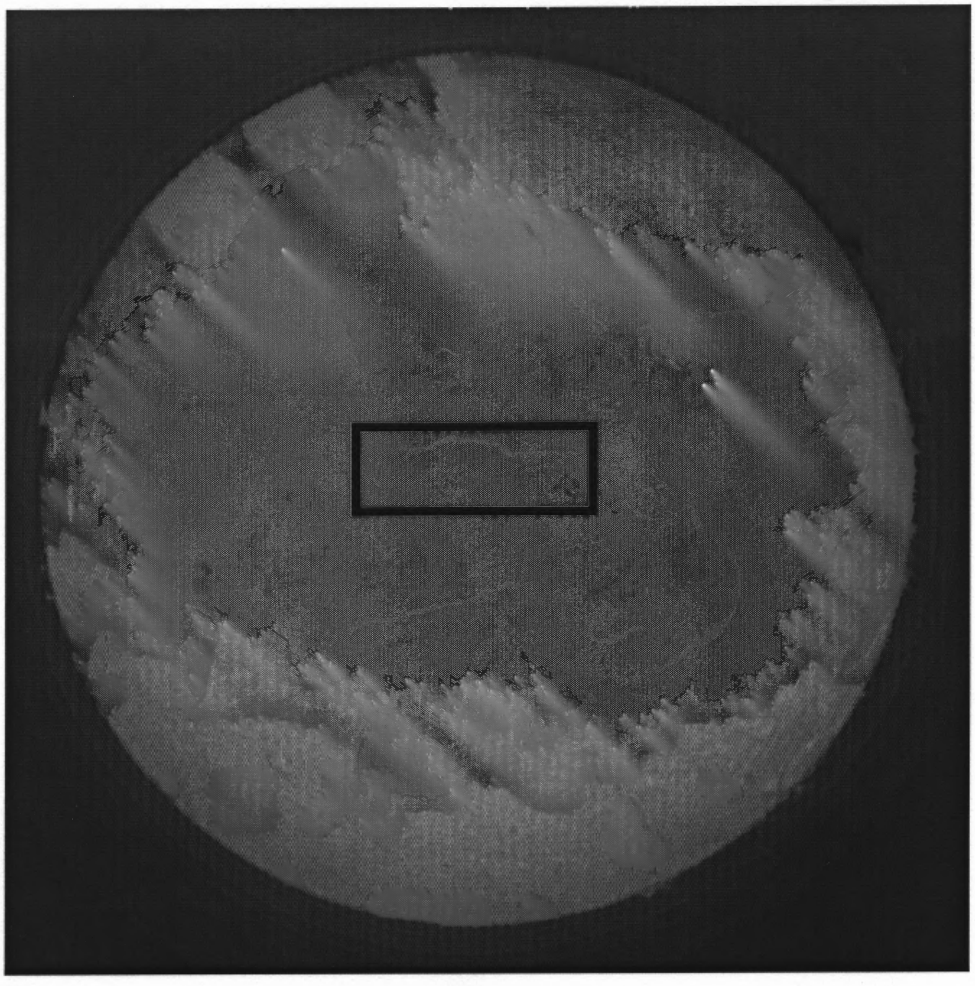

Figure A.1 The original image of the solar disk (from BBSO [5]). A fragment with a filament used in further examples is marked with a black rectangle.

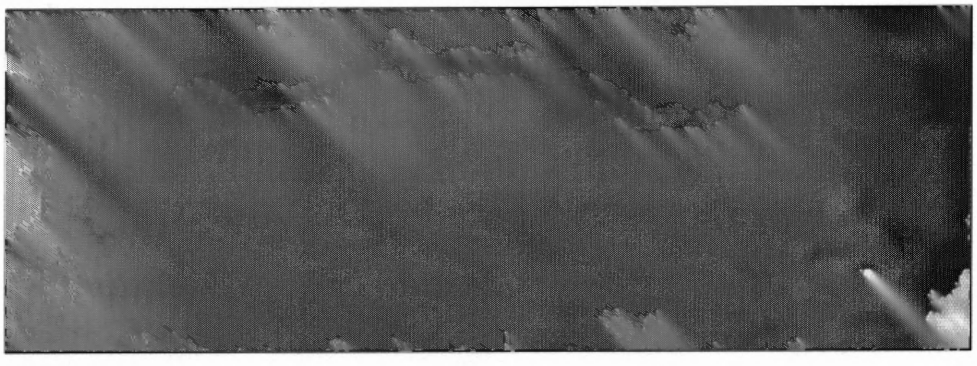

Figure A.2 An example of a solar filament, unprocessed.

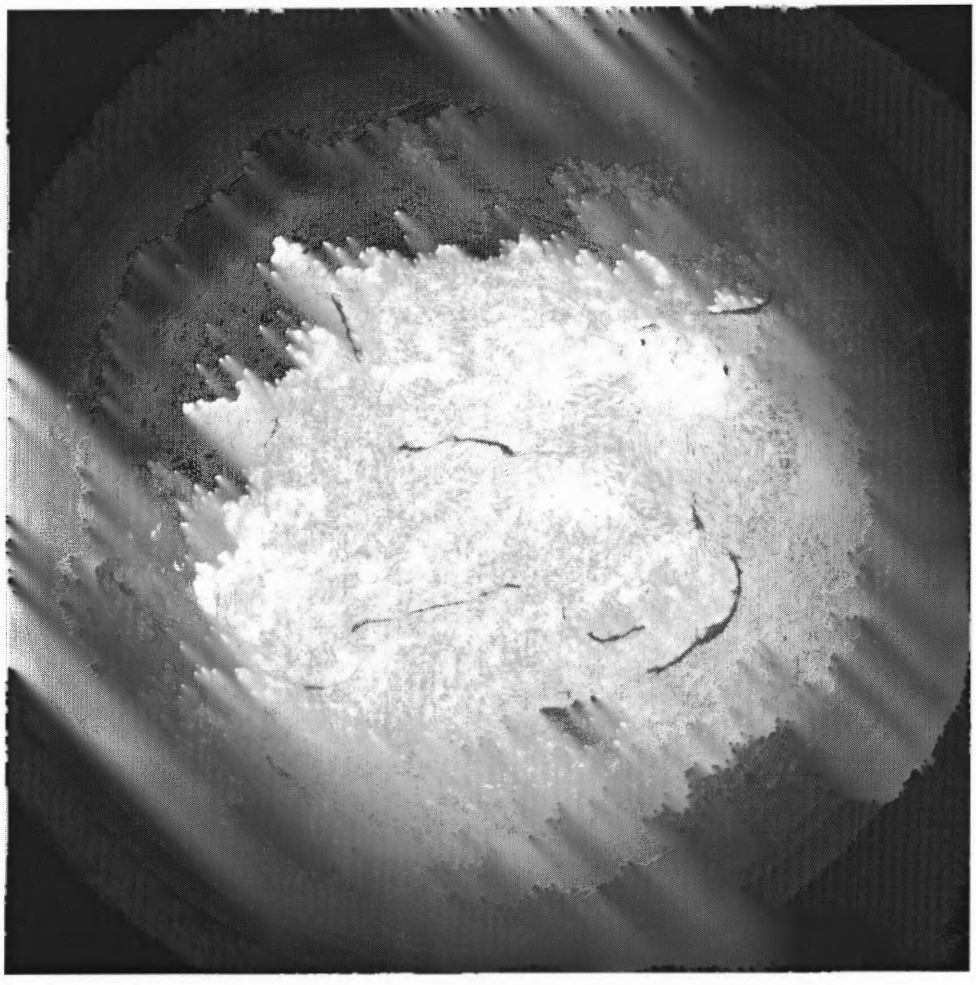

Figure A.3 Solar disk, global histogram equalization.

Figure A.4 Filament, global histogram equalization.

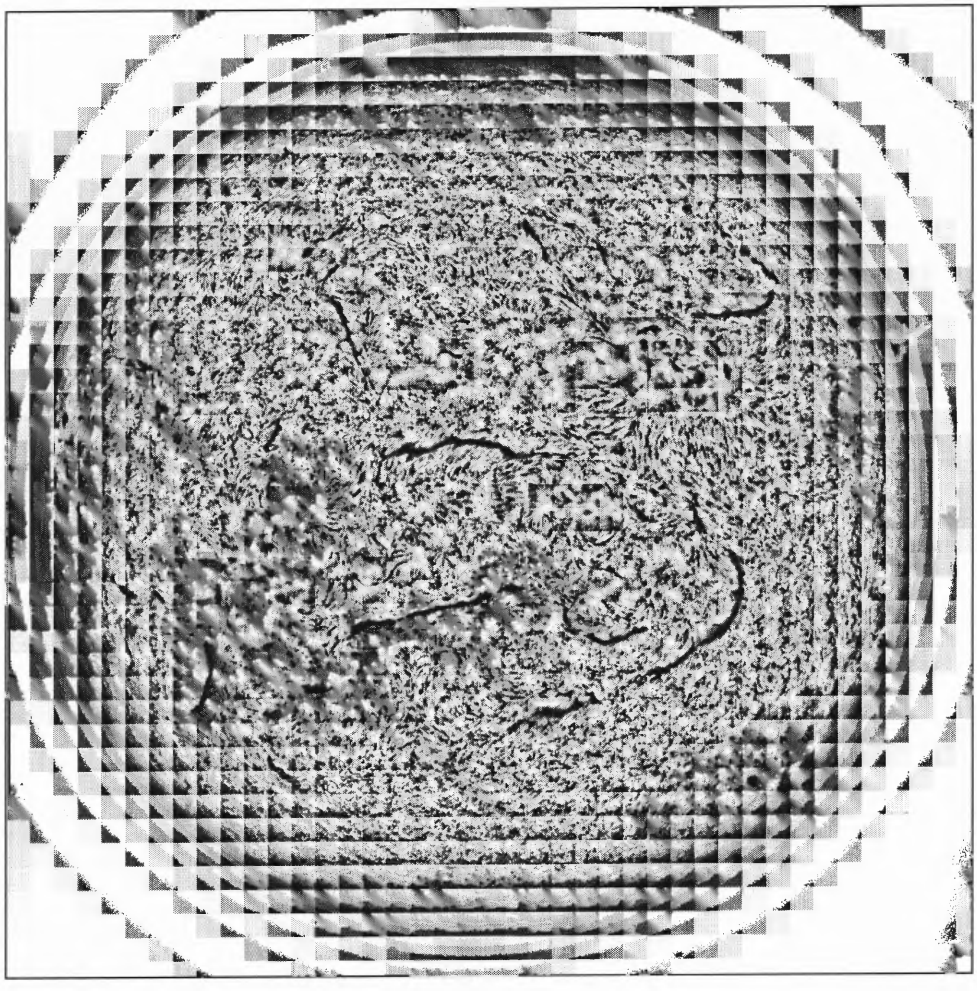

Figure A.5 Solar disk, local histogram equalization, window size w=25 pixels.

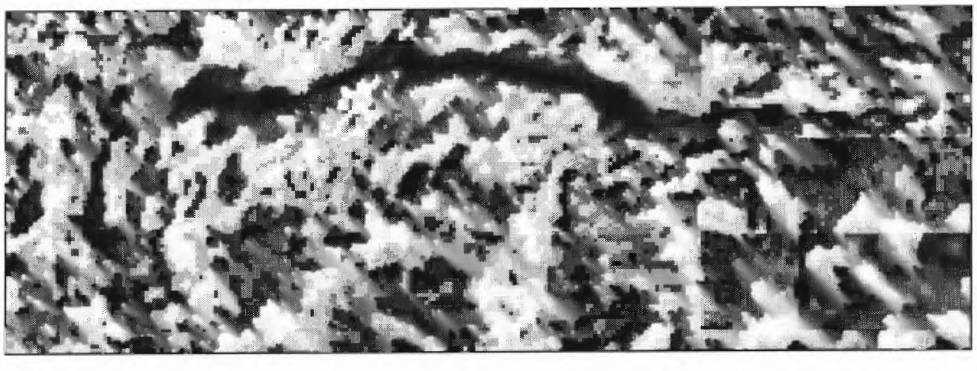

Figure A.6 Filament, local histogram equalization, window size w=25 pixels.

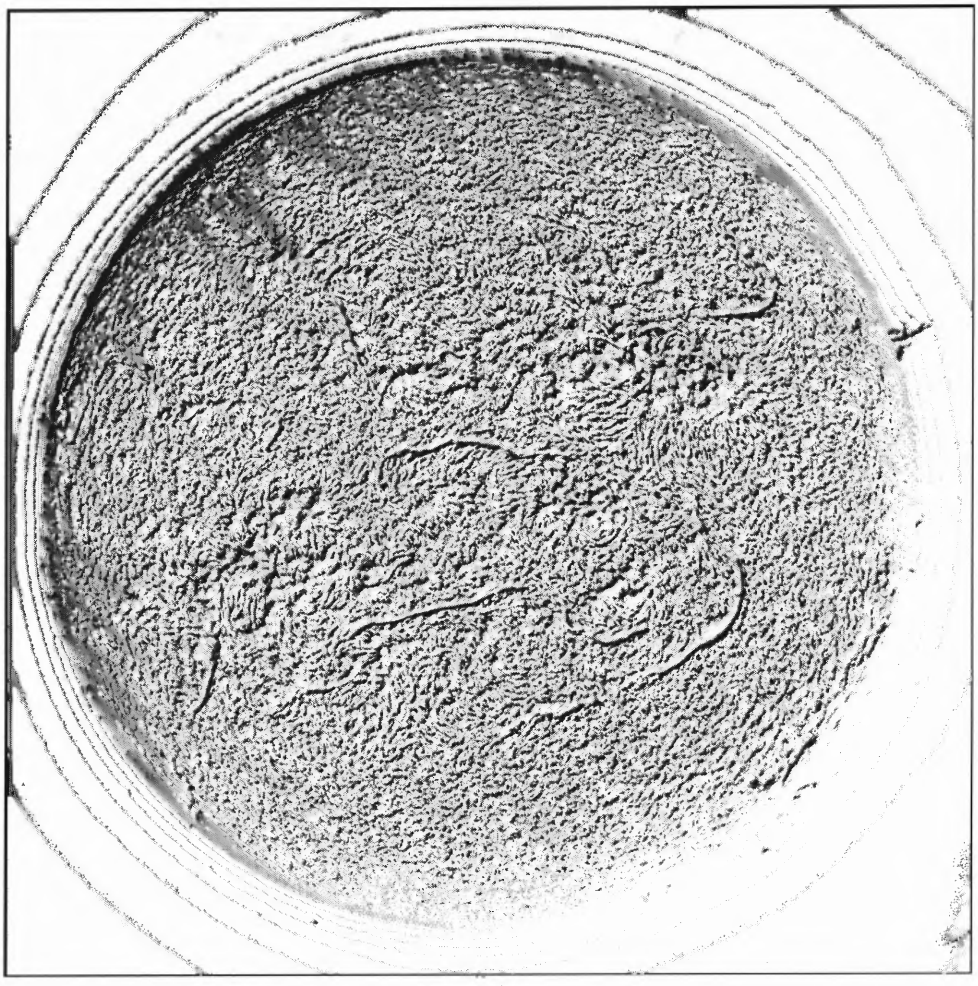

Figure A.7 Solar disk, smooth local histogram equalization, window size w=5 pixels.

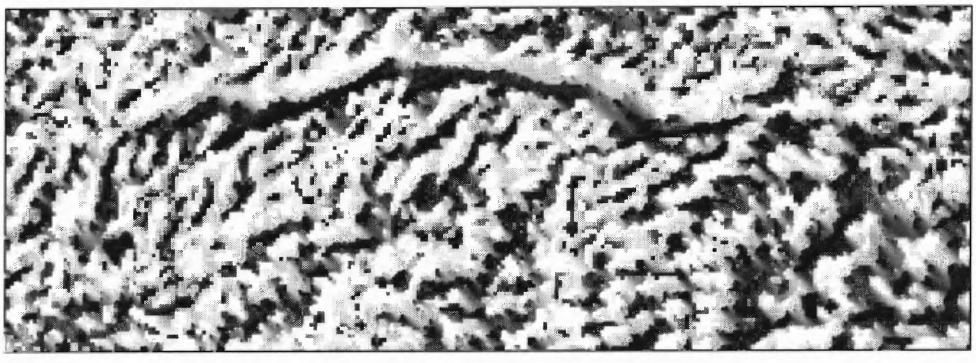

Figure A.8 Filament, smooth local histogram equalization, window size w=5 pixels.

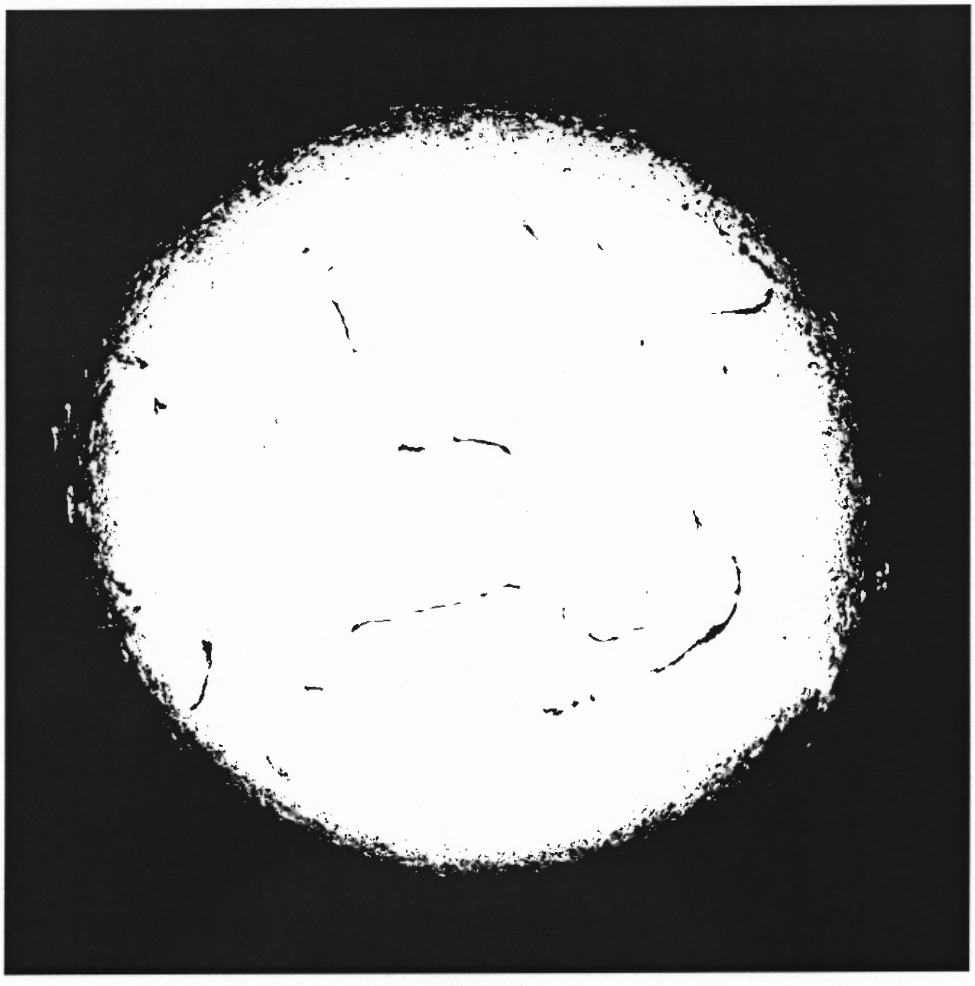

Figure A.9 Solar disk, global thresholding, T=130.

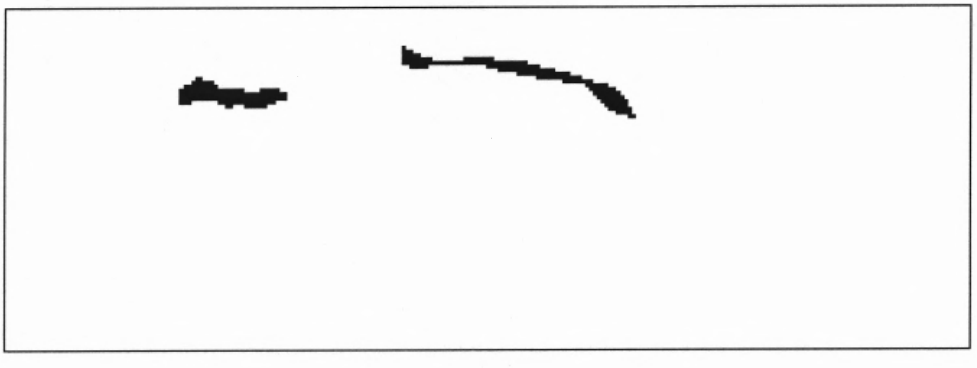

Figure A.10 Filament, global thresholding, T=130.

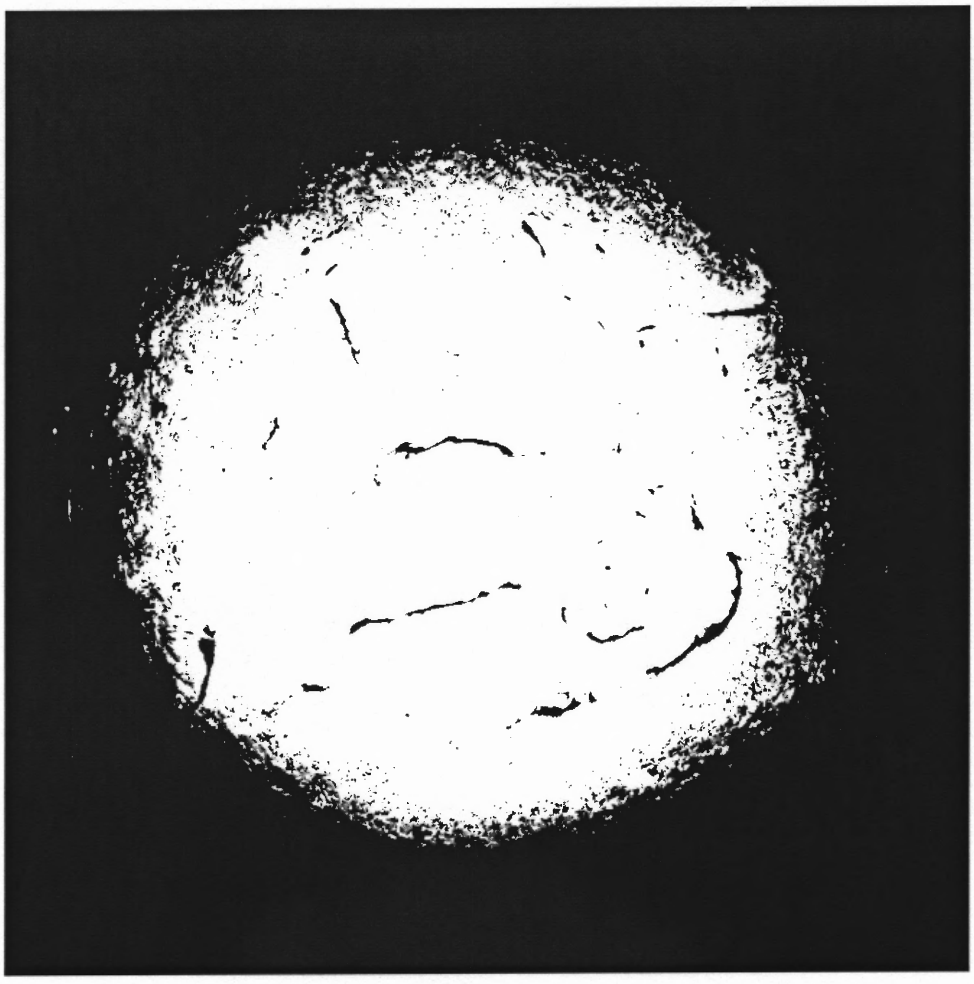

Figure A.11 Solar disk, global thresholding, T=140.

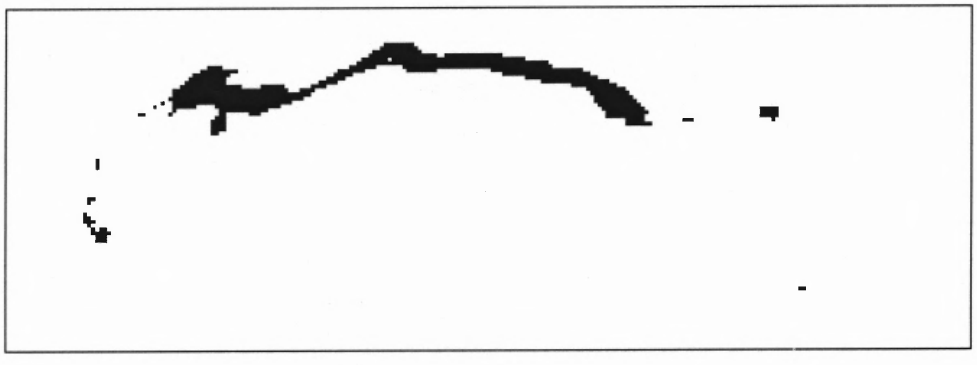

Figure A.12 Filament, global thresholding, T=140.

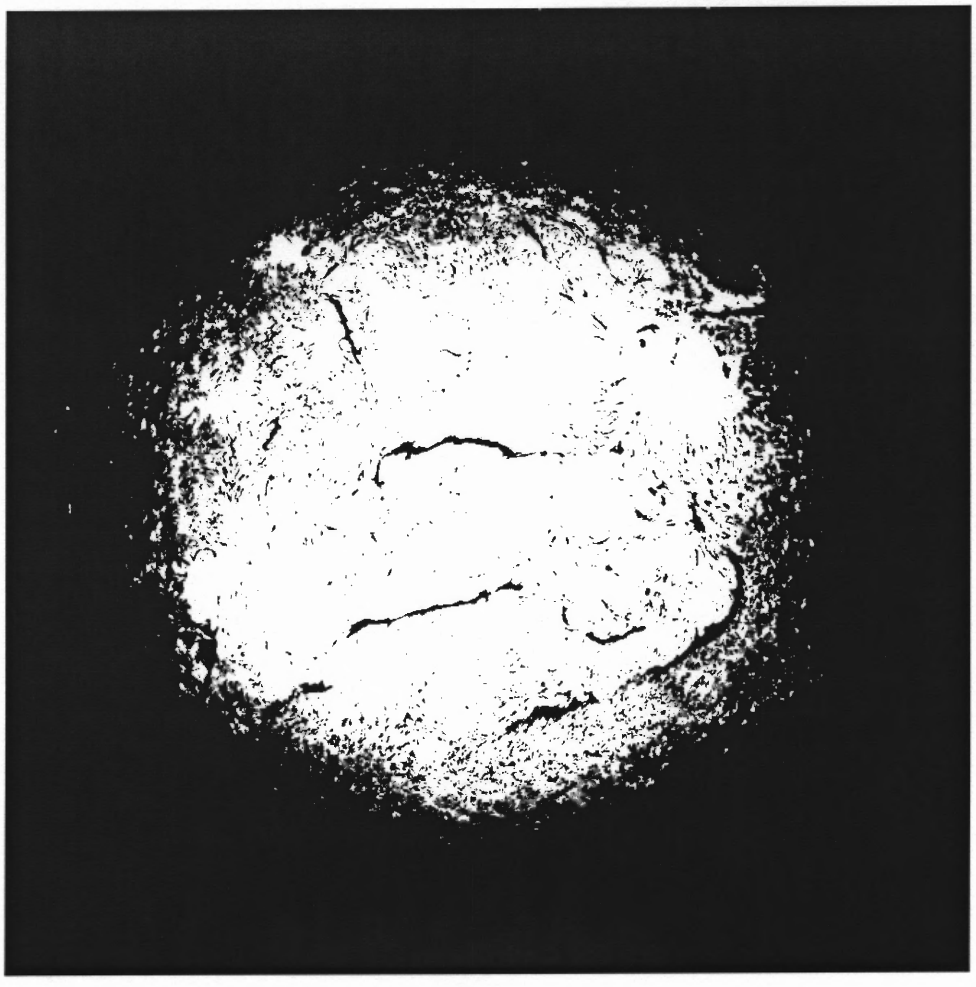

Figure A.13 Solar disk, global thresholding, T=150.

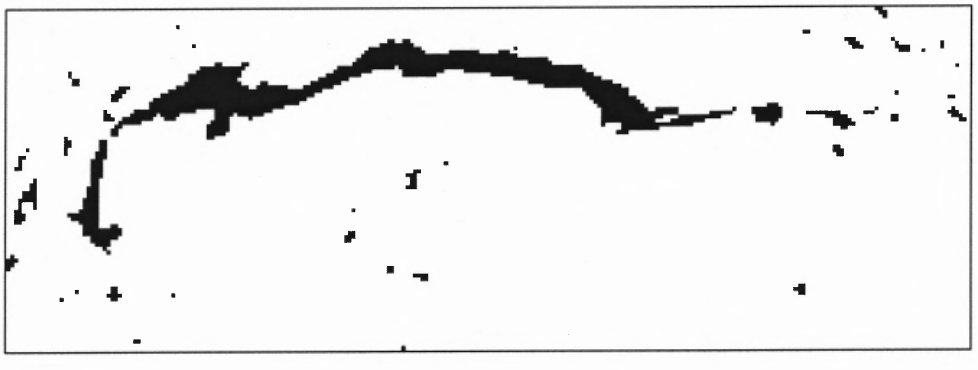

Figure A.14 Filament, global thresholding, T=150.

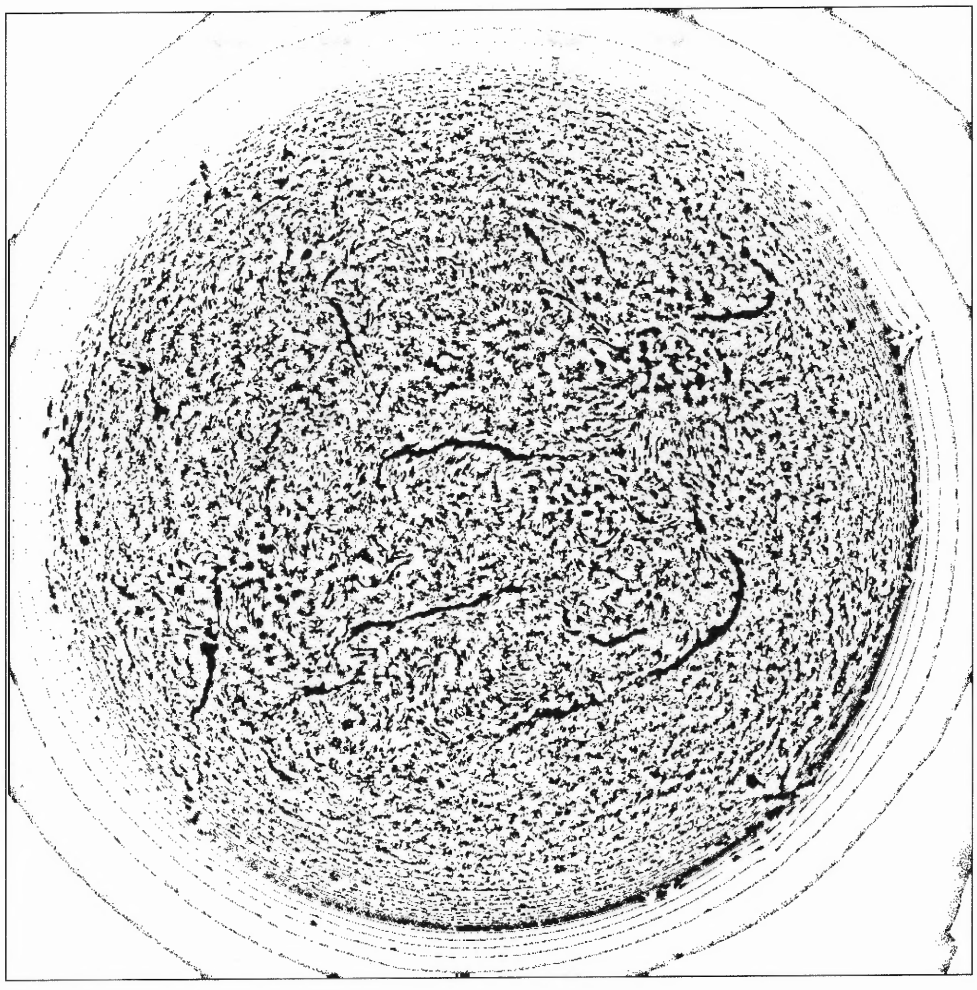

Figure A.15 Solar disk, local thresholding, window size w=20.

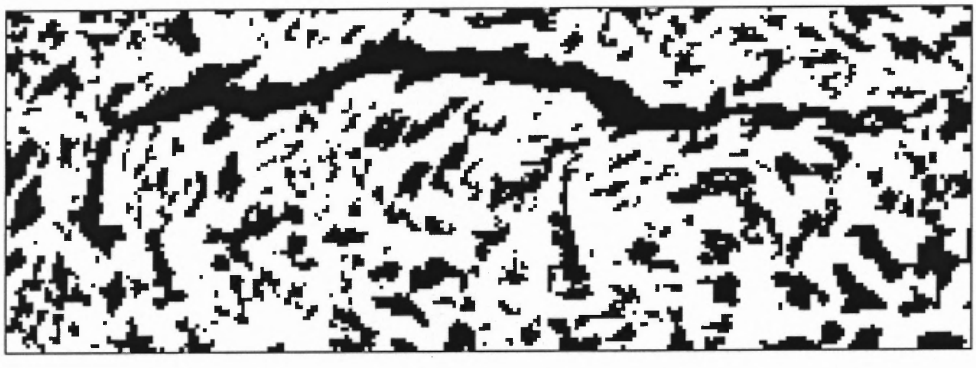

Figure A.16 Filament, local thresholding, window size w=20.

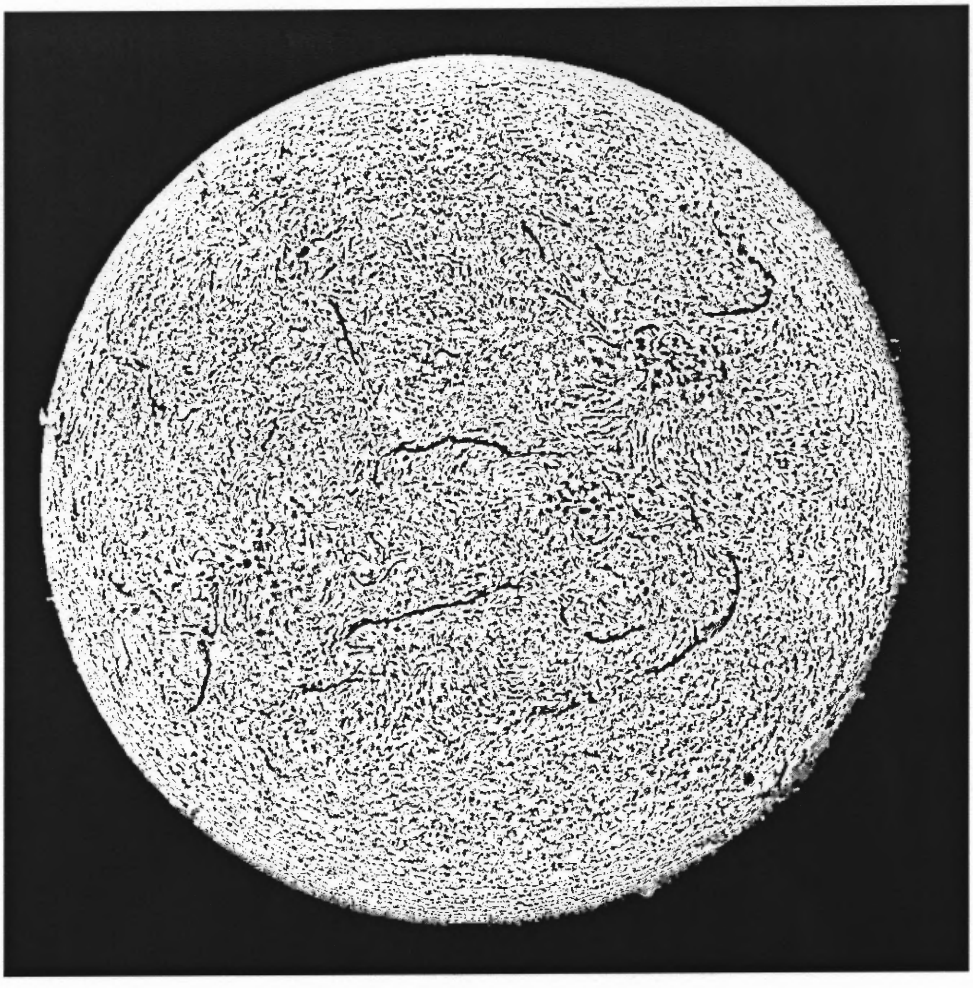

Figure A.17 Solar disk, advanced local thresholding c_{inf}=50, c_{sup}=205, window size w=10.

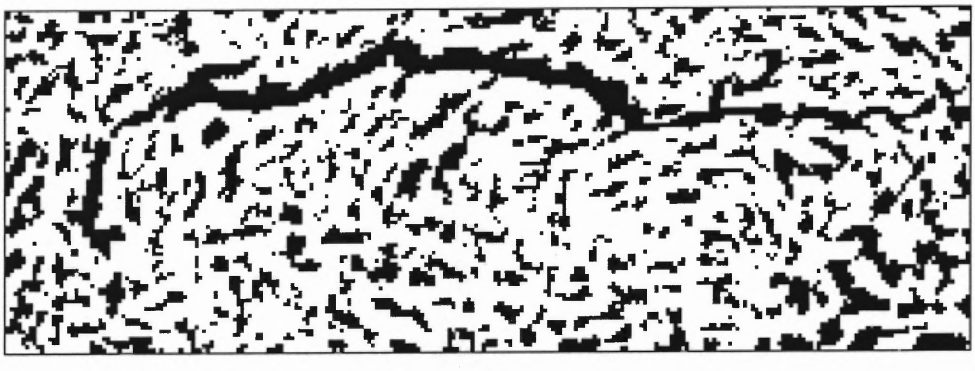

Figure A.18 Filament, advanced local thresholding c_{inf}=50, c_{sup}=205, window size w=10.

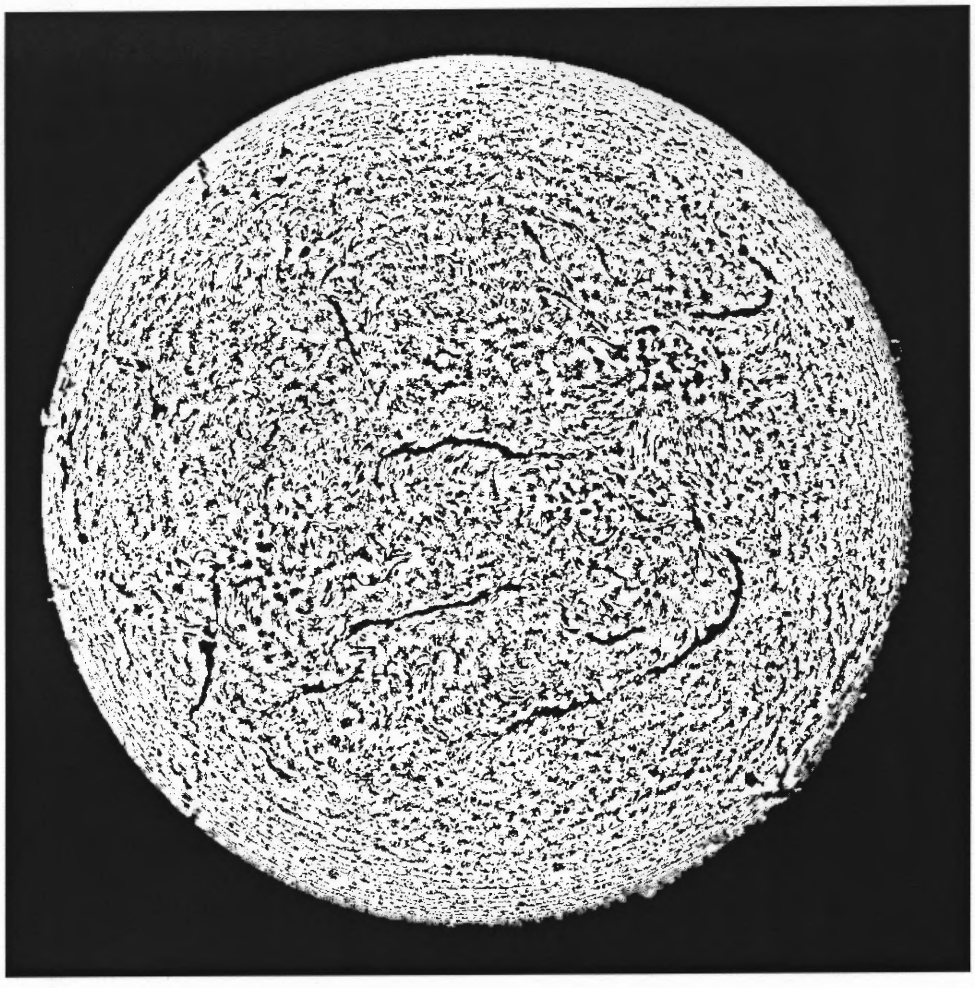

Figure A.19 Solar disk, advanced local thresholding c_{inf}=50, c_{sup}=205, window size w=20.

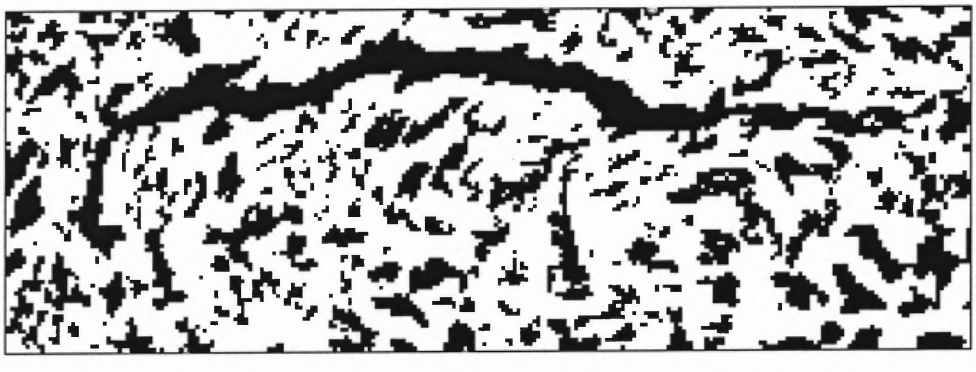

Figure A.20 Filament, advanced local thresholding c_{inf}=50, c_{sup}=205, window size w=20.

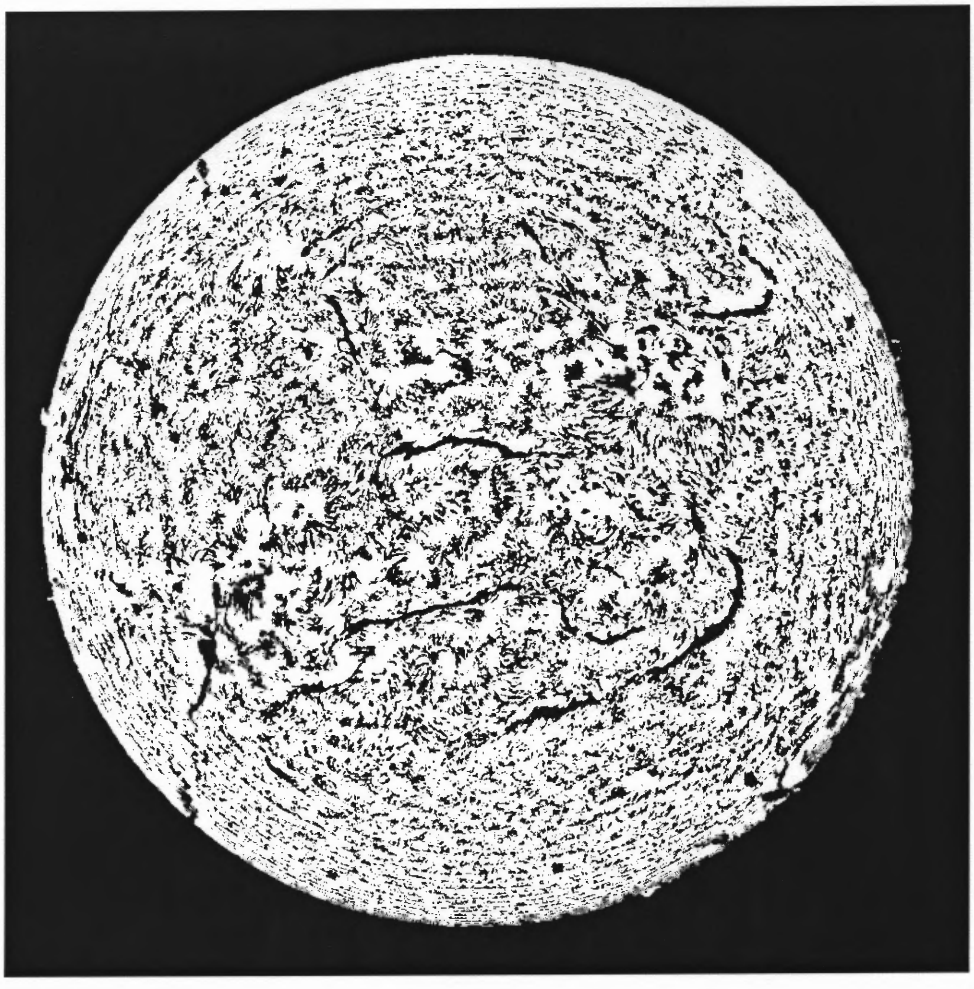

Figure A.21 Solar disk, advanced local thresholding c_{inf}=50, c_{sup}=205, window size w=50.

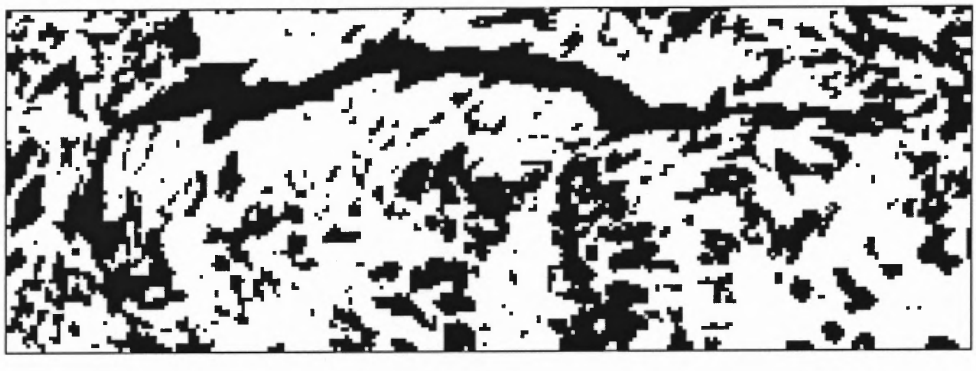

Figure A.22 Filament, advanced local thresholding c_{inf}=50, c_{sup}=205, window size w=50.

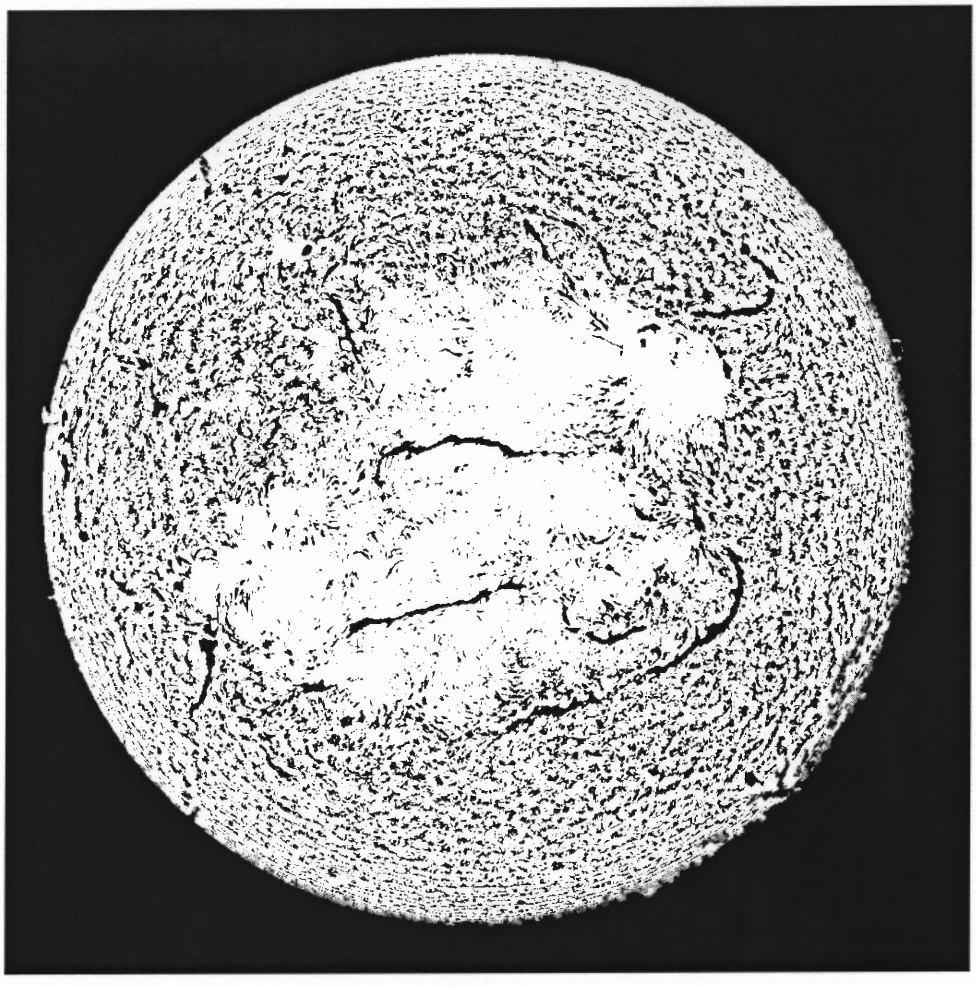

Figure A.23 Solar disk, advanced local thresholding with asymmetrical cutoff values c_{inf}=50, c_{sup}=155, window size w=20.

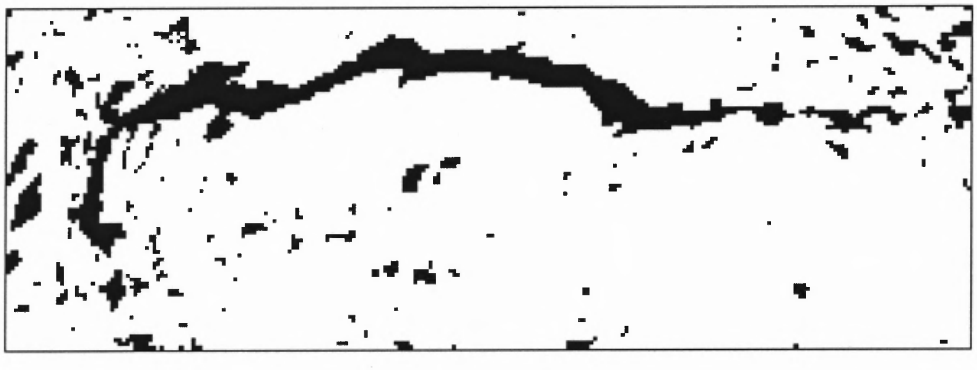

Figure A.24 Filament, advanced local thresholding with asymmetrical cutoff values c_{inf}=50 c_{sup}=155, window size w=20.

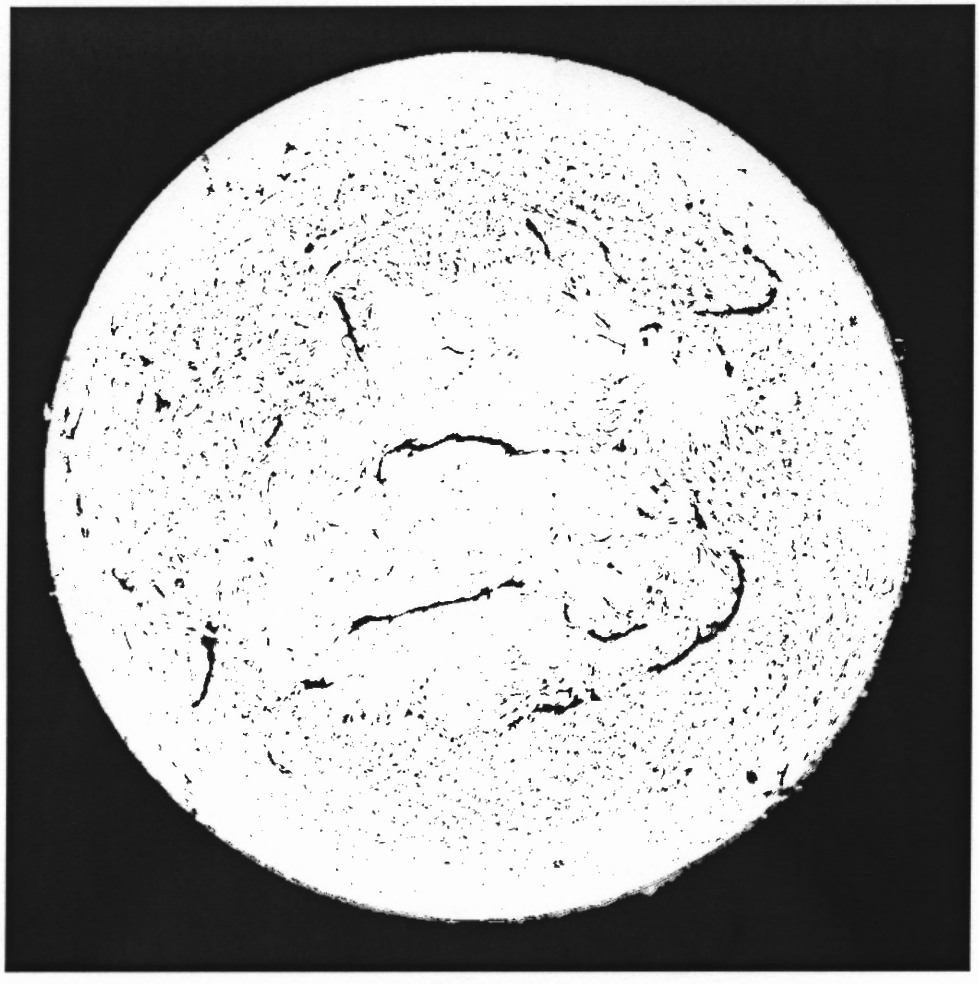

Figure A.25 Solar disk, advanced local thresholding, with asymmetrical cutoff values c_{inf}=50, c_{sup}=155, window size w=20 and modifying factor m=0.95.

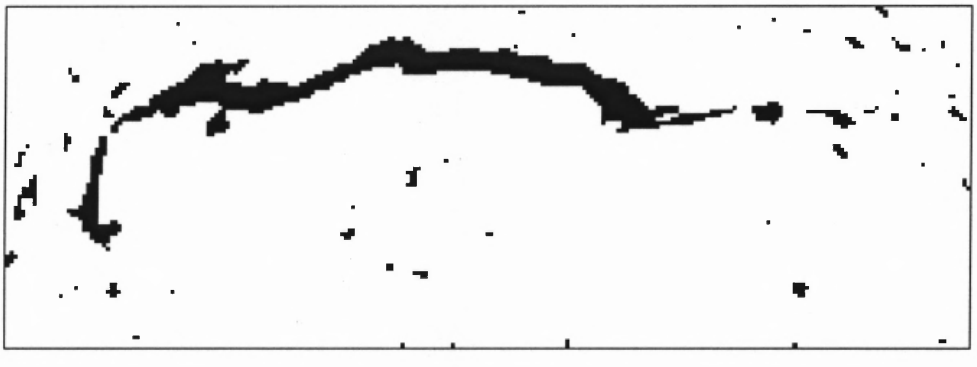

Figure A.26 Filament, advanced local thresholding, with asymmetrical cutoff values c_{inf}=50, c_{sup}=155, window size w=20 and modifying factor m=0.95.

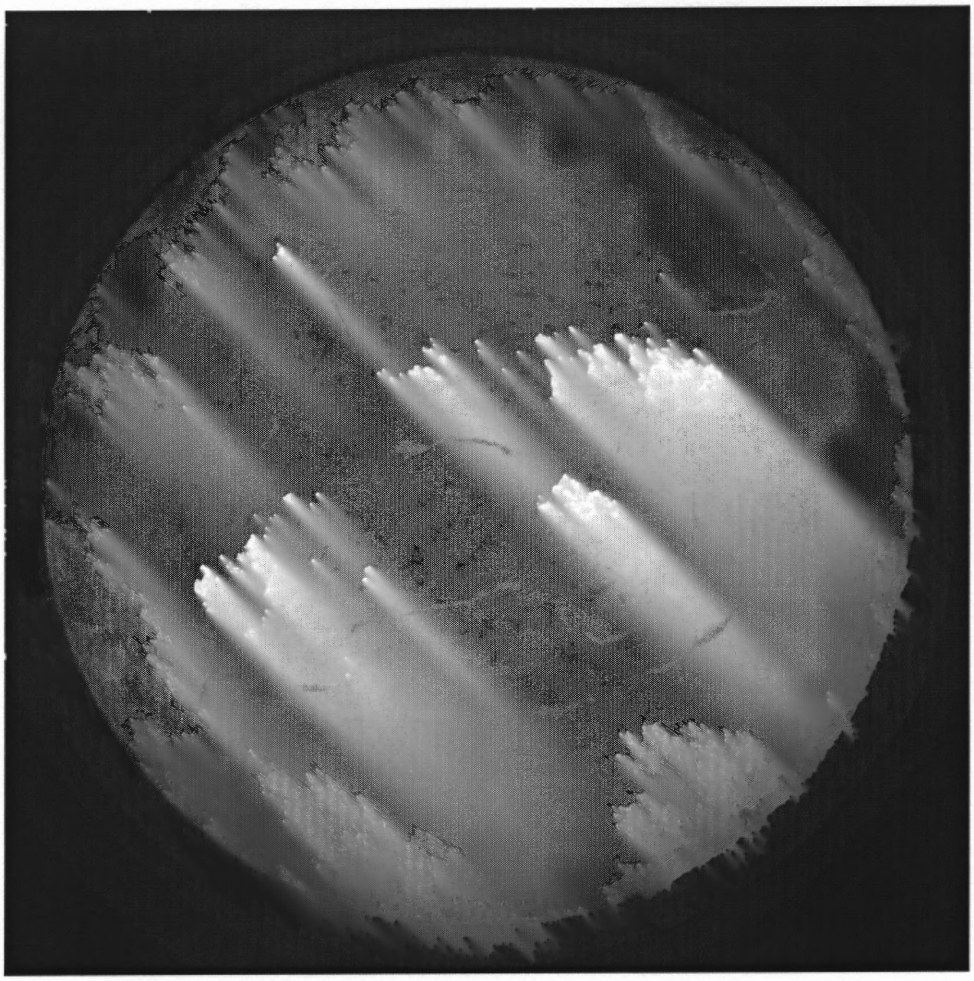

Figure A.27 Solar disk, brightness level normalization.

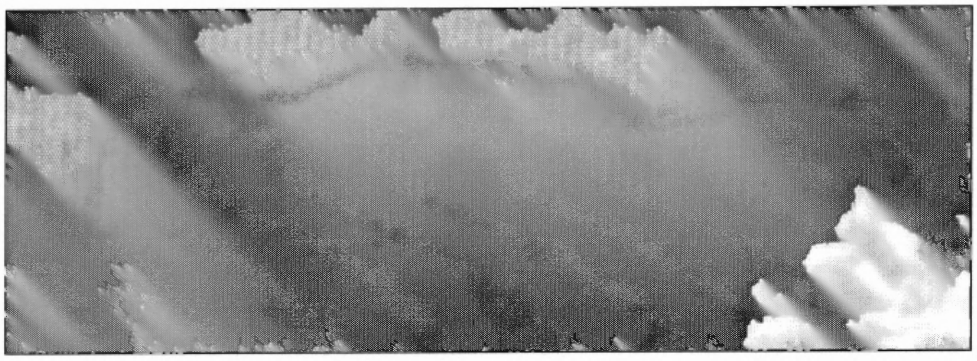

Figure A.28 Filament, brightness level normalization.

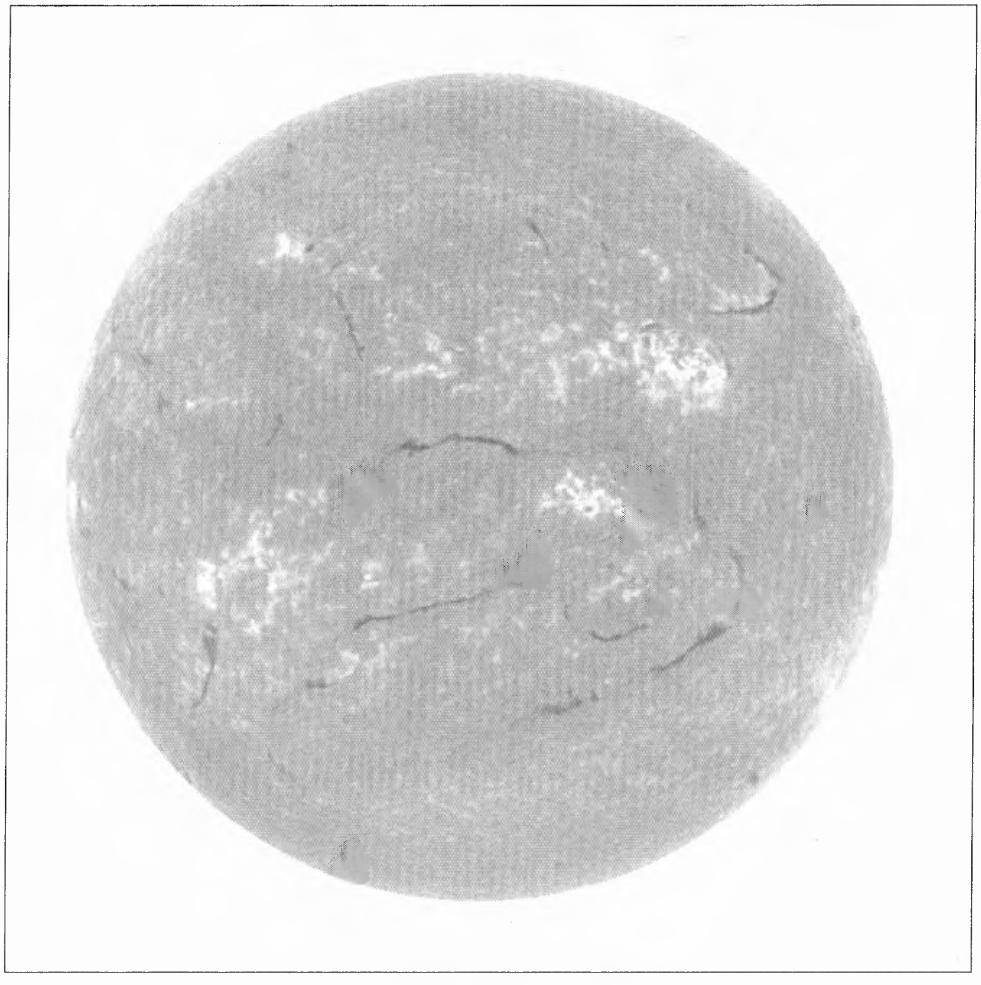

Figure A.29 Solar disk, brightness level normalization, limb darkening removal.

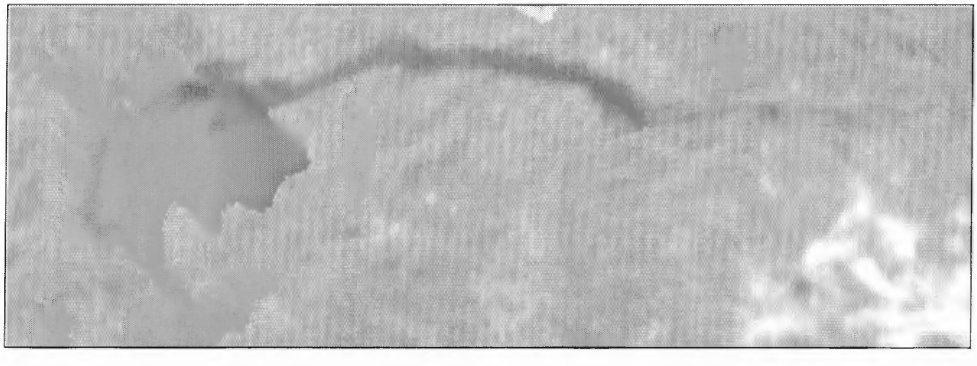

Figure A.30 Filament, brightness level normalization, limb darkening removal.

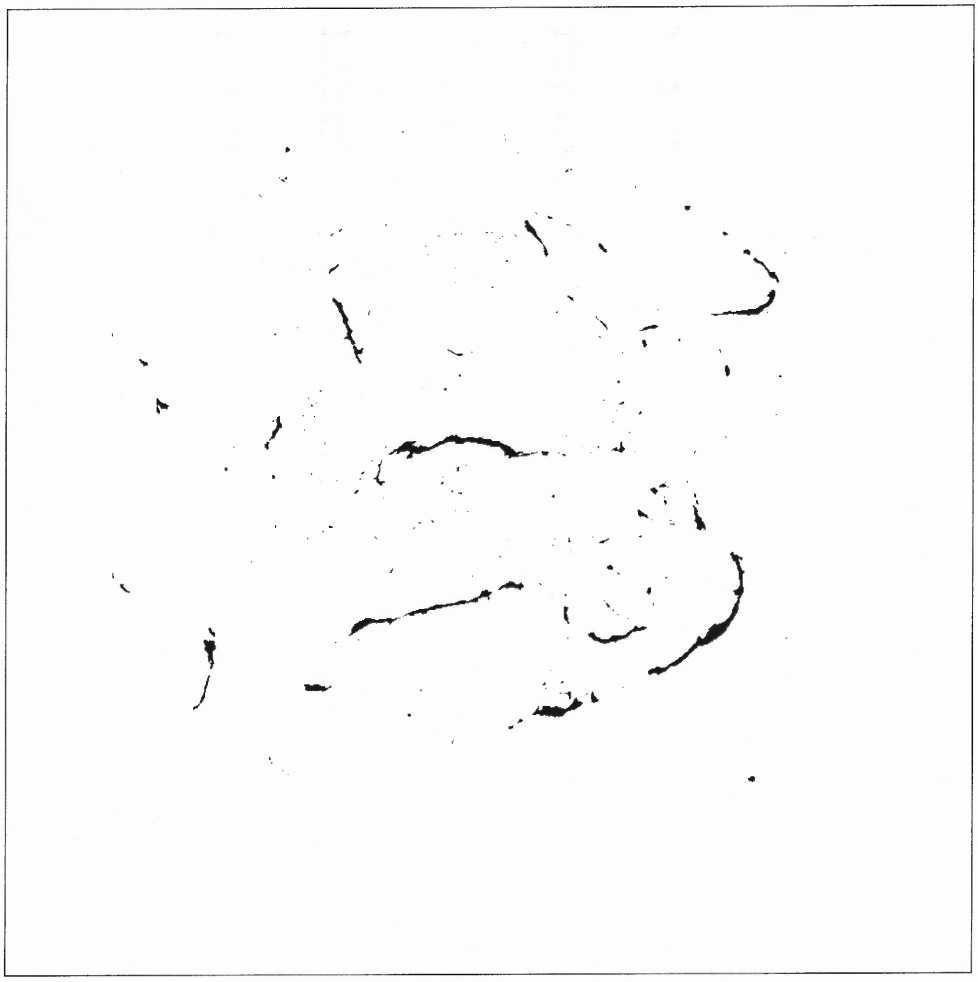

Figure A.31 Solar disk, brightness level normalization, limb darkening and sunspot removal, global thresholding T=185.

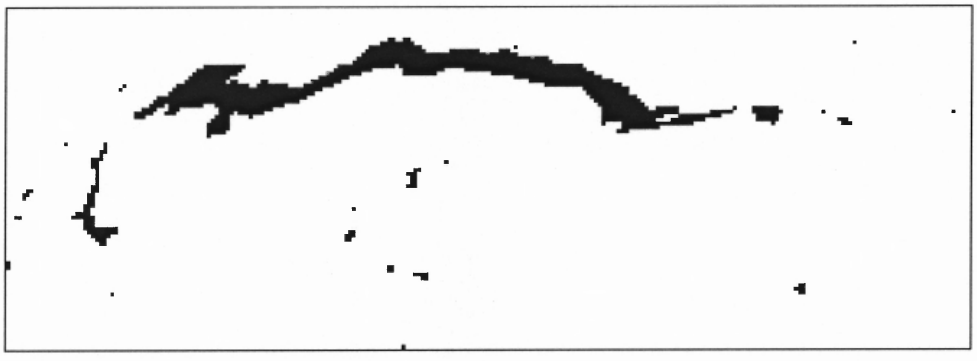

Figure A.32 Filament, brightness level normalization, limb darkening and sunspot removal, global thresholding T=185.

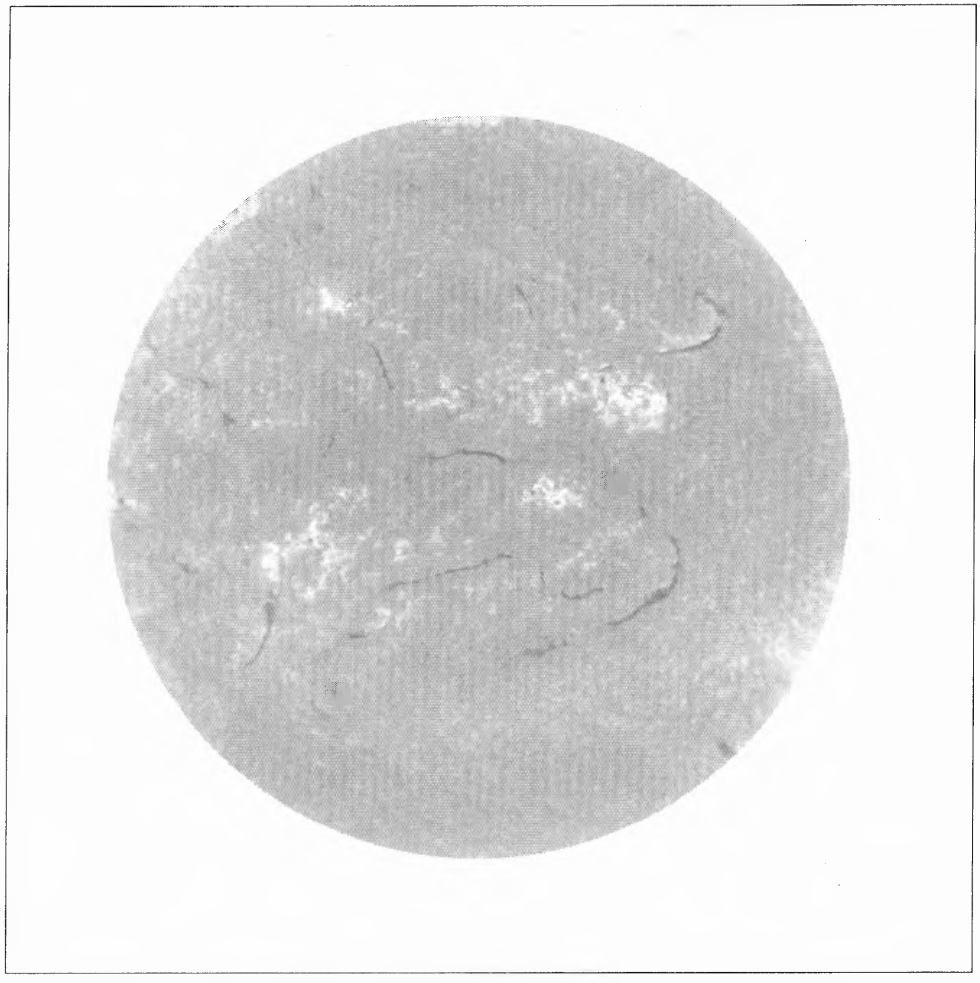

Figure A.33 Solar disk, brightness level normalization, limb darkening and sunspot removal, equal area projection.

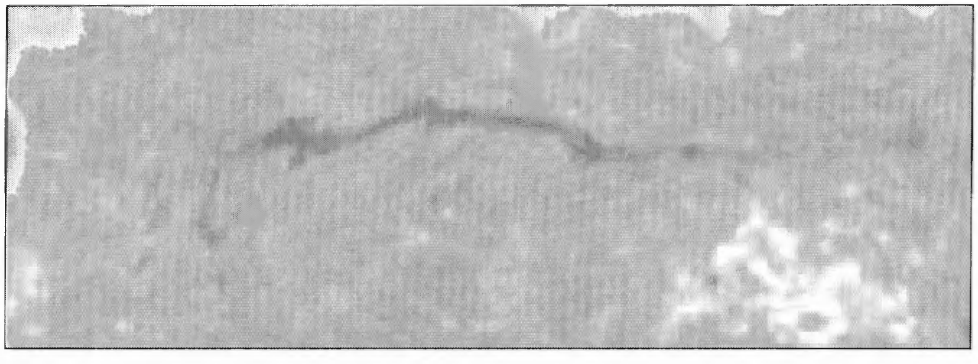

Figure A.34 Filament, brightness level normalization, limb darkening and sunspot removal, equal area projection.

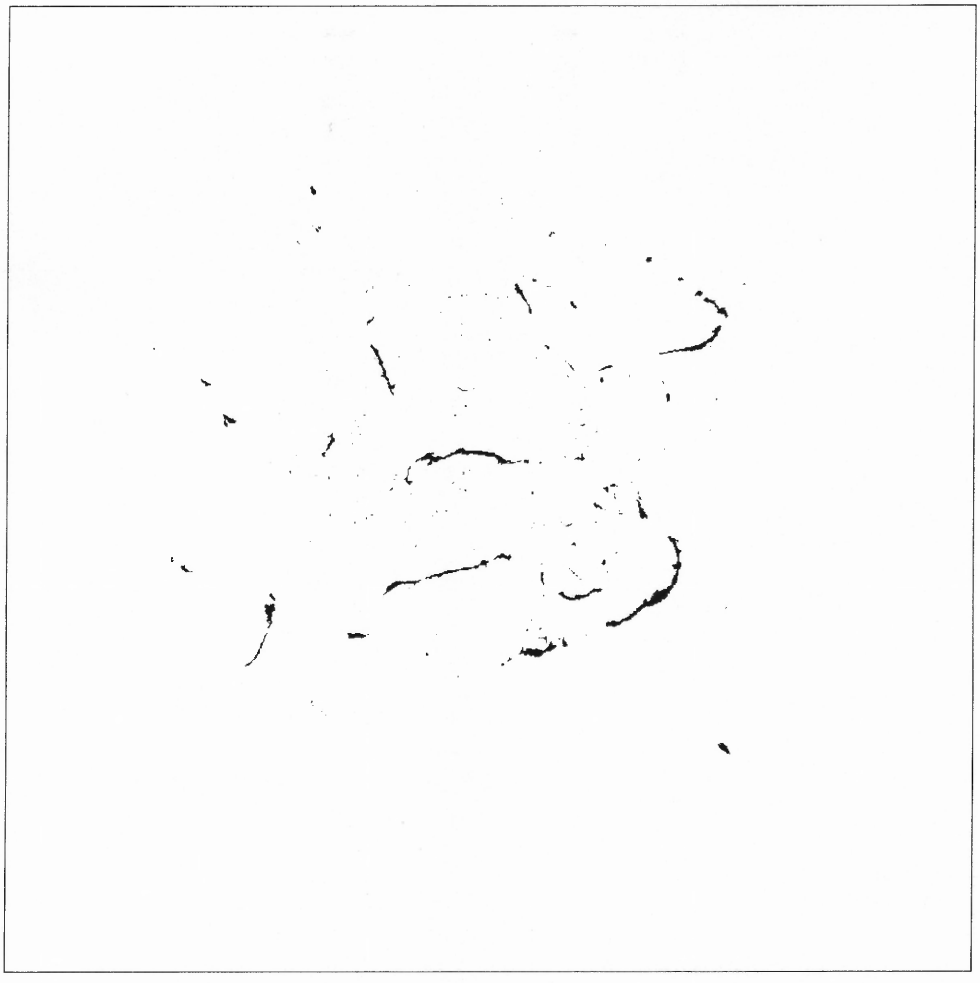

Figure A.35 Solar disk, brightness level normalization, limb darkening and sunspot removal, equal area projection, global thresholding T=185.

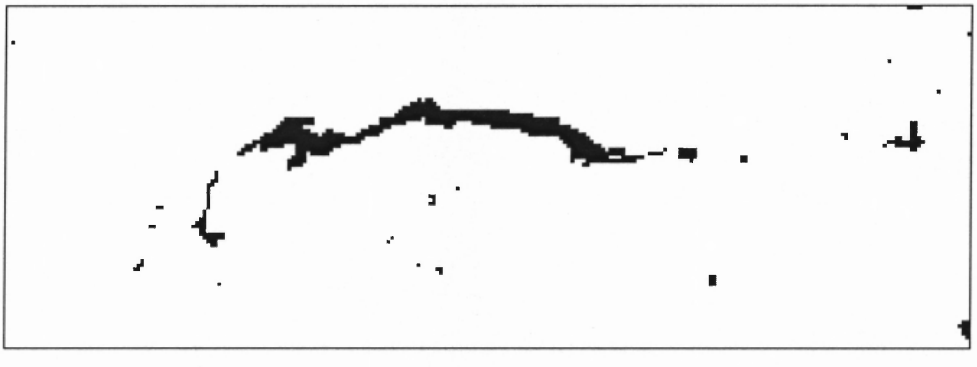

Figure A.36 Filament, brightness level normalization, limb darkening and sunspot removal, equal area projection, global thresholding T=185.

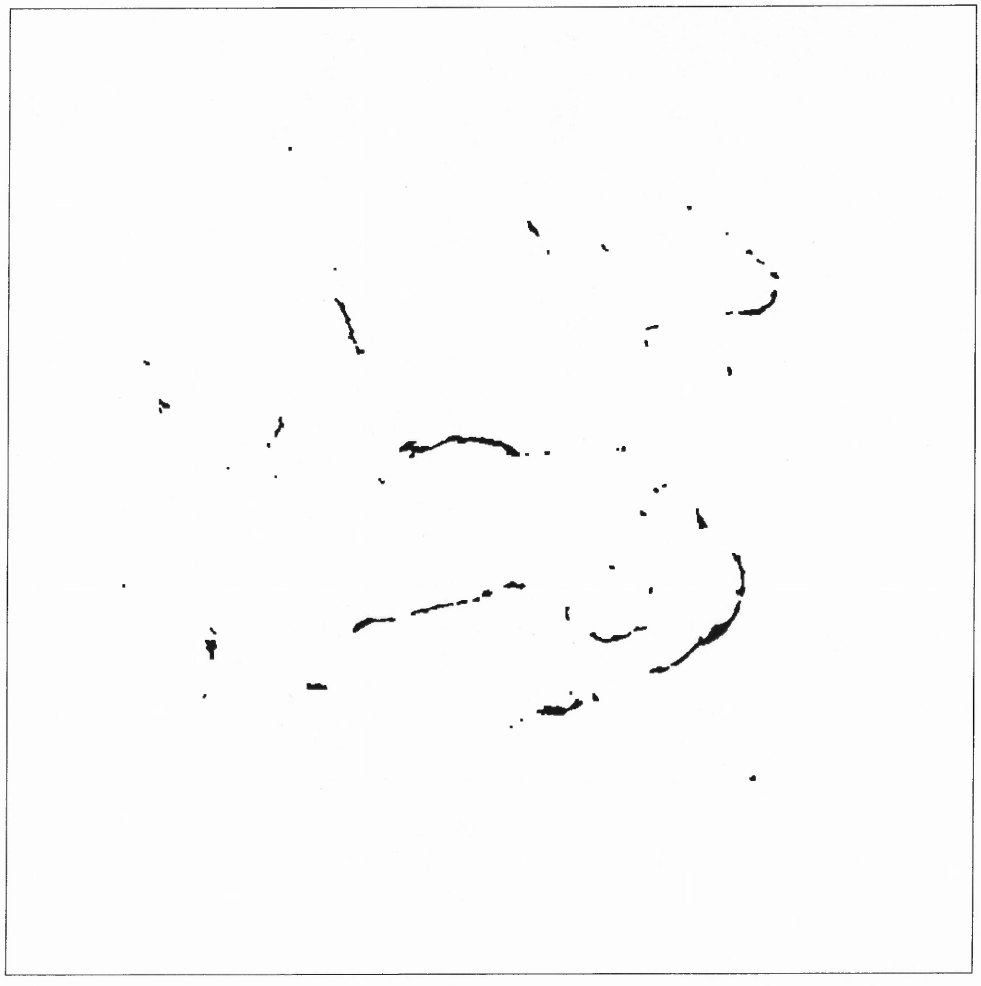

Figure A.37 Solar disk, preprocessed image (brightness level normalization, limb darkening and sunspot removal, global thresholding T=185), 3 × 3 closing.

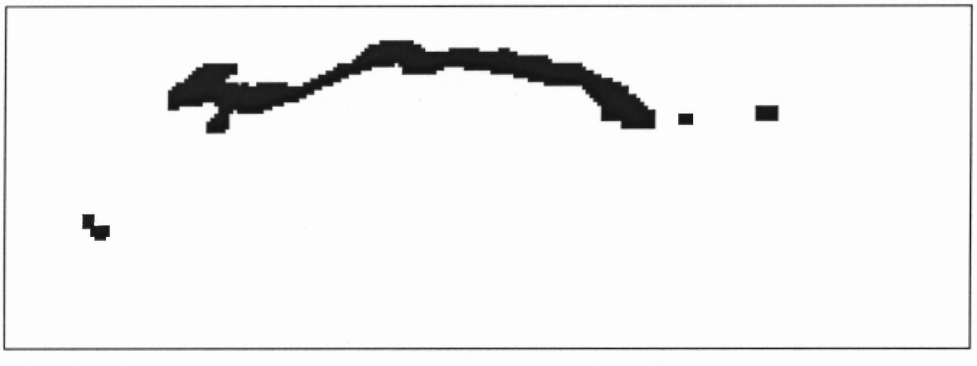

Figure A.38 Filament, preprocessed image (brightness level normalization, limb darkening and sunspot removal, global thresholding T=185), 3 × 3 closing.

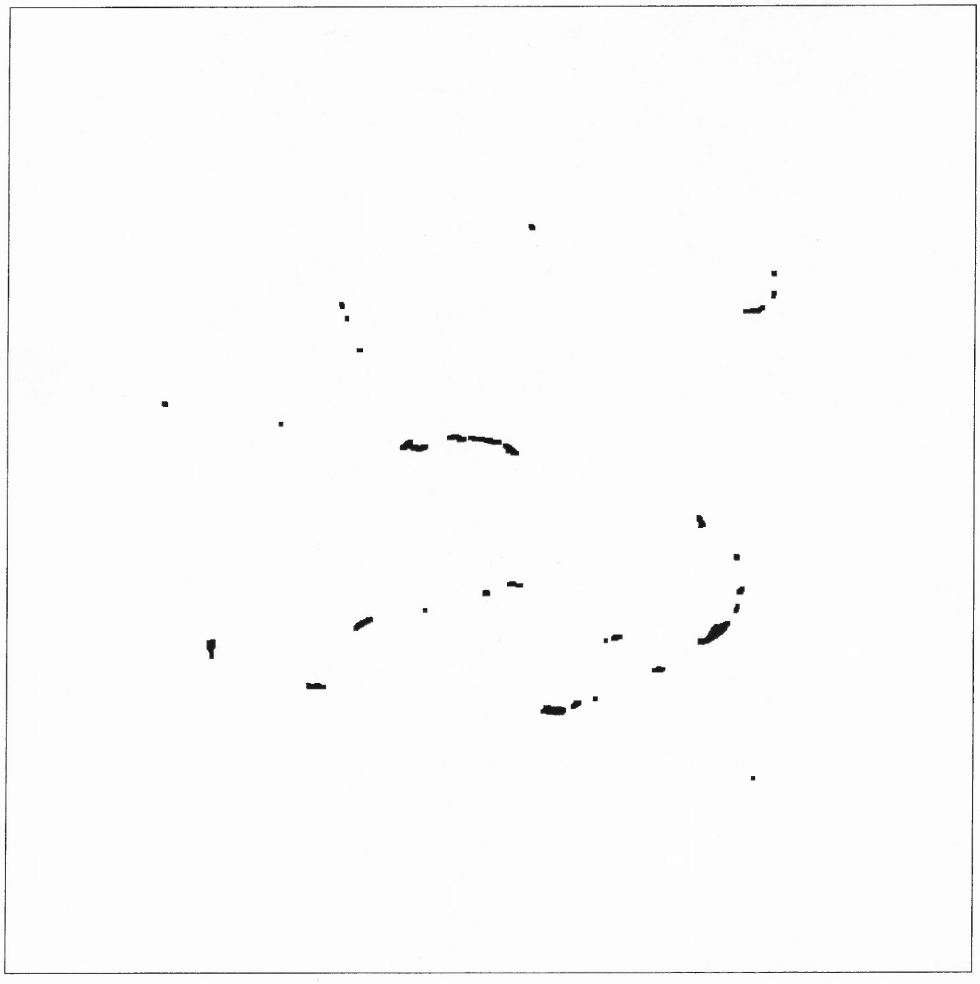

Figure A.39 Solar disk, preprocessed image, 5 × 5 closing.

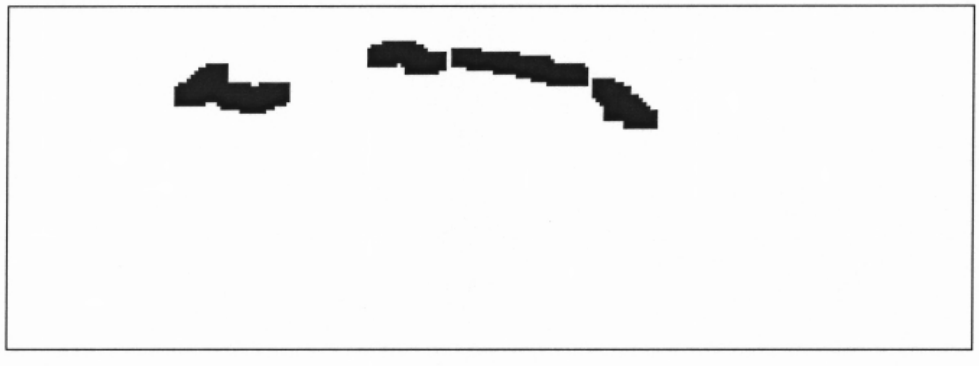

Figure A.40 Filament, preprocessed image, 5 × 5 closing.

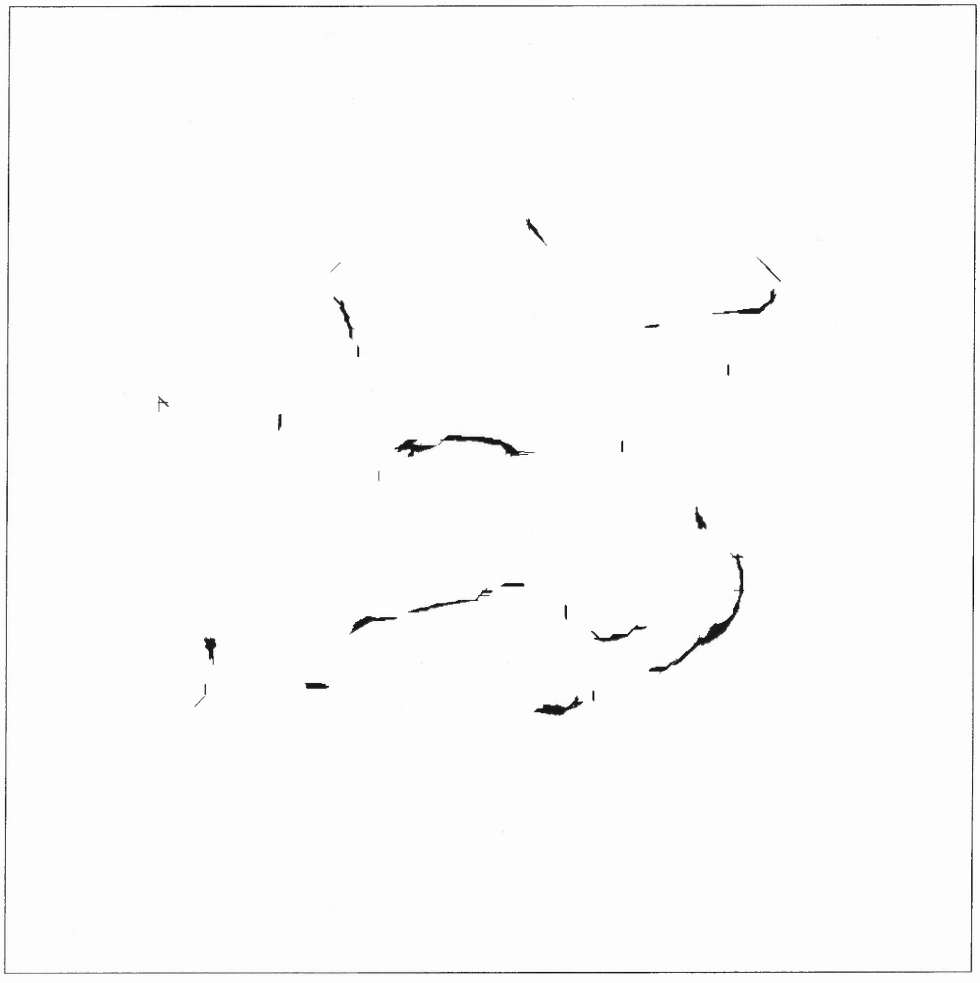

Figure A.41 Solar disk, preprocessed image, superposition of four traditional directional closing operations.

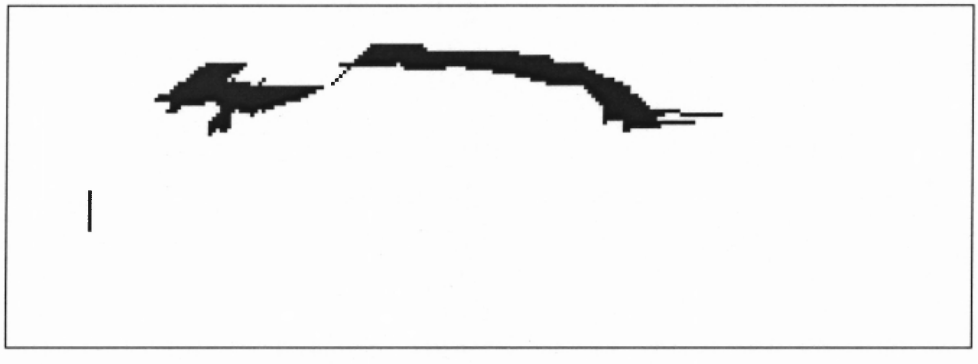

Figure A.42 Filament, preprocessed image, superposition of four traditional directional closing operations.

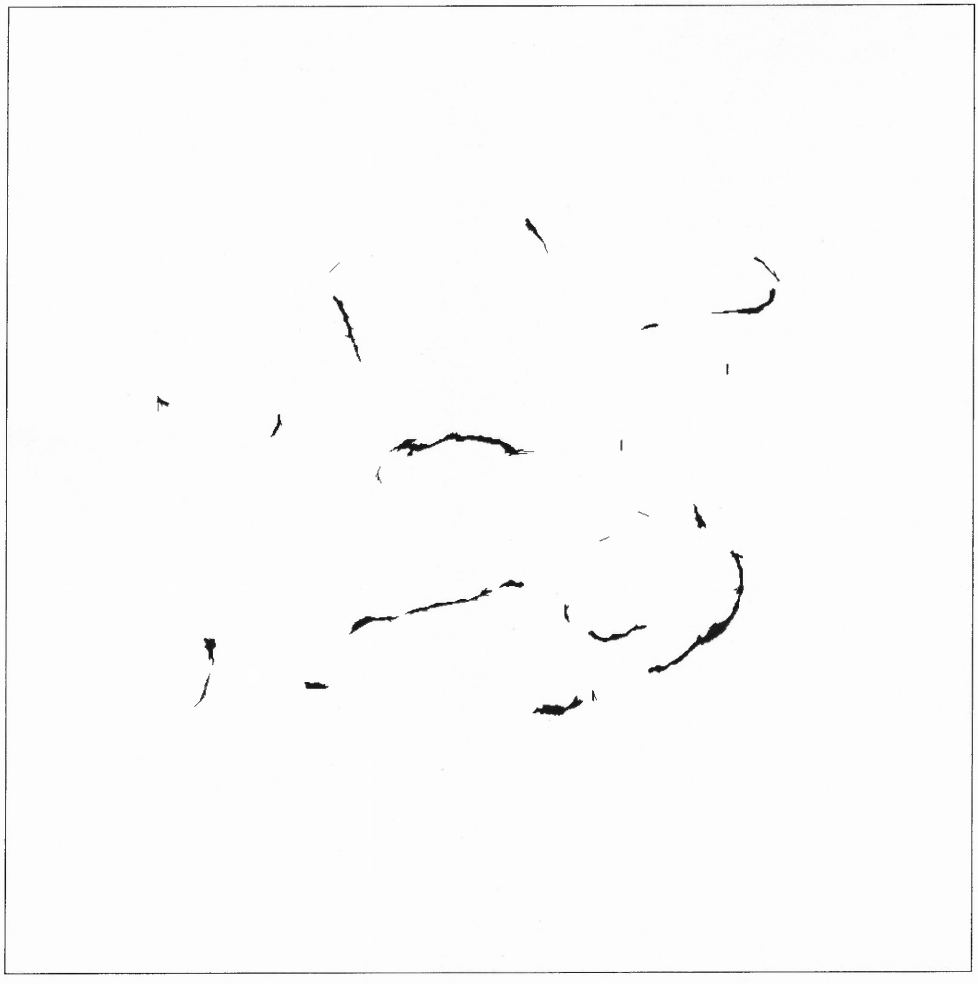

Figure A.43 Solar disk, preprocessed image, superposition of eight traditional directional closing operations.

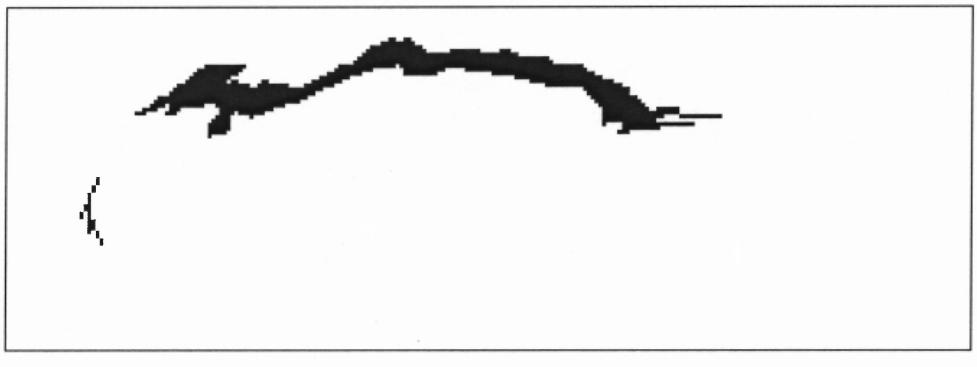

Figure A.44 Filament, preprocessed image, superposition of eight traditional directional closing operations.

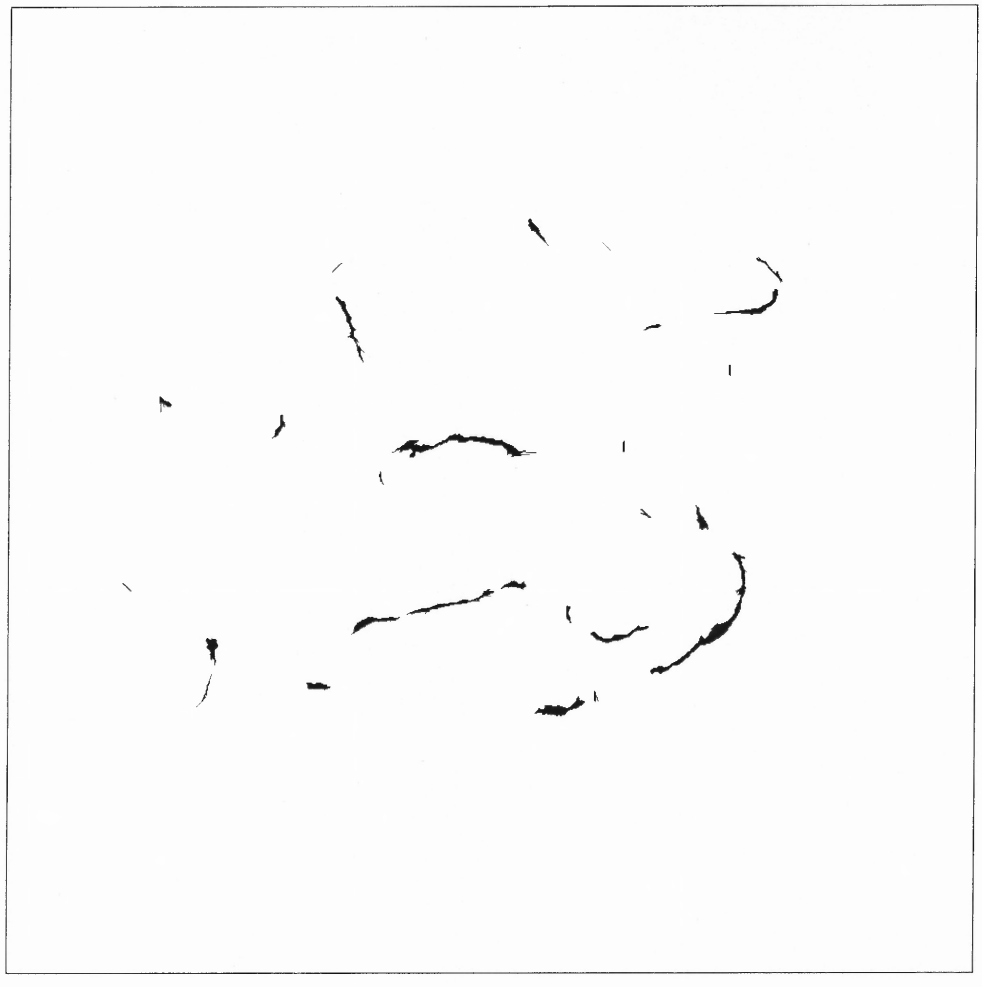

Figure A.45 Solar disk, preprocessed image, superposition of eight recursive directional closing operations.

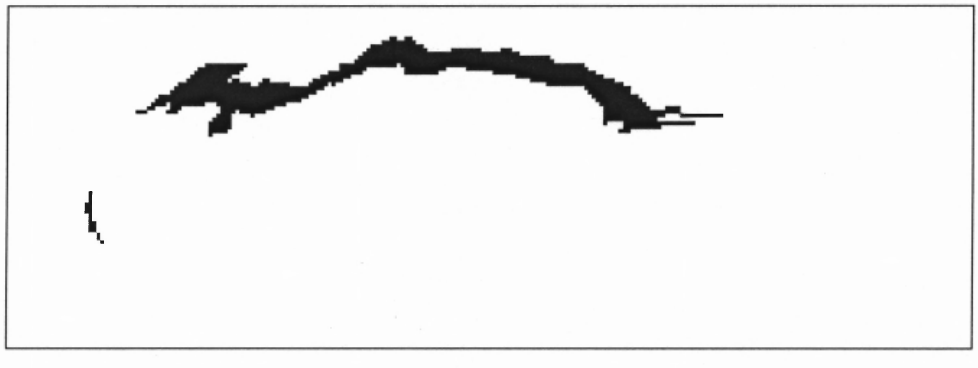

Figure A.46 Filament, preprocessed image, superposition of eight recursive directional closing operations.

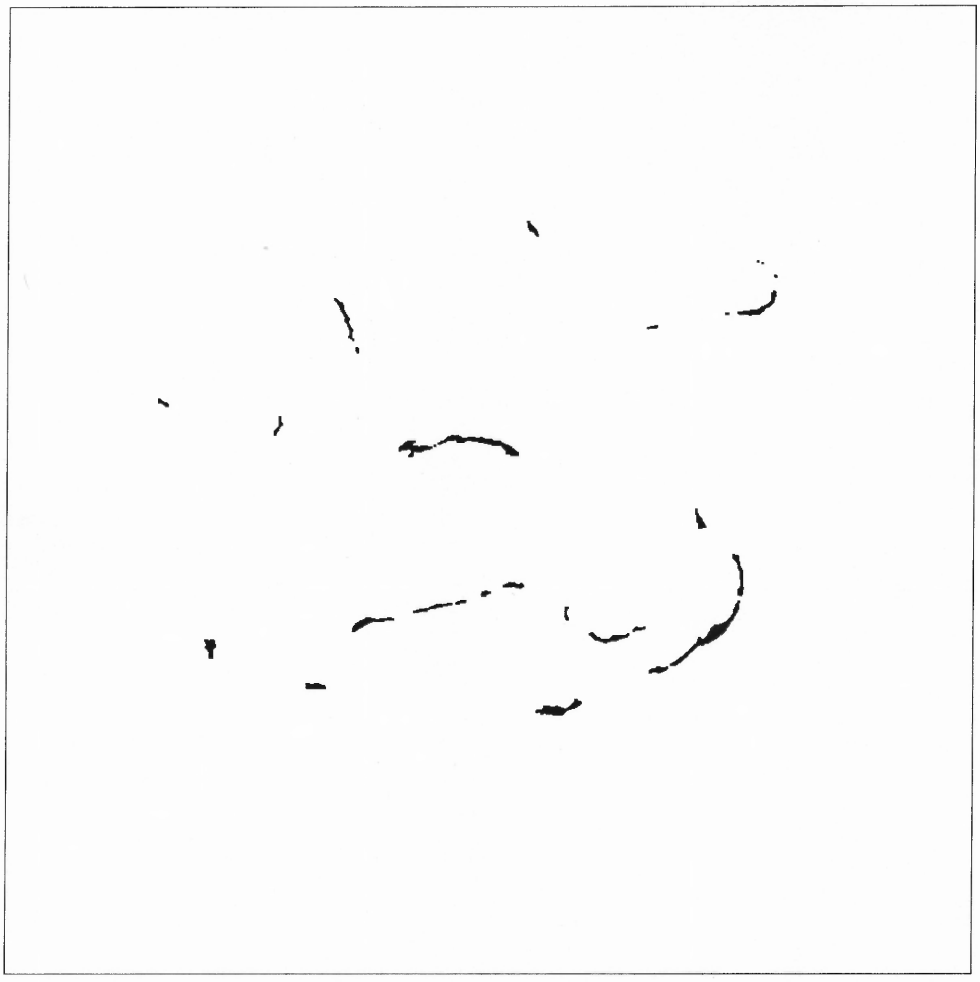

Figure A.47 Solar disk, preprocessed image, superposition of eight recursive directional closing operations, 3 × 3 "cleaning" closing.

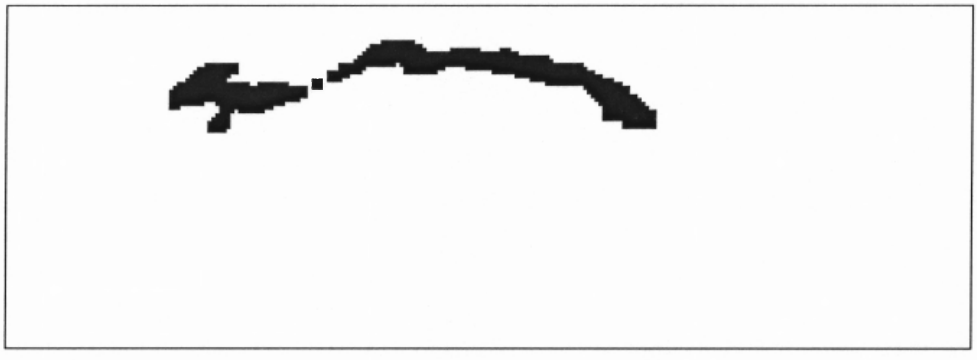

Figure A.48 Filament, preprocessed image, superposition of eight recursive directional closing operations, 3 × 3 "cleaning" closing.

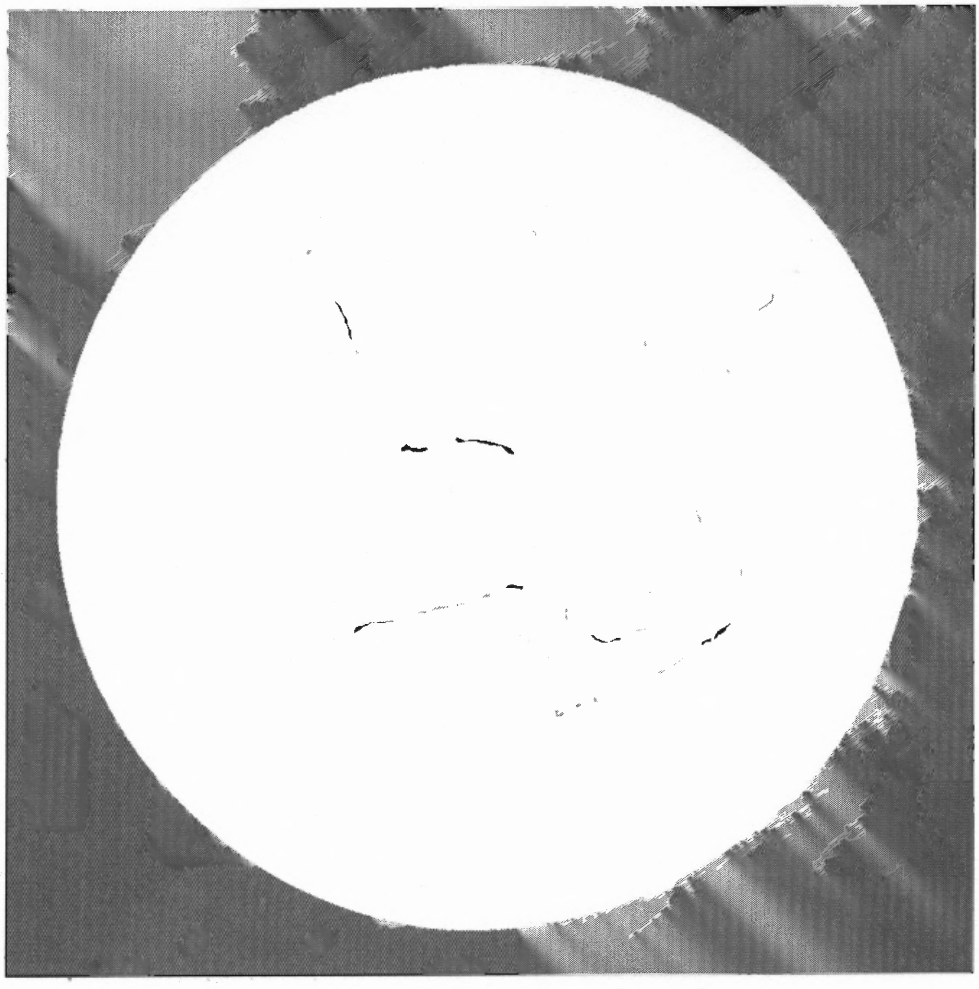

Figure A.49 Solar disk, the result of applying Method I.

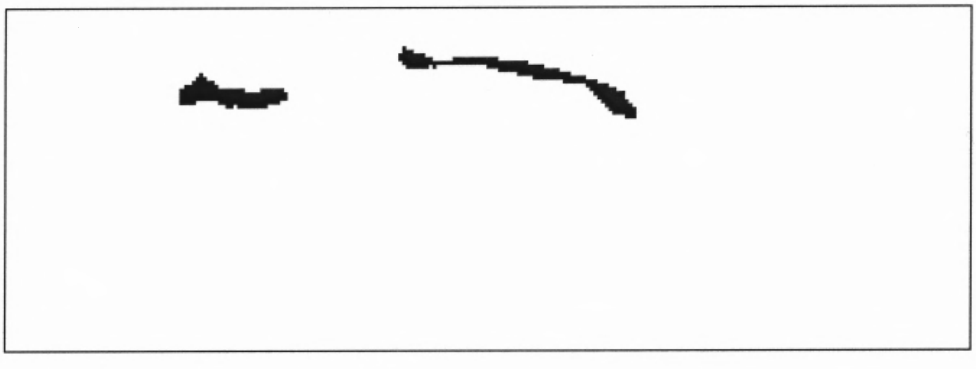

Figure A.50 Filament, the result of applying Method I.

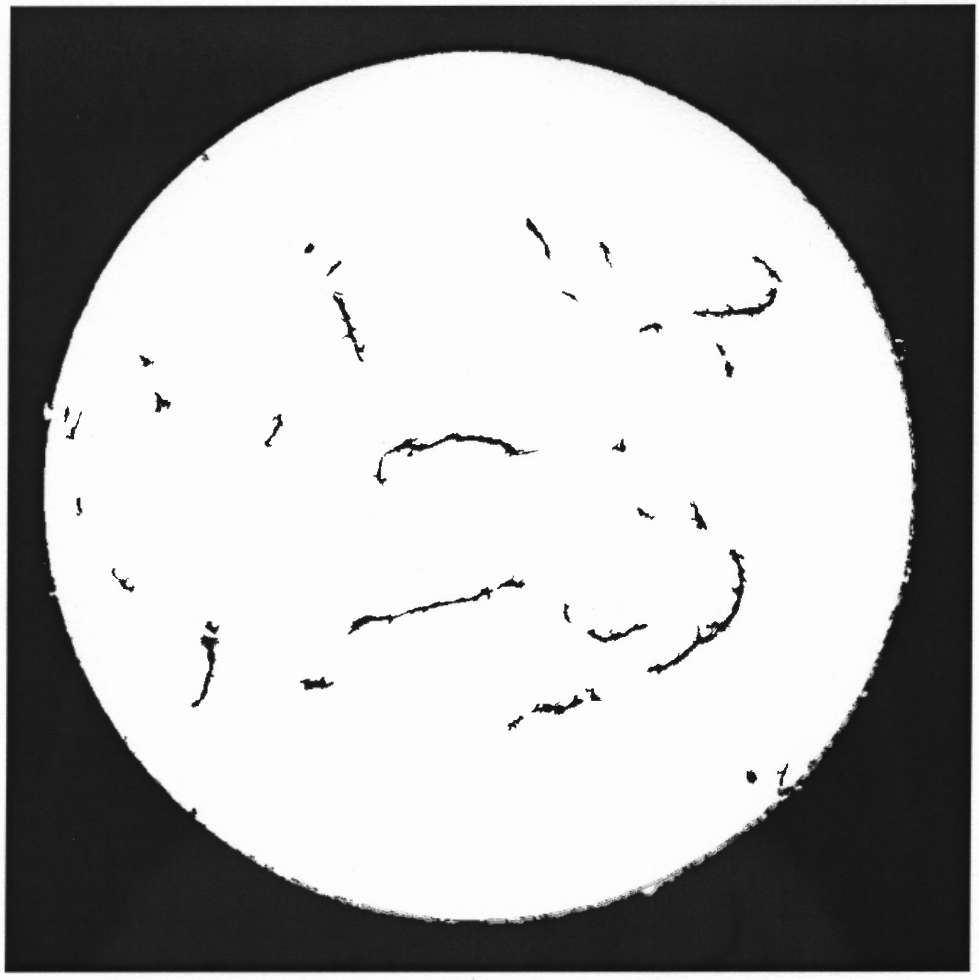

Figure A.51 Solar disk, the result of applying Method II.

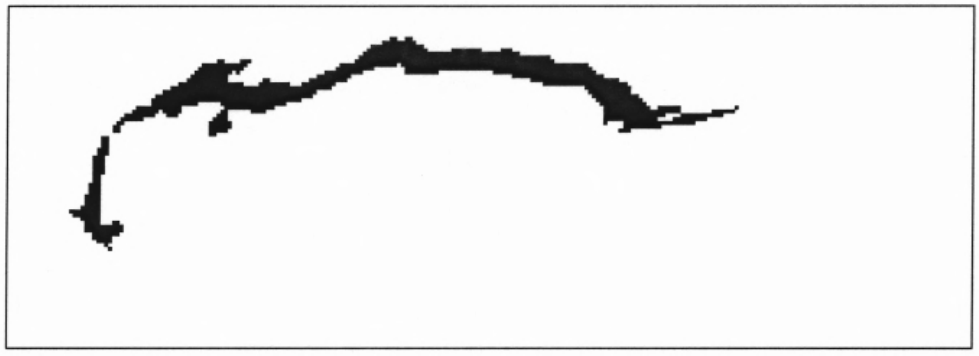

Figure A.52 Filament, the result of applying Method II.

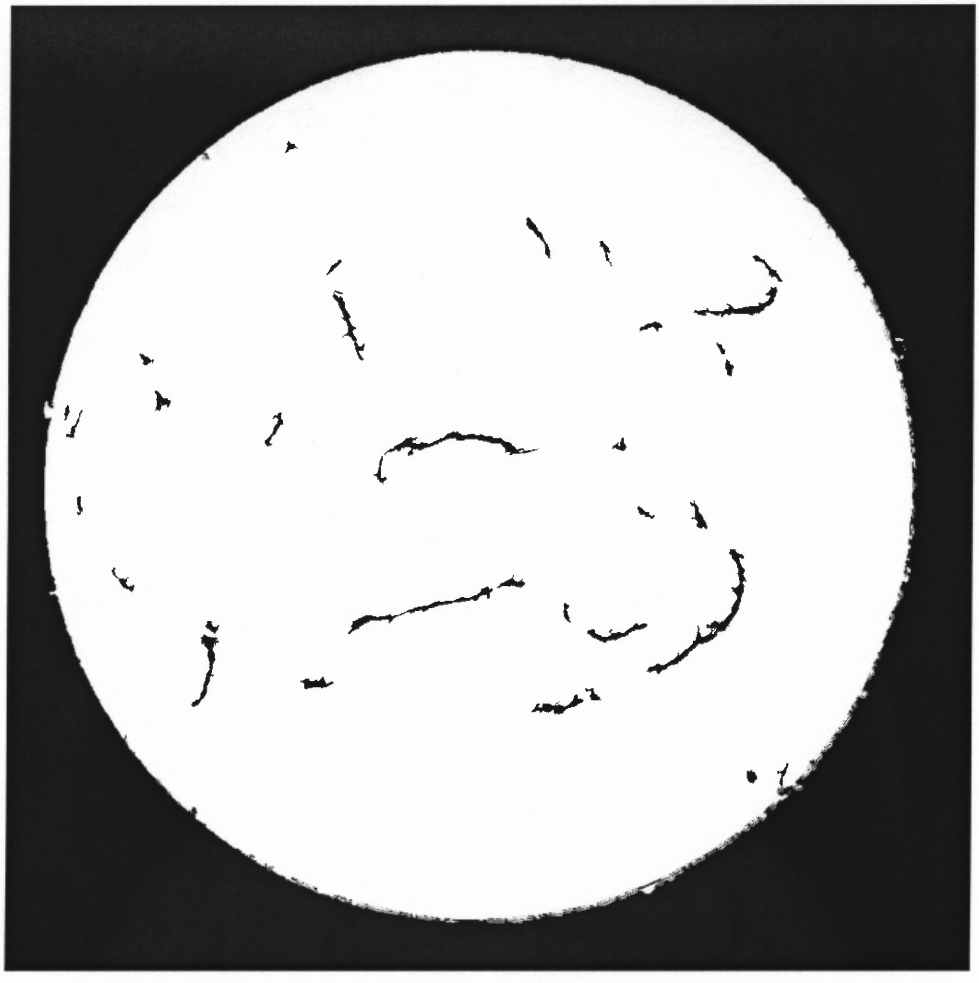

Figure A.53 Solar disk, the result of applying Method III.

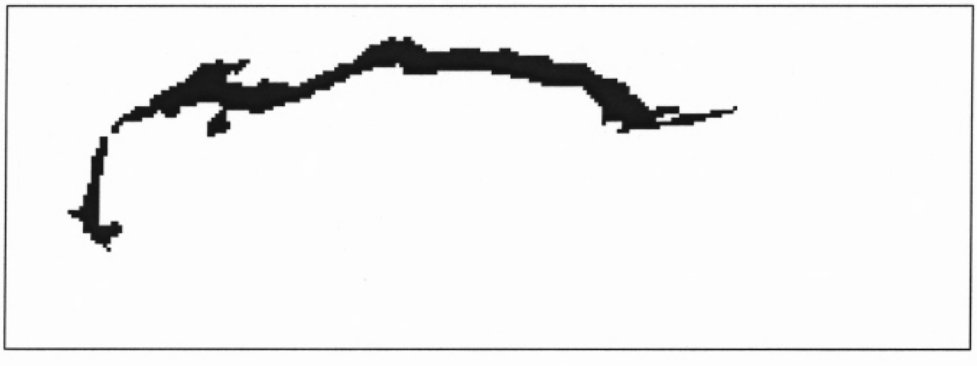

Figure A.54 Filament, the result of applying Method III.

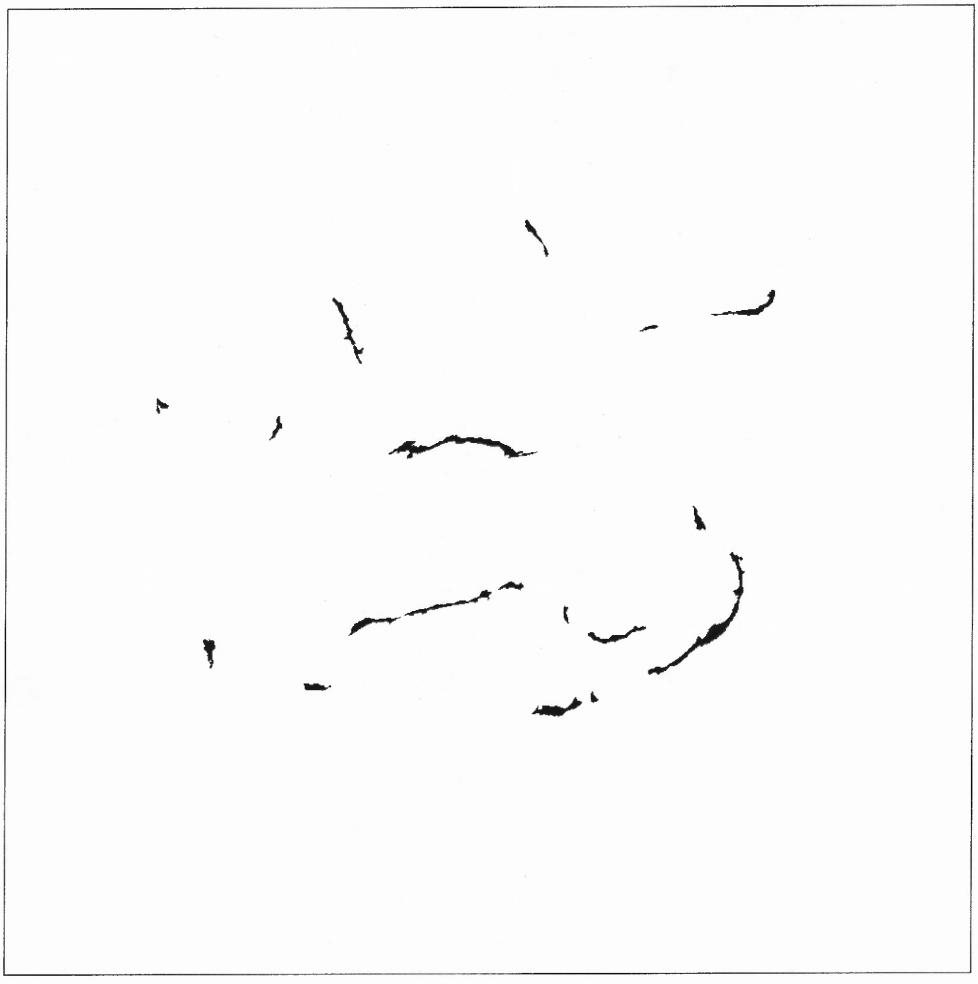

Figure A.55 Solar disk, the result of applying Method IV.

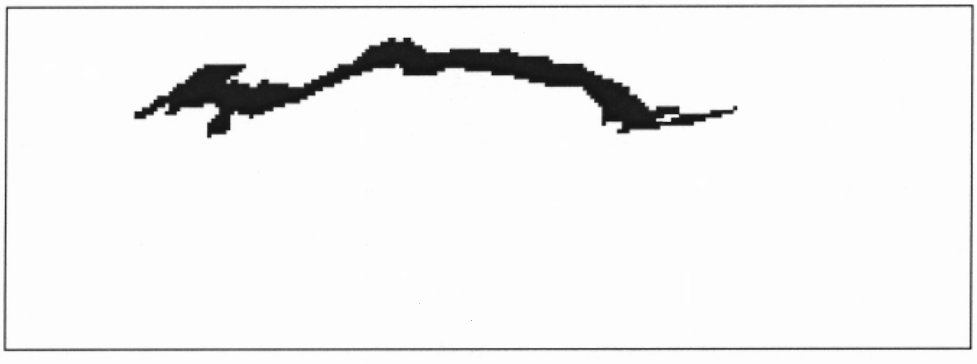

Figure A.56 Filament, the result of applying Method IV.

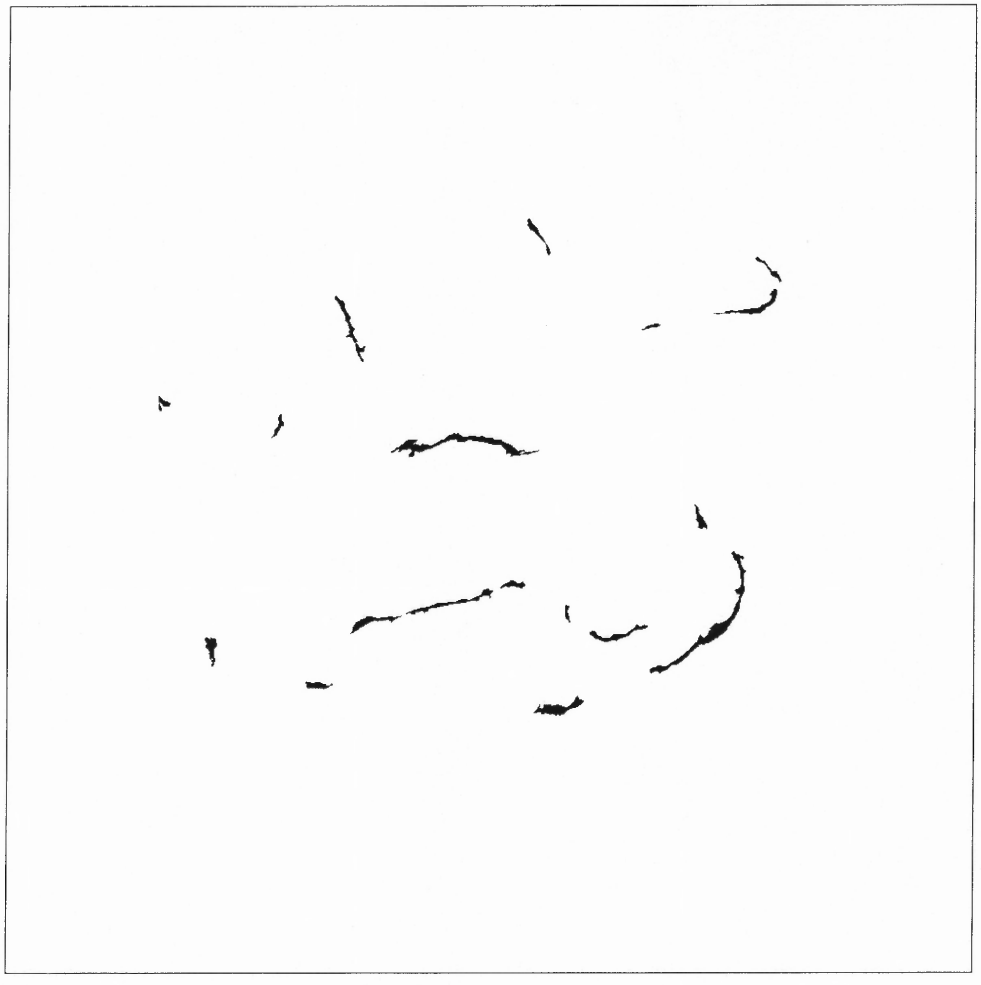

Figure A.57 Solar disk, the result of applying Method V.

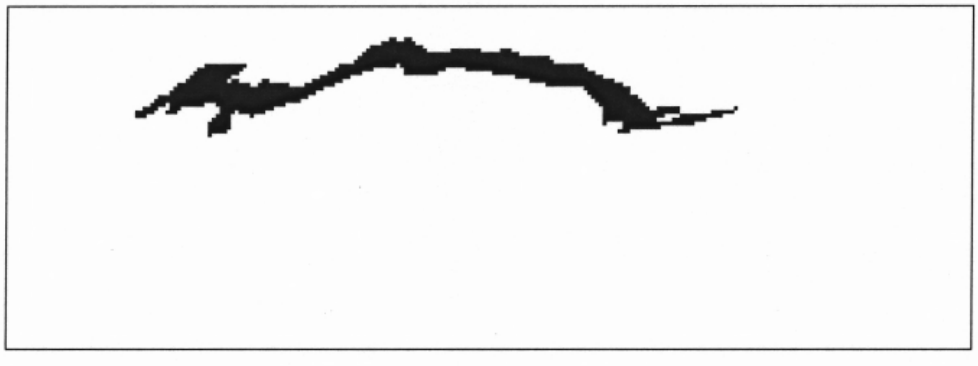

Figure A.58 Filament, the result of applying Method V.

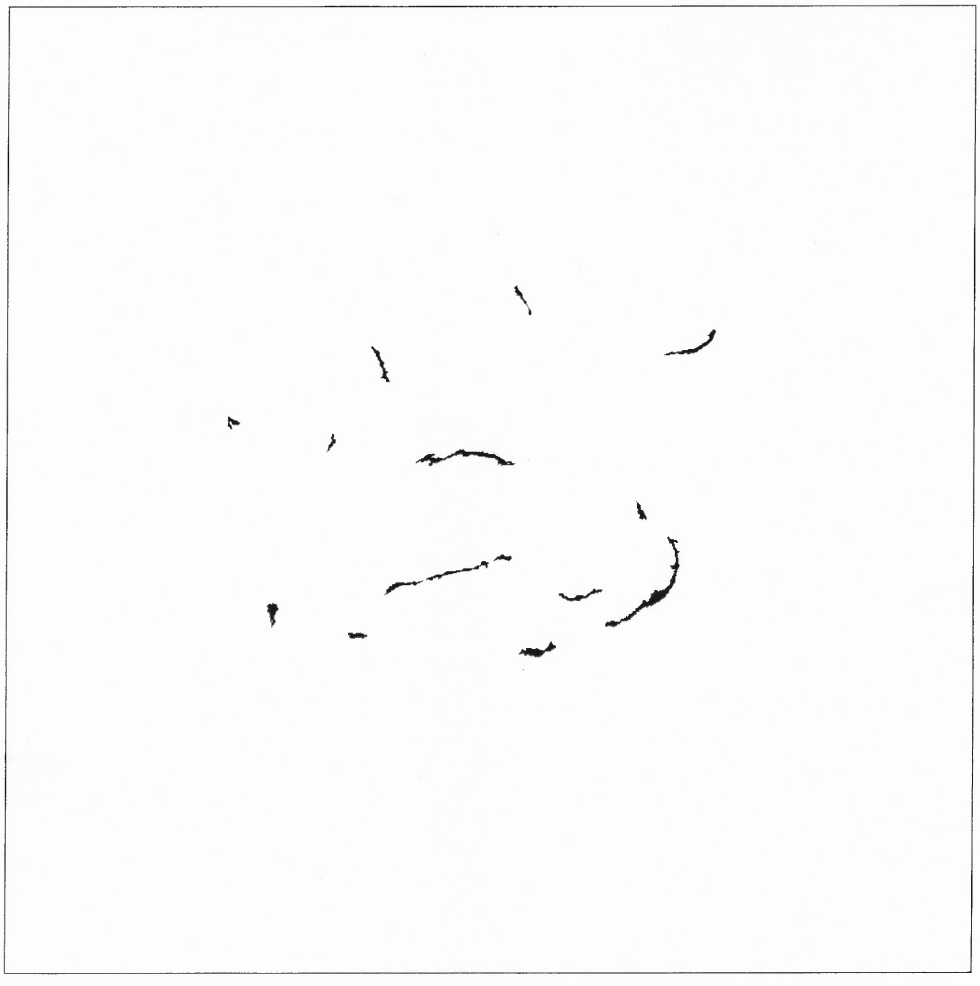

Figure A.59 Solar disk, the result of applying Method VI.

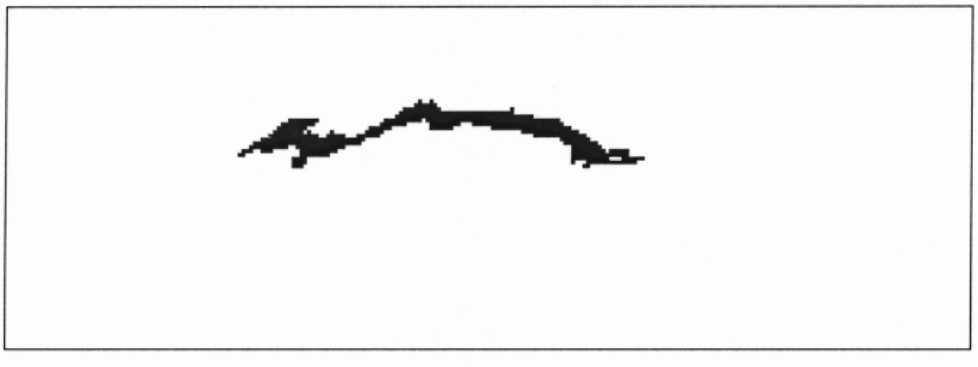

Figure A.60 Filament, the result of applying Method VI.

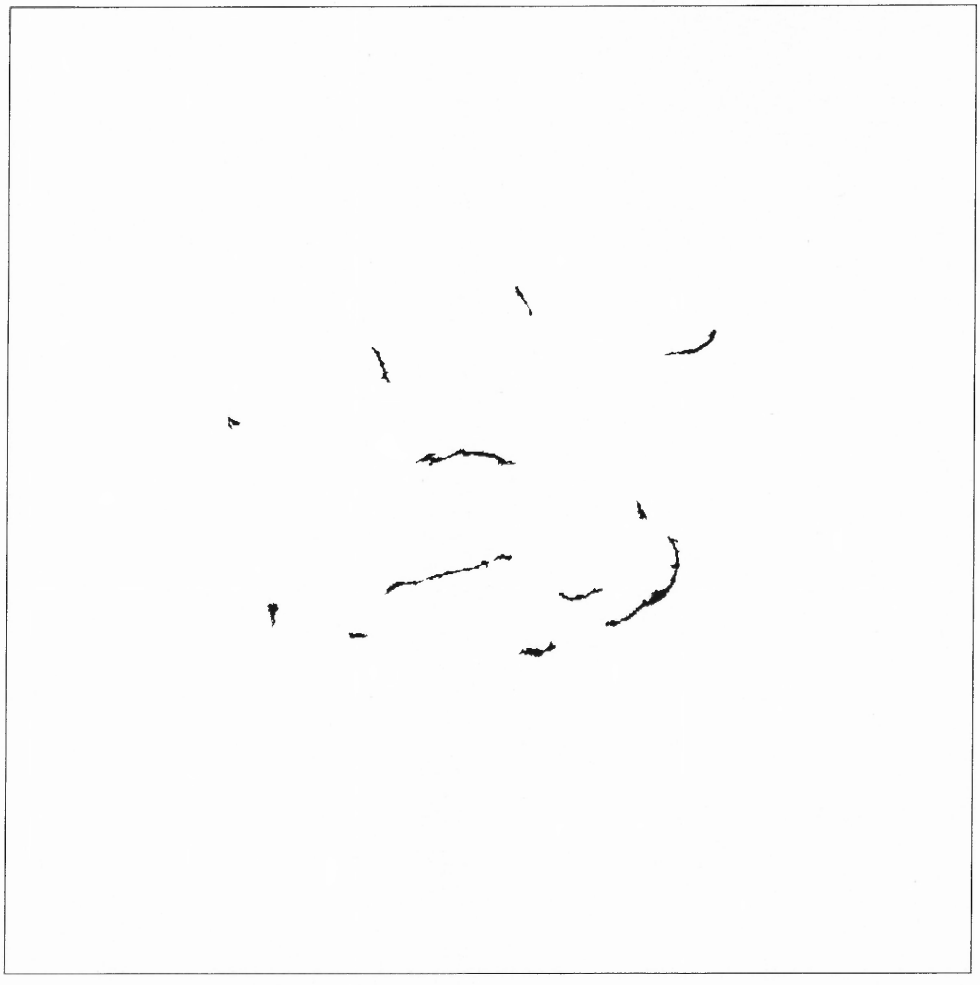

Figure A.61 Solar disk, the result of applying Method VII.

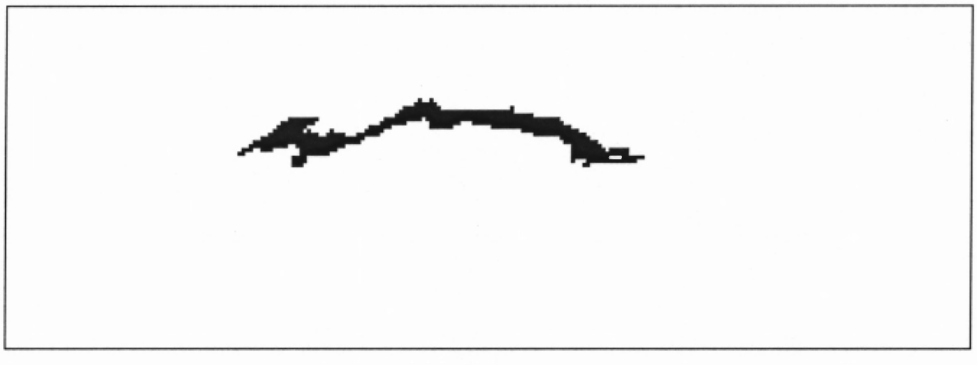

Figure A.62 Filament, the result of applying Method VII.

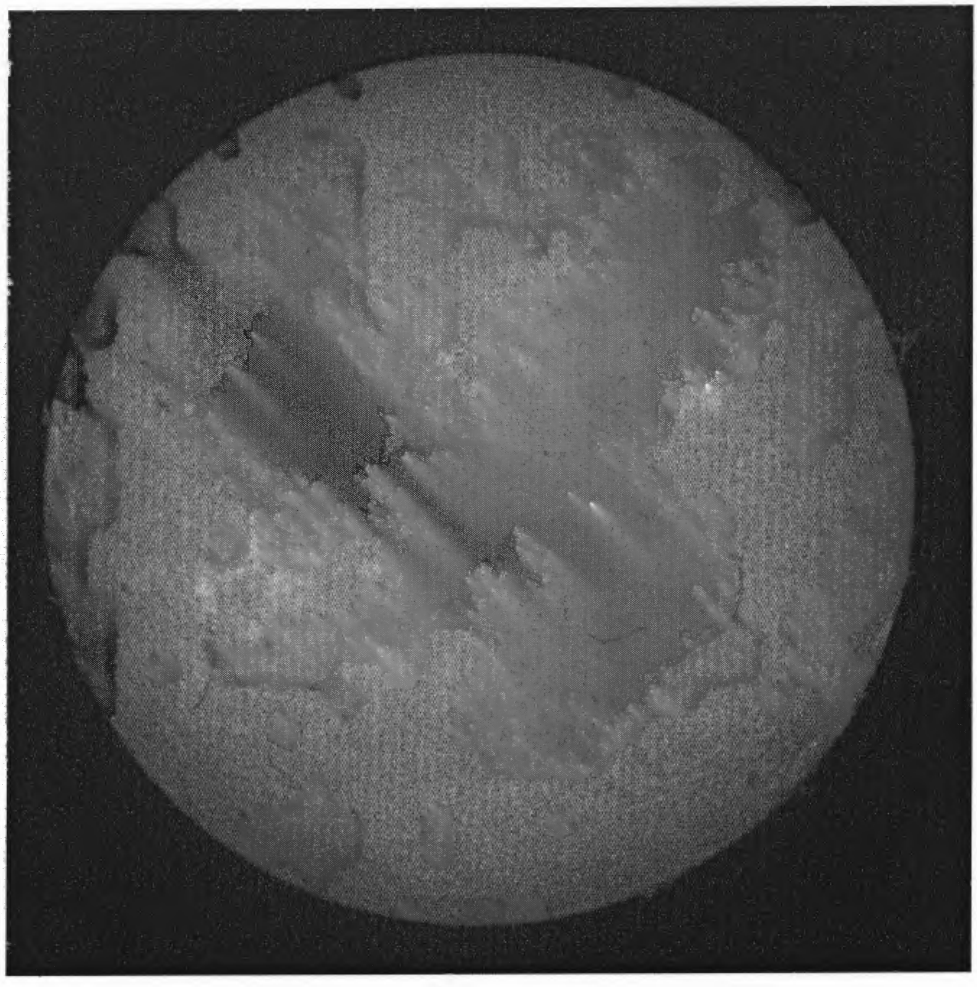

Figure A.63 Solar disk, original image with Gaussian noise, 50% of the noise level and 50% noise distribution.

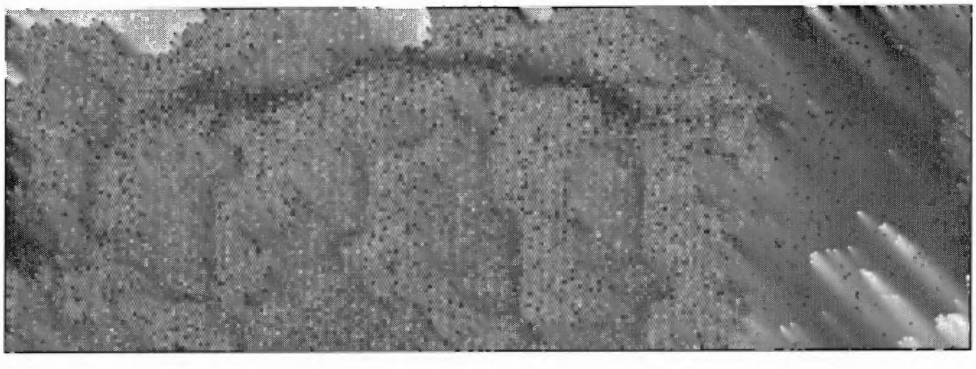

Figure A.64 Filament, original image with Gaussian noise, 50% of the noise level and 50% noise distribution.

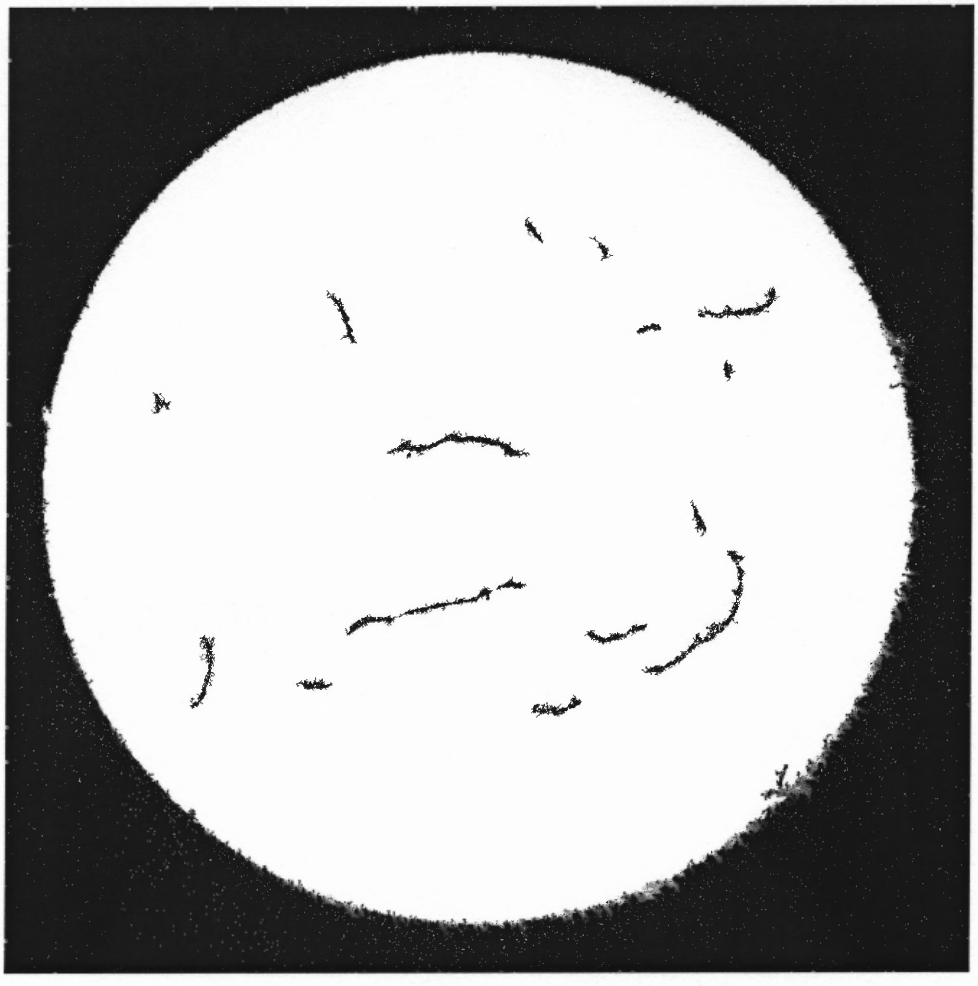

Figure A.65 Solar disk, the result of applying Method III to the image with Gaussian noise, 50% of the noise level and 50% noise distribution.

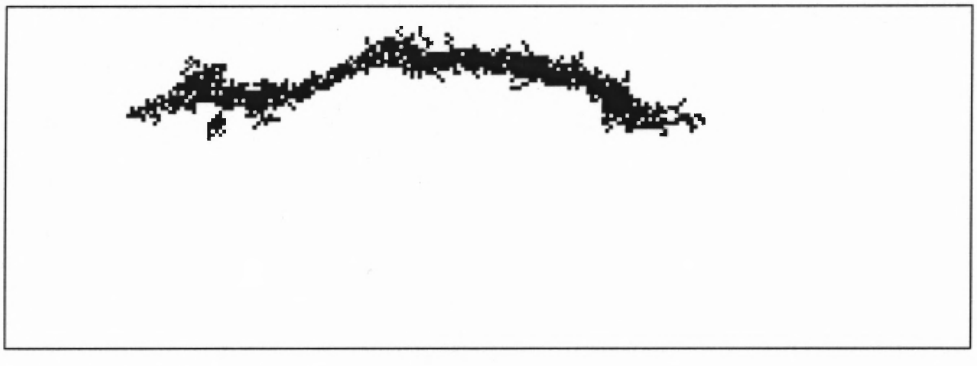

Figure A.66 Filament, the result of applying Method III to the image with Gaussian noise, 50% of the noise level and 50% noise distribution.

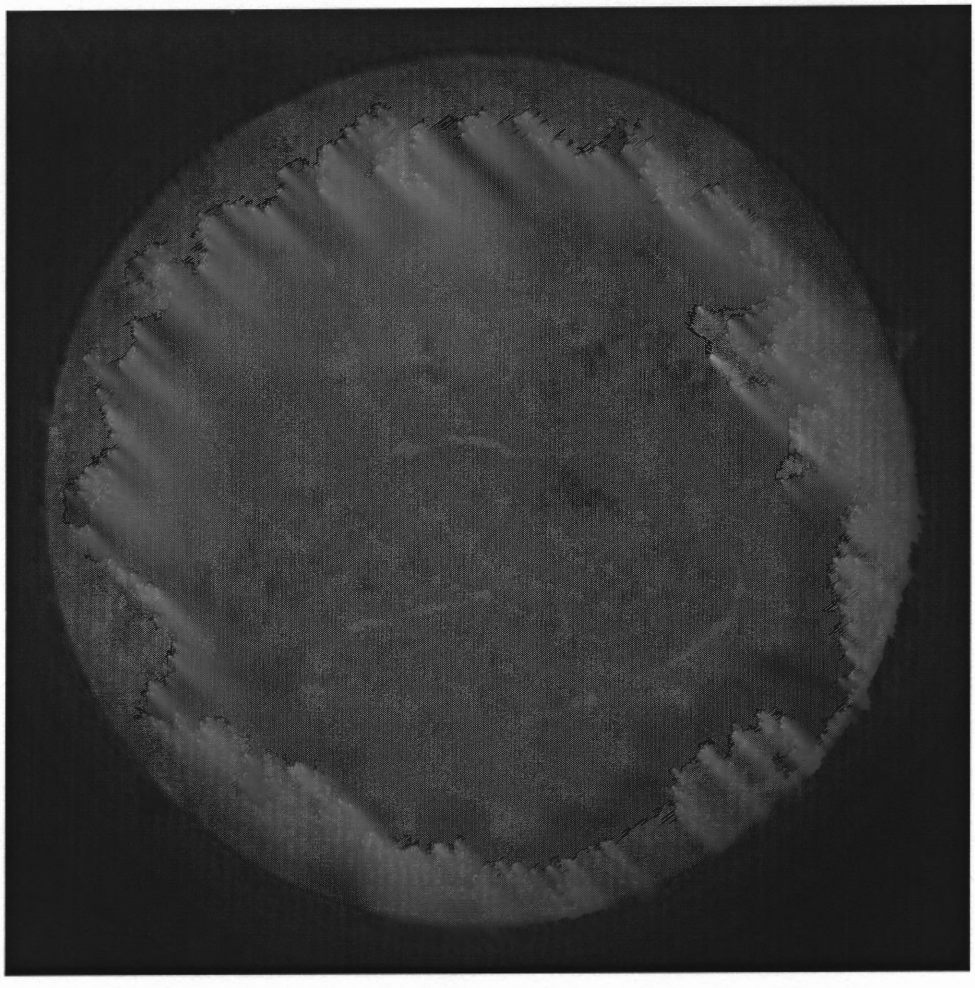

Figure A.67 Solar disk, original image with low pass blur, radius r=5 pixels.

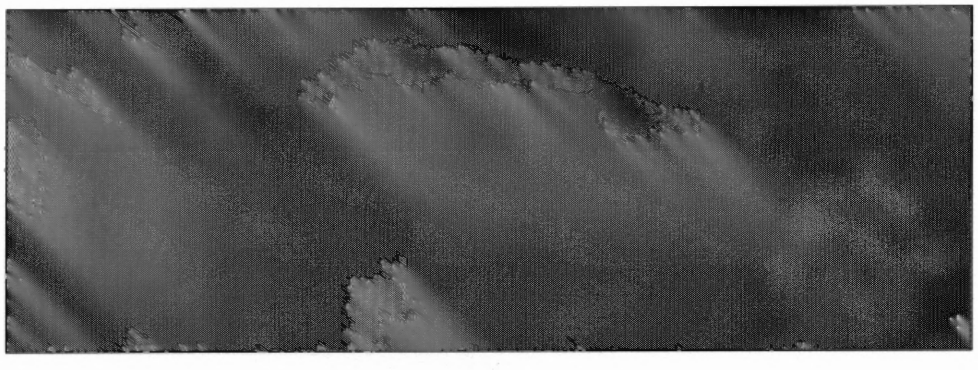

Figure A.68 Filament, original image with low pass blur, radius r=5 pixels.

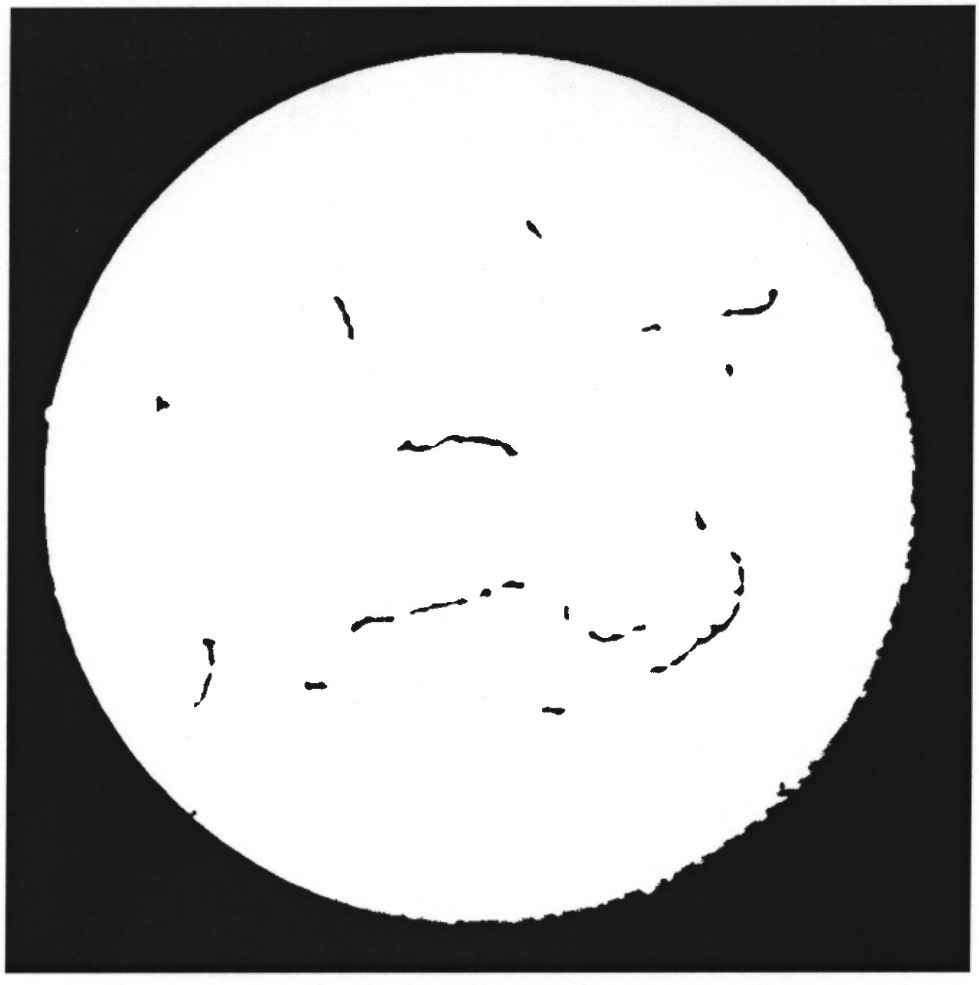

Figure A.69 Solar disk, the result of applying Method III to the image with low pass blur, radius r=5 pixels.

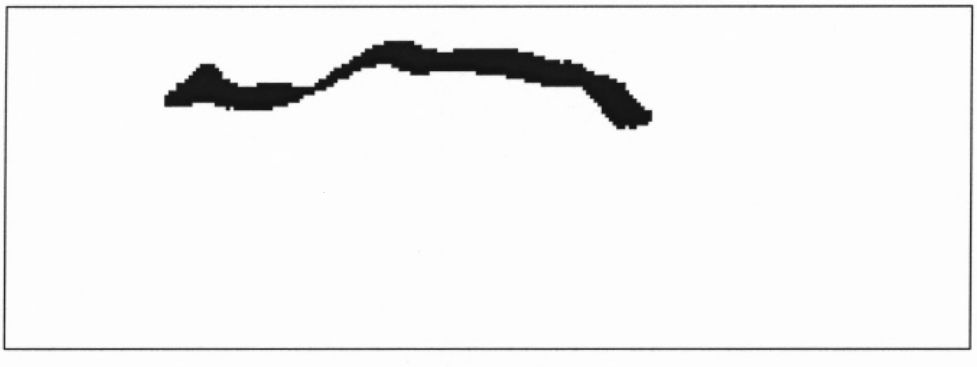

Figure A.70 Filament, the result of applying Method III to the image with with low pass blur, radius r=5 pixels.

APPENDIX B

IP_TOOLS (IMAGE PROCESSING SOFTWARE)

Solar image processing employing such a wide range of techniques requires a flexible software system, which would allow for the application of various known, as well as some newly developed techniques. Such a non-commercial system does not exist, so a new programming environment (IP_Tools) has been developed during the course of research on the methods presented in this dissertation.

The system was created as a MS-Windows application, based on three available software packages:

- FreeImage – a skeleton MS-Windows MDI application with I/O support for many image file formats (version 2.4.1, July 30, 2001)
- The Intel® Image Processing Library (IPL) - a set of low-level image manipulation functions in standard DLLs and static libraries form. This library contains functions that perform filtering, thresholding, and transforms (FFT, DCT, geometric), as well as arithmetic and morphological operations. The library uses a flexible image format, supporting channels of 1-, 8-, 16-, and 32-bit integer pixels, as well as 32-bit floating point pixels, with an arbitrary number of channels per image (version 2.5, October 6, 2000).
- OpenCV – an additional set of library functions used with the IPL-based system (version beta 2.1, December 8, 2001).

The new image processing application used FreeImage base as a MDI template, for I/O operations.

The IPL library allowed for implementation of the following classes of operations:

- Arithmetic and Logical
- Rotations
- Thresholding
- Histogram equalization
- Local Histogram Equalization
- Morphological (Erosion, Dilation, Opening and Closing with constant-size elements)

The OpenCV library allowed for further enhancements and development of more sophisticated methods:

- Enhanced image I/O
- Advanced thresholding
- Advanced Morphological Operations (with customized structure elements)
- Fixed Filters (Laplacian and Sobel)

Based on this skeleton, a few new operations were developed:

- Smooth local equalization
- Local thresholding
- Advanced local thresholding
- Region growing
- Filament detection through region growing
- Brightness normalization

- Limb darkening removal
- Sunspot removal
- Equal Area Projection
- Logging statistical image information
- Recursive directional filtering
- Composite preprocessing and feature extraction operations.

All operations performed on images are logged to a text log file, together with relevant operation parameters and processing time. The system allows for easy addition of new operations and may serve as a testing platform for new method development.

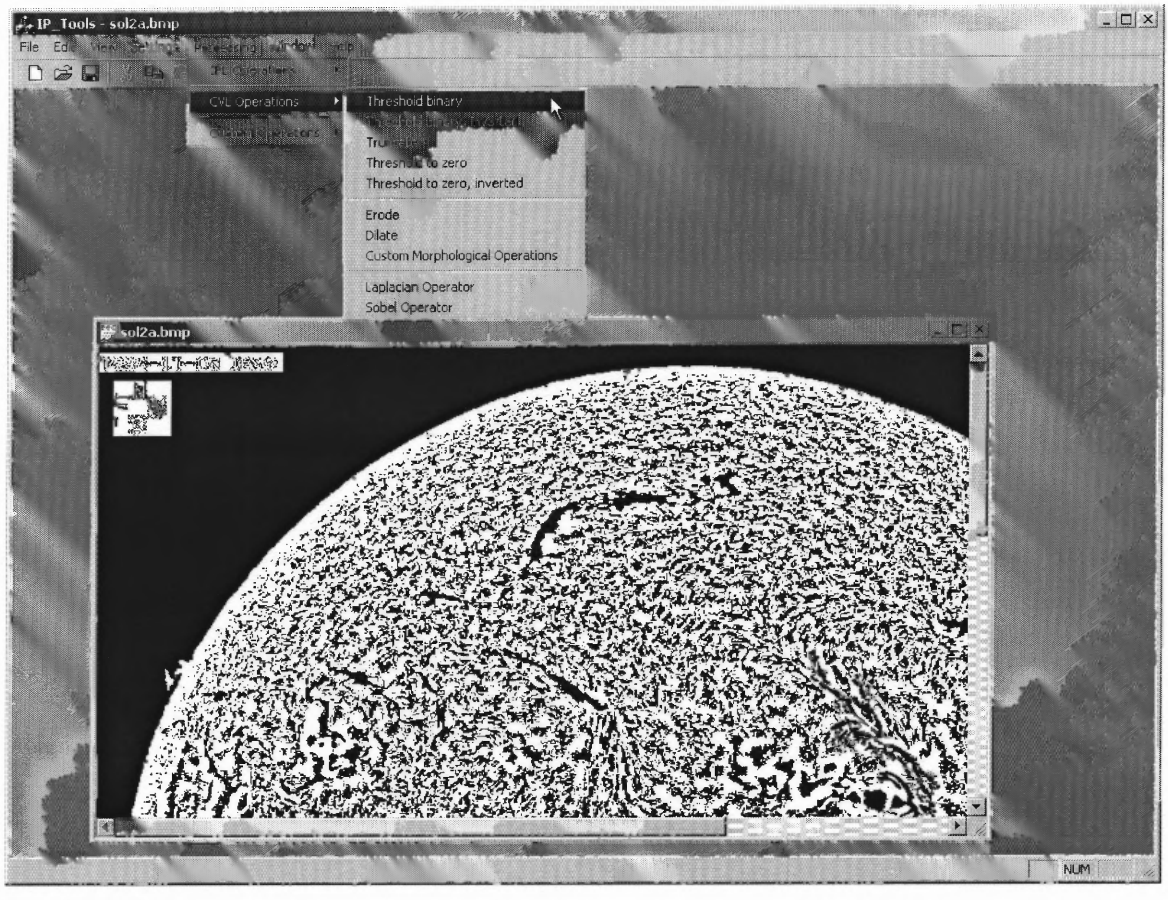

Figure B.1 A screen shot of IP_Tools.

APPENDIX C

GLOSSARY OF SOLAR-TERRESTRIAL TERMS

http://www.sec.noaa.gov/info/glossary.html

a INDEX. A 3-hourly "equivalent amplitude" index of local geomagnetic activity; "a" is related to the 3-hourly **K INDEX** according to the following scale:

K	0	1	2	3	4	5	6	7	8	9
a	0	3	7	15	27	48	80	140	240	400

A INDEX. A daily index of geomagnetic activity derived as the average of the eight 3-hourly a indices.

ACTIVE. Geomagnetic levels such that 15 is less than **Ap** which is less than 29.

ACTIVE. Solar activity levels with at least one geophysical event or several larger radio events (10cm) per day (Class M Flares)

ACTIVE DARK FILAMENT (ADF). An **ACTIVE PROMINENCE** seen on the **DISK**.

ACTIVE LONGITUDE. The approximate center of a range of heliographic longitudes in which **ACTIVE REGIONS** are more numerous and more **FLARE**-active than the average.

ACTIVE PROMINENCE. A **PROMINENCE** displaying material motion and changes in appearance over a few minutes of time.

ACTIVE PROMINENCE REGION (APR). A portion of the solar **LIMB** displaying **ACTIVE PROMINENCE**s.

ACTIVE REGION (AR). A localized, transient volume of the solar atmosphere in which **PLAGE**s, **SUNSPOTS**, **FACULA**e, **FLARE**s, etc. may be observed.

ACTIVE SURGE REGION (ASR). An **ACTIVE REGION** that exhibits a group or series of spike-like surges that rise above the limb.

AFRED. Abbreviation for the **A INDEX** for Fredericksburg.

ANGSTROM. A unit of length = 1.0E-08cm.

Ap INDEX. An averaged planetary **A INDEX** based on data from a set of specific stations.

ARCH FILAMENT SYSTEM (AFS). A bright, compact **PLAGE** crossed by a system of small, arched **FILAMENTS**, which is often a sign of rapid or continued growth in an **ACTIVE REGION**.

ASTRONOMICAL UNIT (AU). The mean earth-sun distance, equal to 1.496E+13cm or 214.94 solar radii.

AURORA. A faint visual phenomenon associated with geomagnetic activity, which occurs mainly in the high-latitude night sky; typical auroras are 100 to 250 km above the ground.

AURORAL OVAL. An oval band around each geomagnetic pole which is the locus of structured **AURORA**e.

AUTUMNAL EQUINOX. The equinox that occurs in September.

BARTEL'S ROTATION NUMBER. The serial number assigned to 27-day rotation periods of solar and geophysical parameters. Rotation 1 in this sequence was assigned arbitrarily by Bartel to begin in January 1833.

BRIGHT SURGE ON THE DISK (BSD). A bright gaseous stream (**SURGE**) emanating from the **CHROMOSPHERE**.

BRIGHT SURGE ON THE LIMB (BSL). A large gaseous stream (**SURGE**) that moves outward more than 0.15 solar radius above the **LIMB**.

BURST. A transient enhancement of the solar **RADIO EMISSION**, usually associated with an **ACTIVE REGION** or **FLARE**.

CARRINGTON LONGITUDE. A system of fixed longitudes rotating with the sun.

CENTIMETER BURST. A solar radio burst in the centimeter wavelength range.

CENTRAL MERIDIAN PASSAGE (CMP). The passage of an **ACTIVE REGION** or other feature across the longitude meridian that passes through the apparent center of the solar **DISK**.

CHROMOSPHERE. The layer of the solar atmosphere above the **PHOTOSPHERE** and beneath the transition region and the **CORONA**.

CHROMOSPHERIC EVENTS. Some flares are just Chromospheric Events without Centimetric Bursts or Effects. (SID) (Class C flare)

COMPREHENSIVE FLARE INDEX (CFI). The indicative of solar flare importance given by the sum of the following five components

a) Importance of ionizing radiation as indicated by time-associated Short Wave Fade or Sudden Ionospheric Disturbance; (Scale 0-3)

b) Importance of H-Alpha flare; (Scale 0-3)

c) Magnitude of 10cm flux; (Characteristic of log of flux in units of 10**-22Watt/m**2/Hz)

d) Dynamic spectrum; (Type II = 1, Continuum = 2, Type IV with duration > 10 minutes = 3)

e) Magnitude of 200MHz flux; (Characteristic of log of flux in units of 10**-22Watt/m**2/Hz)

CONJUGATE POINTS. Two points on the earth's surface, at opposite ends of a geomagnetic field line.

CONTINUUM STORM (CTM). General term for solar noise lasting for hours and sometimes days.

COORDINATED UNIVERSAL TIME (UTC). By international agreement, the local time at the prime meridian, which passes through Greenwich, England. Therefore, it is also known as **GREENWICH MEAN TIME**, or sometimes simply **UNIVERSAL TIME**.

CORONA. The outermost layer of the solar atmosphere, characterized by low densities (<1.0E+09/cc) and high temperatures (>1,0E+06deg.K).

CORONAL HOLE. An extended region of the **CORONA**, exceptionally low in density and associated with unipolar photospheric regions.

CORONAL RAIN (CRN). Material condensing in the **CORONA** and appearing to rain down into the **CHROMOSPHERE** as observed in **H-ALPHA** at the solar **LIMB** above strong **SUNSPOTS**.

CORONAL TRANSIENTS. A general term for short-time-scale changes in the **CORONA**, but principally used to describe outward-moving **PLASMA** clouds.

COSMIC RAY. An extremely energetic (relativistic) charged particle.

CROCHET. A sudden deviation in the sunlit geomagnetic field (H component; see **GEOMAGNETIC ELEMENTS**) associated with large solar **FLARE** X-ray emission.

D REGION. A daytime layer of the earth's **IONOSPHERE** approximately 50 to 90 km in altitude.

DARK SURGE ON DISK (DSD). Dark gaseous ejections visible in **H-ALPHA**.

DIFFERENTIAL ROTATION. The change in **SOLAR ROTATION RATE** with latitude. Low latitudes rotate at a faster angular rate (approx. 14 degrees per day) than do high latitudes (approx. 12 degrees per day).

DISAPPEARING SOLAR FILAMENT (DSF). The sudden (timescale of minutes to hours) disappearance of a solar **FILAMENT (PROMINENCE)**.

DISK. The visible surface of the sun (or any heavenly body) projected against the sky.

Dst INDEX. A geomagnetic index describing variations in the equatorial ringcurrent.

E REGION. A daytime layer of the earth's **IONOSPHERE** roughly between the altitudes of 85 and 140 km.

EMERGING FLUX REGION (EFR). An area on the sun where new magnetic flux is erupting.

ERUPTIVE. Solar activity levels with at least one radio event (10cm) and several chromospheric events per day (Class C Flares)

ERUPTIVE PROMINENCE ON LIMB (EPL). A solar **PROMINENCE** that becomes activated and is seen to ascend from the sun.

EXTREMELY LOW FREQUENCY (ELF). That portion of the radio frequency spectrum from 30 to 3000 hertz.

EXTREME ULTRAVIOLET (EUV). A portion of the electromagnetic spectrum from approximately 100 to 1000 angstroms.

F CORONA. Of the white-light **CORONA** (that is, the corona seen by the eye at a total solar (ECLIPSE), that portion which is caused by sunlight scattered or reflected by solid particles (dust) in inter-planetary space.

F REGION. The upper layer of the **IONOSPHERE**, approximately 120 to 1500 km in altitude. The F region is subdivided into the F1 and F2 regions. The F2 region is the most dense and peaks at altitudes between 200 and 600 km. The F1 region is a smaller peak in electron density, which forms at lower altitudes in the daytime.

FACULA. A bright region of the **PHOTOSPHERE** seen in white light, seldom visible except near the solar **LIMB**.

FIBRIL. A linear pattern in the **H-ALPHA CHROMOSPHERE** of the sun, as seen through an H-alpha filter, occurring near strong **SUNSPOTS** and **PLAGE** or in **FILAMENT** channels.

FILAMENT. A mass of gas suspended over the **PHOTOSPHERE** by magnetic fields and seen as dark lines threaded over the solar **DISK**. A filament on the **LIMB** of the sun seen in emission against the dark sky is called a **PROMINENCE**.

FILAMENT CHANNEL. A broad pattern of **FIBRILS** in the **CHROMOSPHERE**, marking where a **FILAMENT** may soon form or where a filament recently disappeared.

FLARE. A sudden eruption of energy on the solar **DISK** lasting minutes to hours, from which radiation and particles are emitted.

FLUENCE. Time integrated flux.

FLUX. The rate of flow of a physical quantity through a reference surface.

fMIN. The lowest radiowave frequency that can be reflected from the IONOSPHERE.

foEs. The maximum ORDINARY MODE radiowave frequency capable of reflection from the **SPORADIC E REGION** of the **IONOSPHERE**.

foF2. The maximum ORDINARY MODE radiowave frequency capable of reflection from the F2 REGION of the **IONOSPHERE**.

FORBUSH DECREASE. An abrupt decrease, of at least 10%, of the background galactic **COSMIC RAY** intensity as observed by neutron monitors.

GAMMA. A unit of magnetic field intensity equal to 1 x 10.0E-05 **GAUSS**, also equal to 1 **NANOTESLA**.

GAMMA RAYS. High energy radiation (energies in excess of 100 keV) observed during large, extremely energetic solar **FLARES**.

GAUSS. The unit of magnetic induction in the cgs (centimeter-gram-second) system.

GEOMAGNETIC ELEMENTS. The components of the geomagnetic field at the surface of the earth. In SESC use, the northward and eastward components are often called the H and D components, where the D component is expressed in gammas and is derived from D (the declination angle) using the small angle approximation.

GEOMAGNETIC FIELD. The magnetic field observed in and around the earth. The intensity of the magnetic field at the earth's surface is approximately 0.32 gauss at the equator and 0.62 gauss at the north pole.

GEOMAGNETIC STORM. A worldwide disturbance of the earth's magnetic field, distinct from regular diurnal variations.

Minor Geomagnetic Storm: A storm for which the **Ap** index was greater than 29 and less than 50.

Major Geomagnetic Storm: A storm for which the **Ap** index was greater than 49 and less than 100.

Severe Geomagnetic Storm: A storm for which the **Ap** index was 100 or more.

Initial Phase: Of a geomagnetic storm, that period when there may be an increase of the **MIDDLE-LATITUDE** horizontal intensity (H).

Main Phase: Of a geomagnetic storm, that period when the horizontal magnetic field at middle latitudes is generally decreasing.

Recovery Phase: Of a geomagnetic storm, that period when the depressed northward field component returns to normal levels.

GEOPHYSICAL EVENTS. Flares (Importance two or larger) with Centimetric Outbursts (maximum of the flux higher than the Quiet Sun flux, duration longer 10 minutes) and/or strong **SID**. Sometimes these flares are followed by **Geomagnetic Storms** or small PCA. (Class M Flares)

GEOSYNCHRONOUS. Term applied to any equatorial satellite with an orbital velocity equal to the rotational velocity of the earth. The net effect is that the satellite is virtually motionless with respect to an observer on the ground.

GMT. Greenwich Mean Time. (See **COORDINATED UNIVERSAL TIME.**)

GRADUAL COMMENCEMENT. The commencement of a geomagnetic storm that has no well-defined onset.

GRANULATION. Cellular structure of the **PHOTOSPHERE** visible at high spatial resolution.

GREEN LINE. The green line is one of the strongest (and first-recognized) visible coronal lines. It identifies moderate temperature regions of the **CORONA**.

GROUND-LEVEL EVENT (GLE). A sharp increase in ground-level **COSMIC RAY** count to at least 10% above background, associated with solar protons of energies greater than 500 MeV. GLEs are relatively rare, occurring only a few times each **SOLAR CYCLE**.

H-ALPHA. This ABSORPTION LINE of neutral hydrogen falls in the red part of the visible spectrum and is convenient for solar observations. The H-alpha line is universally used for patrol observations of solar flares.

H-component of the Geomagnetic Field. See **GEOMAGNETIC ELEMENTS.**

HIGH ENERGY EVENT. Flares (class two or more) with outstanding Centimetric Bursts and **SID**. High Energy Protons are reported at the Earth in case of most of these events occurring on the western part of solar disk. (Class X flares)

HIGH FREQUENCY (HF). That portion of the radio frequency spectrum between between 3 and 30 MHz.

HIGH LATITUDES. With specific reference to zones of geomagnetic activity, "high latitudes" refers to 50o to 80o geomagnetic.

HIGH-SPEED STREAM. A feature of the **SOLAR WIND** having velocities that are about double average solar wind values.

HOMOLOGOUS FLARES. Solar flares that occur repetitively in the same **ACTIVE REGION**, with essentially the same position and with a common pattern of development.

HYDER FLARE. A **FILAMENT**-associated **TWO-RIBBON FLARE**, often occurring in spotless regions. The flare presumably results from the impact on the **CHROMOSPHERE** of infalling **FILAMENT** material.

INTERPLANETARY MAGNETIC FIELD (IMF). The magnetic field carried with the **SOLAR WIND**.

IONOSPHERE. The region of the earth's upper atmosphere containing a small percentage of free electrons and ions produced by photoionization of the constituents of the atmosphere by solar ultraviolet radiation at very short wavelengths (l.t.1000 angstroms). The ionosphere significantly influences radiowave propagation of frequencies less than about 30 MHz.

IONOSPHERIC STORM. A disturbance in the **F REGION** of the **IONOSPHERE**, which occurs in connection with geomagnetic activity.

K CORONA. Of the white-light **CORONA** (that is, the corona seen by the eye at a total solar eclipse), that portion which is caused by sunlight scattered by electrons in the hot outer atmosphere of the sun.

K INDEX. A 3-hourly quasi-logarithmic local index of geomagnetic activity relative to an assumed quiet-day curve for the recording site. Range is from 0 to 9. The K index measures the deviation of the most disturbed horizontal component.

KELVIN. A unit of absolute temperature.

Kp INDEX. A 3-hourly planetary geomagnetic index of activity generated in Gottingen, Germany, based on the K INDEX from 12 or 13 stations distributed around the world.

LEADER SPOT In a magnetically bipolar or multipolar **SUNSPOT** group, the western part precedes and the main spot in that part is called the leader.

LIGHT BRIDGE. Observed in white light, a bright tongue or streaks penetrating or crossing **SUNSPOT UMBRA**e. The appearance of a light bridge is frequently a sign of impending region division or dissolution.

LIMB. The edge of the solar **DISK**.

LIMB FLARE. A solar **FLARE** seen at the edge (LIMB) of the sun.

LOOP PROMINENCE SYSTEM (LPS). A system of loop prominences associated with major **FLARES**.

LOW FREQUENCY (LF). That portion of the radio frequency spectrum from 30 to 300 kHz.

M 3000. The optimum **HIGH FREQUENCY** radio wave with a 3000 km range, which reflects only once from the **IONOSPHERE** (single hop transmission).

MAGFLARE. A geomagnetic and/or cosmic storm has been associated with this flare.

MAGNETIC BAY. A relatively smooth excursion of the H (horizontal) component (see **GEOMAGNETIC ELEMENTS**) of the geomagnetic field away from and returning to quiet levels.

MAGNETOGRAM. Solar magnetograms are a graphic representation of solar magnetic field strengths and polarity.

MAGNETOPAUSE. The boundary layer between the **SOLAR WIND** and the **MAGNETOSPHERE**.

MAGNETOSPHERE. The magnetic cavity surrounding the earth, carved out of the passing **SOLAR WIND** by virtue of the **GEOMAGNETIC FIELD**, which prevents, or at least impedes, the direct entry of the **SOLAR WIND PLASMA** into the cavity.

MAJORFLARE. This flare is the basis for the forecast of geomagstorm, cosmic storm and/or protons in the earth's vicinity.

MeV. Mega (million) electronvolt. A unit of energy used to describe the total energy carried by a particle or photon.

MEDIUM FREQUENCY. (MF). That portion of the radio frequency spectrum from 0.3 to 3 MHz.

MICROWAVE BURST. A radiowave signal associated with optical and/or X-ray FLAREs.

MIDDLE LATITUDES. With specific reference to zones of geomagnetic activity, "middle latitudes" refers to 20 deg. to 50 deg. geomagnetic.

MOUNT WILSON MAGNETIC CLASSIFICATIONS.

Alpha. Denotes a unipolar **SUNSPOT** group.

Beta. A sunspot group having both positive and negative magnetic polarities, with a simple and distinct division betweenthe polarities.

Beta-Gamma. A sunspot group that is bipolar but in which no continuous line can be drawn separating spots of opposite polarities.

Delta. A complex magnetic configuration of a solar sunspot group consisting of opposite polarity **UMBRA**e within the same **PENUMBRA**.

Gamma. A complex **ACTIVE REGION** in which the positive and negative polarities are so irregularly distributed as to prevent classification as a bipolar group.

NANOTESLA (nT). A unit of magnetism 10.0E-09 tesla, equivalent to a gamma (10.0E-05 gauss).

NEUTRAL LINE. The line that separates longitudinal magnetic fields of opposite polarity.

PENUMBRA. The **SUNSPOT** area that may surround the darker **UMBRA** or umbrae. It consists of linear bright and dark elements radial from the sunspot umbra.

PERSISTENCE. Continuation of existing conditions. When a physical parameter varies slowly, the best prediction is often persistence.

PHOTOSPHERE. The lowest layer of the solar atmosphere; corresponds to the solar surface viewed in **WHITE LIGHT**. **SUNSPOTs** and **FACULAe** are observed in the photosphere.

PLAGE. An extended emission feature of an **ACTIVE REGION** that exists from the emergence of the first magnetic flux until the widely scattered remnant magnetic fields merge with the background.

PLAGE CORRIDOR. A space in chromospheric (see **CHROMOSPHERE**) **PLAGE** lacking plage intensity, coinciding with polarity inversion line.

PLAGENIL. Spotless disc free of calcium plage.

PLASMA. Any ionized gas, that is, any gas containing ions and electrons.

POLAR CAP ABSORPTION (PCA). An anomalous condition of the polar **IONOSPHERE** whereby HF and VHF (3 - 300 MHz) radiowaves are absorbed, and LF and VLF (3 - 300 kHz) radiowaves are reflected at lower altitudes than normal. In practice, the absorption is inferred from the proton flux at energies greater than 10 MeV, so that PCAs and **PROTON EVENT**s are simultaneous. Transpolar radio paths may still be disturbed for days, up to weeks, following the end of a proton event.

POST-FLARE LOOPS. A **LOOP PROMINENCE SYSTEM** often seen after a major **TWO-RIBBON FLARE**, which bridges the ribbons.

PROMINENCE. A term identifying cloud-like features in the solar atmosphere. The features appear as bright structures in the **CORONA** above the solar **LIMB** and as dark **FILAMENT**s when seen projected against the solar **DISK**.

PROTON. Solar activity levels with at least on high energy event (Class X Flares)

PROTON EVENT. By definition, the measurement of at least 10 protons/sq.cm/sec/steradian at energies greater than 10 MeV.

PROTON FLARE. Any **FLARE** producing significant **FLUX**es of greater-than-10 MeV protons in the vicinity of the earth.

QUIESCENT PROMINENCE (FILAMENT). Long, sheet-like prominences nearly vertical to the solar surface.

QUIET. A descriptive word specifically meaning geomagnetic levels such that **Ap** < 8 (see **Ap** INDEX).

QUIET. Solar activity levels with less than one chromospheric event per day

RADIO EMISSION. Emissions of the sun in radio wavelengths from centimeters to dekameters, under both quiet and disturbed conditions.

Type I. A noise storm composed of many short, narrow-band bursts in the metric range (300 - 50 MHz).

Type II. Narrow-band emission that begins in the meter range (300 MHz) and sweeps slowly (tens of minutes) toward dekameter wavelengths (10 MHz). Type II emissions occur in loose association with major **FLARE**s and are indicative of a shock wave moving through the solar atmosphere.

Type III. Narrow-band bursts that sweep rapidly (seconds) from decimeter to dekameter wavelengths (500 - 0.5 MHz). They often occur in groups and are an occasional feature of complex solar **ACTIVE REGION**s.

Type IV. A smooth continuum of broad-band bursts primarily in the meter range (300 - 30 MHz). These bursts are associated with some major **FLARE** events beginning 10 to 20 minutes after the flare maximum, and can last for hours.

RADIO EVENT. Flares with Centimetric Bursts and/or definite Ionospheric Event (**SID**).

RECURRENCE. Used especially in reference to the recurrence of physical parameters every 27 days (the rotation period of the sun).

RIOMETER (Relative Ionospheric Opacity meter). A specially designed radio receiver for continuous monitoring of cosmic noise. The absorption of cosmic noise in the polar regions is very sensitive to the solar low-energy **COSMIC RAY** flux.

SECTOR BOUNDARY. In the **SOLAR WIND**, the area of demarcation between sectors, which are large-scale features distinguished by the predominant direction of the **interplanetary magnetic field**, toward or away from the sun.

SHORT WAVE FADE (SWF). A particular ionospheric solar flare effect under the broad category of sudden ionospheric disturbances (**SIDs**) whereby short-wavelength radio transmissions, VLF, through HF, are absorbed for a period of minutes to hours.

SMOOTHED SUNSPOT NUMBER. An average of 13 monthly RI numbers, centered on the month of concern.

SOLAR COORDINATES. Central Meridian Distance (CMD). The angular distance in solar longitude measured from the central meridian.

SOLAR CYCLE. The approximately 11-year quasi-periodic variation in frequency or number of solar active events.

SOLAR MAXIMUM. The month(s) during the **SOLAR CYCLE** when the 12-month mean of monthly average **SUNSPOT** NUMBERS reaches a maximum. The most recent solar maximum occurred in July 1989.

SOLAR MINIMUM. The month(s) during the **SOLAR CYCLE** when the 12-month mean of monthly average **SUNSPOT NUMBERS** reaches a minimum. The most recent minimum occurred in September 1986.

SOLAR SECTOR BOUNDARY (SSB). The apparent solar origin, or base, of the interplanetary **SECTOR BOUNDARY** marked by the larger-scale polarity inversion lines.

SOLAR WIND. The outward flux of solar particles and magnetic fields from sun. Typically, solar wind velocities are near 350 km/s.

SPORADIC E. A phenomenon occurring in the **E REGION** of the **IONOSPHERE**, which significantly affects HF radiowave propagation. Sporadic E can occur during daytime or nighttime and it varies markedly with latitude.

SPOTNIL. Spotless **DISK**

SUDDEN COMMENCEMENT(SC, or SSC for Storm Sudden Commencement). An abrupt increase or decrease in the northward component of the geomagnetic field, which marks the beginning of a **GEOMAGNETIC STORM**.

SUDDEN IMPULSE (SI+ or SI-). A sudden perturbation of several gammas in the northward component of the low-latitude geomagnetic field, not associated with a following **GEOMAGNETIC STORM**. (An SI becomes an SC if a storm follows.)

SUDDEN IONOSPHERIC DISTURBANCE (SID). HF propagation anomalies due to ionospheric changes resulting from solar **FLAREs, PROTON EVENTs** and **GEOMAGNETIC STORMs**.

SUNSPOT. An area seen as a dark spot on the PHOTOSPHERE of the sun. Sunspots are concentrations of magnetic flux, typically occurring in bipolar clusters or groups. They appear dark because they are cooler than the surrounding photosphere.

SUNSPOT GROUP CLASSIFICATION (Modified Zurich Sunspot Classification).

A - small single unipolar **SUNSPOT** or very small group of spots without **PENUMBRA**.

B - Bipolar sunspot group with no penumbra.

C - An elongated bipolar sunspot group. One sunspot must have penumbra.

D - An elongated bipolar sunspot group with penumbra on both ends of the group.

E - An elongated bipolar sunspot group with penumbra on both ends. Longitudinal extent of penumbra exceeds 10 deg. But not 15 deg.

F - An elongated bipolar sunspot group with penumbra on both ends. Longitudinal extent of penumbra exceeds 15 deg.

H - A unipolar sunspot group with penumbra.

SUNSPOT NUMBER. A daily index of **SUNSPOT** activity (R), defined as $R = k (10 g + s)$ where S = number of individual spots, g = number of sunspot groups, and k is an observatory factor.

SURGE. A jet of material from **ACTIVE REGIONs** that reaches coronal heights and then either fades or returns into the **CHROMOSPHERE** along the trajectory of ascent.

TWO-RIBBON FLARE. A **FLARE** that has developed as a pair of bright strands (ribbons) on both sides of the main inversion ("neutral") line of the magnetic field of the **ACTIVE REGION**.

TYPE I, II, III, IV. See **RADIO EMISSION**

U BURST. A fast radio burst spectrum of a **FLARE**. It has a U-shaped appearance in an intensity-vs.-frequency plot.

ULTRA HIGH FREQUENCY (UHF). Those radio frequencies exceeding 300 MHz.

UMBRA. The dark core or cores (umbrae) in a **SUNSPOT** with **PENUMBRA**, or a sunspot lacking **PENUMBRA**.

UNIVERSAL TIME (UT). See **COORDINATED UNIVERSAL TIME**.

UNSETTLED. With regard to geomagnetic levels, a descriptive word specifically meaning that 8 is less than or equal to the **Ap** INDEX which is less than or equal to15.

UTC. See **COORDINATED UNIVERSAL TIME**.

VERY HIGH FREQUENCY (VHF). That portion of the radio frequency spectrum from 30 to 300 MHz.

VERY LOW FREQUENCY (VLF). That portion of the radio frequency spectrum from 3 to 30 kHz.

WHITE LIGHT (WL). Sunlight integrated over the visible portion of the spectrum (4000 - 7000 angstroms) so that all colors are blended to appear white to the eye.

WHITE LIGHT FLARE. A major **FLARE** in which small parts become visible in white light. Such flares are usually strong X-ray, radio, and particle emitters.

WOLF NUMBER. An historic term for **SUNSPOT NUMBER**. In 1849, R. Wolf of Zurich originated the general procedure for computing the sunspot number.

X-RAY BACKGROUND. A daily average background X-ray flux in the 1 to 8 angstrom range. It is a midday minimum designed to reduce the effects of **FLAREs**.

X-RAY BURST. A temporary enhancement of the X-ray emission of the sun. The time-intensity profile of soft X-ray bursts is similar to that of the **H-ALPHA** profile of an associated **FLARE**.

X-RAY FLARE CLASS. Rank of a **FLARE** based on its X-ray energy output. Flares are classified by the order of magnitude of the peak burst intensity (I) measured at the earth in the 1 to 8 angstrom band as follows:

Class	(in Watt/sq. Meter)
B	I less than (l.t.) 10.0E-06
C	10.0E-06 l.e.= I l.t.= 10.0E-05
M	10.0E-05 l.e.= I l.t.= 10.0E-04
X	I g.e.= 10.0E-04

ZURICH SUNSPOT CLASSIFICATION. A **SUNSPOT** classification system that has been modified for SESC use.

REFERENCES

[1] Amerinex Applied Imaging, Inc. TRACS - Toolkit for Recognition and Automatic Classification of Solar Features. Retrieved April 15, 2003 from the World Wide Web: http://www.aai.com/AAI/NOAA/NOAA.html.

[2] Mark R. Banham and Aggelos K. Katsaggelos, "Digital Image Restoration," IEEE Signal Processing Magazine, Vol. 14, No. 2, pp. 24-41, March 1997.

[3] U. Bhattacharya, V. Liebscher, A. Datta, S.K. Parui, K. Rodenacker, B.B. Chaudhuri, "Shape Extraction of Volumetric Images of Filamentous Bacteria Using Topology Adaptive Self Organization," Proceedings of the 15th International Conference on Pattern Recognition, Volume 2, pp. 291-294, 2000.

[4] Joydeep Bhattacharya, Ernesto Pereda, Rangaiah Kariyappa, Partha Pratim Kanjilal, "Application of Non-linear Analysis to Intensity Oscillations of the Chromospheric Bright Points," Solar Physics, Vol. 199, No. 2, pp. 267-290, April 2001.

[5] The Big Bear Solar Observatory WWW Page. Retrieved April 15, 2003 from the World Wide Web: http://www.bbso.njit.edu.

[6] Yves Bobichon, Albert Bijaoui, "Restoration of Lossy Compressed Astronomical Images," Proceedings of the International Conference on Image Processing, Vol. 1, pp. 33-36, 1996.

[7] Ulisses M. Braga Neto, "Connectivity in mage processing and analysis: theory, multiscale extensions and applications," PhD Thesis, Electrical and Computer Engineering Department, Johns Hopkins University, Baltimore, MD, 2001. Retrieved April 15, 2003 from the World Wide Web: http://iacl.ece.jhu.edu/~ulisses/thesis.pdf.

[8] D.S. Brown and E.R. Priest, "The Topological Behaviour of Stable Magnetic Separators," Solar Physics, Vol. 190, pp. 25-33, December 1999.

[9] N. Brynildsen, P. Maltby, P. Brekke, S.V.H. Haugan, O. Kjeldseth-Moe, "Soho Observations of the Structure and Dynamics of Sunspot Region Atmospheres," Solar Physics, Vol. 186, pp. 141-191, May 1999.

[10] I. Joseph Burt, "Transition Region and Coronal Explorer Mission," Proceedings of the Aerospace Applications Conference, Vol. 2, pp. 197-212, February 1996.

[11] Alcione Jandir Candeas, Ulisses de Mendonça Braga Neto, and Edson Costa de Barros Carvalho Filho, "A mathematical morphology approach to the characterization of astronomical objects," SIBGRAPI 96, IX Simpósio Brasileiro de Computação Gráfica e Processamento de Imagens, Conference Proceedings, pp. 235-242, October 1996.

[12] Jongchul Chae, Hong Sik Yun, Takashi Sakurai and Kiyoshi Ichimoto, "Stray Light Correction in Magnetograph Observations Using the Maximum Entropy Method," Solar Physics, Vol. 183, No. 2, pp. 245-261, December 1998.

[13] Steve A. Chien and Helen B. Mortensen, "Automating image processing for scientific data analysis of a large image database," IEEE Transactions on Pattern Analysis and Machine Intelligence, Vol. 18, No. 8, pp. 854-859, August1996.

[14] Frances Cleveland, Wade Malcolm, Daniel E. Nordell, Jack Zirker, "Solar Effects on Communications," IEEE Transactions on Power Delivery, Vol. 7, No. 2, pp. 460-468, April 1992.

[15] E.B. Christopoulou, A.A. Georgakilas, and S. Koutchmy, "Fine Structure of the Magnetic Chromosphere: Near-Limb Imaging, Data Processing and Analysis of Spicules and Mottles," Solar Physics, Vol. 199, No. 1, pp. 61-80, March 2001.

[16] Andre Csillaghy, D. M. Zarro and Sam L. Freeland, "Steps Towards a Virtual Solar Observatory," IEEE Signal Processing Magazine, Vol. 18, No. 2, pp. 41-48, March 2001.

[17] Rita Cucchiara and Fabio Filicori, "The Vector-Gradient Hough Transform," IEEE Transactions on Pattern Analysis and Machine Intelligence, Vol. 20, No. 7, pp. 746-750, July 1998.

[18] C. Denker, A. Johannesson, W. Marquette, P.R. Goode, H. Wang, H. Zirin, "Synoptic Hα Full-Disk Observations of the Sun from Big Bear Solar Observatory – I. Instrumentation, Image Processing, Data Products, and First Results," Solar Physics, Vol. 184, No. 1, pp. 87-102, January 1999.

[19] C. Denker, G. Yang, H. Wang, "Near Real-Time Image Reconstruction," Solar Physics, Vol. 202, No. 1, pp. 63-70, August 2001.

[20] V.N. Dermendjiev, N.I. Petrov, M. Tz. Detchev, B. Rompolt, P. Rudawy, "Line-of-Sight Velocity Fluctuations of a Quiescent Prominence," Solar Physics, Vol. 202, No. 1, pp. 99-107, August 2001.

[21] C. Richard DeVore and Spiro K. Antiochos, "Dynamical Formation and Stability of Helical Prominence Magnetic Fields," The Astrophysical Journal, Vol. 539, No. 2, pp. 954-963, August 2000.

[22] Edward R. Dougherty, "Optimal Conjunctive Granulometric Bandpass Filters," Journal of Mathematical Imaging and Vision, Vol. 14, 2001.

[23] Edward R. Dougherty and Yidong Chen, "Granulometric Filters," Chapter 4 in *Nonlinear Filtering for Image Processing*, eds. E. Dougherty and J. Astola, SPIE and IEEE Presses, 1999.

[24] Cristiana Dumitrache, "On The Evolution of Filaments," Solar Physics, Vol. 173, No. 2, pp. 281-304, July 1997.

[25] Brent L. Ellerbroek and Robert J. Plemmons, "Computations in astro-imaging," Proceedings of The International Conference on Image Processing, Vol. 3, pp. 113-116, 1996.

[26] Jianlin Gao, Haimin Wang and Mengchu Zhou, "Development of an Automatic Filament Disappearance Detection System," Solar Physics, Vol. 205, No. 1, pp. 93-103, January 2002.

[27] V. Gaizauskas , D. H. Mackay , and K. L. Harvey, "Evolution of Solar Filament Channels Observed during a Major Poleward Surge of Photospheric Magnetic Flux," The Astrophysical Journal, Vol. 558, No. 2, pp. 888-902, September 2001.

[28] V. Gaizauskas, J. B. Zirker, C. Sweetland, and A. Kovacs, "Formation of a Solar Filament Channel," The Astrophysical Journal, Vol. 479, No. 1, pp. 448-457, April 1997.

[29] Alois Goller, Franz Leberl, "Radar image processing with clusters of computers," Aerospace Conference Proceedings, 2000 IEEE , Vol. 3, pp. 281-285, March 2000.

[30] Rafael C. Gonzalez and Richard E. Woods, *Digital Image Processing*, Addison-Wesley Publishing Company, Inc., June 1992.

[31] Michael Greene, Hong Tan, "Solar tracking: design and simulation (X-ray emission detection)," Proceedings of the Twentieth Southeastern Symposium on System Theory, pp. 208-212, March 1988.

[32] Peter H. Gregson, "Automatic neural arbor reconstruction," Conference Record of the Nuclear Science Symposium and Medical Imaging Conference, Vol. 3, pp. 2133-2139, November 1991.

[33] Matthew Hill, Vittorio Castelli, Chung-Sheng Li, Yuan-Chi Chang, Barbara Thompson, Lawrence Bergman, John R. Smith, "Solarspire: querying temporal solar imagery by content," Proceedings of the International Conference on Image Processing, Vol. 1, pp. 834-837, October 2001.

[34] H. Imamura, Y. Kitaoka, Y. Katsuma, Y. Kenmochi, K. Kotani, "Estimation of stereo image pairs from single-camera views for a rotating spherical object covered with moving texture," Proceedings of International Conference on Image Processing (ICIP 99), Vol. 4, pp. 400-404, October 1999.

[35] A. Irbah, M. Bouzaria, L. Lakhal, R. Moussaoui, J. Borgnino, F. Laclare, C. Delmas, "Feature extraction from solar images using wavelet transform: image cleaning for applications to solar astrolabe experiment," Solar Physics, Vol. 185, No. 2, pp. 255-273, April 1999.

[36] Radovan Krejčí, Jan Flusser and Stanislava Šimberová, "A new Multichannel Blind Deconvolution Method and its Application to Solar Images," Proceedings of the Fourteenth International Conference on Pattern Recognition, Vol. 2 , pp. 1765-1767, August 1998.

[37] Deepa Kundur and Dimitrios Hatzinakos, "A Novel Blind Deconvolution Scheme for Image Restoration Using Recursive Filtering," IEEE Transactions On Signal Processing, Vol. 46, No. 2, pp. 375-390, February 1998.

[38] Dawn D. Lenz, Edward E. DeLuca, Leon Golub, Robert Rosner, Jay A. Bookbinder, Christof Litwin, Fabio Reale, Giovanni Peres, "Long-lived Coronal Loop Profiles from TRACE," Solar Physics, Vol. 190, pp. 131-138, December 1999.

[39] Isaac J. H. Leung, James E. Jordan, "Image processing for weather satellite cloud segmentation," Canadian Conference on Electrical and Computer Engineering, Vol. 2, pp. 953-956, September 1995.

[40] Yuri E. Litvinenko, "On the Magnetic Field Orientation and Plasma Flows in Solar Filament Barbs," Solar Physics, Vol. 196, No. 2, pp. 369-375, October 2000.

[41] Matthew Lybanon, Suzanne M. Lea, Susan M. Himes, "Segmentation of diverse image types using opening and closing," Proceedings of the 12th IAPR International Conference on Pattern Recognition, Vol. 1 - Conference A: Computer Vision & Image Processing, pp. 347-351, October 1994.

[42] D. H. Mackay , V. Gaizauskas, and A. A. van Ballegooijen, "Comparison of Theory and Observations of the Chirality of Filaments within a Dispersing Activity Complex," The Astrophysical Journal, Vol. 544, No. 2, pp. 1122-1134, December 2000.

[43] Petrus C. Martens and Cornelis Zwaan, "Origin and Evolution of Filament-Prominence Systems," The Astrophysical Journal, Vol. 558, No. 2, pp. 872-887, September 2001.

[44] Sara F. Martin, "Conditions for the Formation and Maintenance of Filaments – (Invited Review)," Solar Physics, Vol. 182, No. 1, pp. 107-137, September 1998.

[45] Nelson D. A. Mascarenhas, Ilana A. Souza, Paulo E. Cruvinel, Clovis I. Biscegli, Reinaldo R. Rosa, "An estimation theoretic approach to 3D image interpolation," Proceedings of the XIII Brazilian Symposium on Computer Graphics and Image Processing, pp. 163-169, October 2000.

[46] Noriaki Miura, Naoshi Baba, Takashi Sakurai, Kiyoshi Ichimoto, Dirk Soltau, Peter Brandt, "Resolution Improvement of Solar Images," Solar Physics, Vol. 187, No. 2, pp. 347-356, July 1999.

[47] Rafael Molina, Jorge Nunez, Francisco Jose Cortijo and Javier Mateos, "Image Restoration in Astronomy: A Bayesian Perspective," IEEE Signal Processing Magazine, Vol. 18, No. 2, pp. 11-29, March 2001.

[48] James G. Nagy, Robert J. Plemmons, Todd C. Torgersen, "Iterative image restoration using approximate inverse preconditioning," IEEE Transactions on Image Processing, Vol. 5, No. 7, pp. 1151-1162, July 1996.

[49] The National Geophysical Data Center (NGDC). On-Line Glossary of Solar-Terrestrial Terms. Retrieved April 15, 2003 from the World Wide Web: http://www.ngdc.noaa.gov/stp/GLOSSARY/glossary.html.

[50] Heinz Neckel and Deitrich Labs, "Solar Limb Darkening 1986-1990 (λλ303 to 1099 nm)," Solar Physics, Vol. 153, No. 1, pp. 91-114, 1994.

[51] Xavier Orriols, Richardo Toledo, Xavier Binefa, Petia Radeva, Jordi Vitria and J.J. Villanueva, "Probabilistic Saliency Approach for Elongated Structure Detection Using Deformable Models," Proceedings of the 15th International Conference on Pattern Recognition (ICPR'00), Vol. 3, pp. 1006-1009, September 2000.

[52] José Paumard, Éric Aubourg, "Adjusting astronomical images using a censored Hausdorff distance," Proceedings of the International Conference on Image Processing, Vol. 3, pp. 232-235, October 1997.

[53] Soo-Chang Pei, Chin-Lun Lai and Frank Y. Shih, "Efficient class of alternating sequential filters in morphology," Graphical Models and Image Processing, Vol. 59, No. 2, pp. 109-116, 1997.

[54] Dora G. Preminger, Stephen R. Walton, and Gary A. Chapman, "Solar Feature Identification using Contrasts and Contiguity," Solar Physics, Vol. 202, No. 1, pp. 53-62, August 2001.

[55] Athanasios M. Psomoulis, Natalie Cazajus, Jannis S. Dandouras, Henry Barthe, Michel Gangloff, and Emmanuel T. Sarris, "Development of an innovative, two-processor data processing unit for the magnetospheric imaging instrument onboard the Cassini mission to Saturn. I. Hardware architecture," IEEE Transactions on Geoscience and Remote Sensing, Vol. 37, No. 4, pp. 1980-1996, July 1999.

[56] Jiong Qiu, Haimin Wang, Jongchul Chae, and Philip R. Goode, "Counter-streaming Mass Flow and Transient Brightening in Active Region Loops," Solar Physics, Vol. 190, pp. 153-165, December 1999.

[57] John C. Russ, *The Image Processing Handbook*, Third Edition, CRC PressLLC, 1999.

[58] Frank Y. Shih and C.C. Pu, "Analysis of the Properties of Soft Morphological Filtering Using Thresholding Decomposition," IEEE Transactions on Signal Processing, Vol. 43, No. 2, pp. 539-544, February 1995.

[59] Frank Y. Shih and P. Puttagunta, "Recursive Soft Morphological Filters," IEEE Transactions on Image Processing, Vol. 4, No. 7, pp. 1027-1032, July 1995.

[60] Frank Y. Shih, Chung Ta King and C.C. Pu, "Pipeline Architectures for Recursive Morphological Operations," IEEE Transactions on Image Processing, Vol. 4, No. 1, pp. 11-18, January 1995.

[61] Pierre Soille, Edmond J. Breen, and Ronald Jones, "Recursive Implementation of Erosions and Dilations Along Discrete Lines at Arbitrary Angles," IEEE Trans. Pattern Analysis and Machine Intelligence, vol. 18, no. 5, pp. 562-567, May 1996.

[62] Pierre Soille and Hughes Talbot, "Directional Morphological Filtering," IEEE Transactions on Pattern Analysis and Machine Intelligence, vol. 23, No. 11, pp. 1313-1329, November 2001.

[63] Jean-Luc Starck and Fionn Murtagh, "Astronomical Image and Signal Processing: Looking at Noise, Information, and Scale," IEEE Signal Processing Magazine, Vol. 18, No. 2, pp. 30-40, March 2001.

[64] Qing-Rui Su and Min Su "CME's, filament eruptions, and sheared low-lying magnetic loops in multipolar magnetic configuration," Solar Physics, Vol. 194, No. 1, pp. 121-130, May 2000.

[65] Glen Thorpe, Donald Fraser, "Correction and restoration of images obtained through turbulent media," Proceedings of 1996 IEEE TENCON. Digital Signal Processing Applications, Vol. 1, pp. 415-420, November 1996.

[66] Glen Thorpe, Andrew Lambert, and Donald Fraser, "Atmospheric turbulence visualisation through image time-sequence registration," Proceedings of the Fourteenth International Conference on Pattern Recognition, Vol. 2, pp. 1768-1770, August 1998.

[67] Richardo Toledo, Xavier Orriols, Xavier Binefa, Petia Radeva, Jordi Vitria and J.J. Villanueva, "Tracking Elongated Structures Using Statistical Snakes," Proceedings of the IEEE Conference on Computer Vision and Pattern Recognition, Vol. 1, pp. 157-162, June 2000.

[68] Richardo Toledo, Xavier Orriols, Petia Radeva, Xavier Binefa, Jordi Vitria, Cristina Canero and J.J. Villanueva, "Eigensnakes for Vessel Segmentation in Angiography," Proceedings of the 15th International Conference on Pattern Recognition (ICPR'00), Vol. 4, pp. 340-343, September 2000.

[69] Michael J. Turmon and Saleem Mukhtar, "Recognizing Chromospheric Objects via Markov Chain Monte Carlo," Proceedings of the International Conference on Image Processing, Vol. 3, pp. 320-323, 1997.

[70] P.S. Umesh Adiga and B.B. Chaudhuri, "Analysis of volumetric images of filamentous bacteria in industrial sludge," Proceedings of the Fourteenth International Conference on Pattern Recognition, Vol. 2 , pp. 1735-1737, 1998.

[71] C. M. de Vos, K. van der Schaaf, and J. D. Bregman, "Cluster computers and grid processing in the first radio-telescope of a new generation," Proceedings of the First IEEE/ACM International Symposium on Cluster Computing and the Grid, pp. 156-160, May 2001.

[72] Thomas Walter, Jean-Claude Klein, Pascalle Massin and Ferderic Zana, "Automatic Segmentation and Registration of Retinal Fluorescein Angiographies: Application to Diabetic Retinopathy," First International Workshop on Computer Assisted Fundus Image Analysis (CAFIA), May 2000, Copenhagen, Denmark.

[73] Haimin Wang, Carsten Denker and John Cerpinelli, "Development and Application of Real-Time Imaging at Big Bear Solar Observatory," BBSO, NJIT, August 2000.

[74] H. Wang, C. Denker, T. Spirock, P.R. Goode, S. Yang, W. Marquette, J. Varsik, R.J. Fear, J. Nenow, and D.D. Dingley, "New Digital Magnetograph At Big Bear Solar Observatory," Solar Physics, Vol. 183, No. 1, pp. 1-13, November 1998.

[75] David F. Webb, "Coronal Mass Ejections: Origins, Evolution, and Role in Space Weather," IEEE Transactions on Plasma Science, Vol. 28, No. 6, pp. 1795-1806, December 2000.

[76] D. C. Wells, E. W. Griesen and R. H. Harten, "FITS: A Flexible Image Transport System," Astron. Astrophys., Vol. 44, pp. 363-370, 1981.

[77] S. T. Wu, W. P. Guo, Murray Dryer, "Dynamical Evolution of a Coronal Streamer – Flux Rope System – II. A Self-Consistent Non-Planar Magnetohydrodynamic Simulation," Solar Physics, Vol. 170, No. 2, pp. 265-282, February 1997.

[78] Frédéric Zana and Jean-Claude Klein, "Robust segmentation of vessels from retinal angiography," Proceedings of the 13th International Conference on Digital Signal Processing, Vol. 2, pp. 1087-1090, July 1997.

[79] Frédéric Zana and Jean-Claude Klein, "A Multimodal Registration Algorithm of Eye Fundus Images Using Vessels Detection and Hough Transform," IEEE Transactions on Medical Imaging, Vol. 18, No. 5, pp. 419-428, May 1999.

[80] Frédéric Zana and Jean-Claude Klein, "Segmentation of Vessel-Like Patterns Using Mathematical Morphology and Curvature Evaluation," IEEE Transactions on Image Processing, Vol. 10, No. 7, pp. 110-119, July 2001.

[81] Lin Zhou, Chandra Kambhamettu, Dmitry B. Goldgof, K. Palaniappan, and A. F. Hasler, "Tracking Nonrigid Motion and Structure from 2D Satellite Cloud Images without Correspondences," IEEE Transactions on Pattern Analysis and Machine Intelligence, vol. 23, No. 11, pp. 1330-1336, November 2001.